

ROTATIONAL TUNNEL SPLITTING OF METHYL
QUANTUM ROTORS IN THE CONDENSED PHASE

DISSERTATION

ZUR ERLANGUNG DES DOKTORGRADES DER
NATURWISSENSCHAFTEN
(DR. RER. NAT.)

der

Naturwissenschaftliche Fakultät II
Chemie, Physik und Mathematik
der Martin-Luther-Universität Halle-Wittenberg

VORGELEGT VON

Frau Somayeh Khazaei

GEB. AM 01.03.1983 IN TEHERAN

DAY OF PUBLIC DEFENSE: JUNE 28, 2018

Prof. Dr. Daniel Sebastiani	First Reviewer
MLU Halle-Wittenberg	
Institut für Physikalische Chemie	
Von-Dankelmann Platz 4	
06120 Halle (Saale)	
Germany	

Prof. Dr. Jeremy O. Richardson	Second Reviewer
HCI D 267.3	
Vladimir-Prelog-Weg 1-5/10	
8093 Zürich	
Switzerland	

This dissertation has been created under the supervision of Prof. Daniel Sebastiani at the Institute of the Martin-Luther University Halle-Wittenberg.

This work has in parts been funded by deutsche akademischer austauschdienst (DAAD).

ABSTRACT

In this thesis, a method is presented for the numerical determination of tunnel splittings of the rotational quantum states of methyl groups at low temperatures and in the presence of realistic condensed-phase chemical environment. The rotational quantum states are obtained via direct diagonalization of the corresponding Hamiltonian in one and two dimensions (single methyl quantum rotor and two coupled methyl quantum rotors, respectively). The rotational potential and the methyl–methyl coupling strength are obtained quantitatively via quantum chemical calculations of the corresponding potential energy surface within the framework of density functional theory combined with the nudged elastic band method.

Experimentally, a large tunnel splitting can be exploited for enforcing the almost exclusive population of the lowest rotational quantum state of the methyl groups of a macroscopic sample at low temperatures. This well-defined population in turn can be transferred to the proton spin state, yielding a large spin hyperpolarization well beyond the Boltzmann level, which results in a signal amplification in NMR spectroscopy by several orders of magnitude.

The relationship between the dynamics of the methyl rotators and their environments at low temperature for two specific systems, γ -picoline and toluene are discussed and the results of the calculations are compared with the experiments. The focus is on the effect of chemical environment (supermolecular packing) on the tunnel splitting. In particular, the influence of coupled motion of methyl rotators on the tunneling spectrum is investigated within a pair-coupled model.

A surprising result is that the presence of a coupled second methyl group can actually *decrease* the rotational barrier of the two-dimensional quantum rotor, yielding an unexpectedly *large* tunnel splitting between the symmetric and antisymmetric combination of the two individual quantum rotor states. This effect is observed under the condition that the coupling strength approximately equals the individual rotor potential, which in turn enables a low-barrier coherent motion of the two methyls.

PUBLICATIONS

Some of the work described in this thesis has been published in peer-reviewed Journal. In the following, the individual contributions of authors are specified:

- S. Khazaei and D. Sebastiani. “Tunneling of coupled methyl quantum rotors in 4-methylpyridine: single rotor potential versus coupling interaction.” *J. Chem. Phys.* **147**, 194303 (2017).

For this publication, S. Khazaei carried out all the preparation, calculation, code development, analysis, and wrote the manuscript. D. Sebastiani supervised the project and discussed the results.

- S. Khazaei and D. Sebastiani. “Methyl rotor quantum states and the effect of chemical environment in organic crystals: γ -picoline and toluene.” *J. Chem. Phys.* **145**, 234506 (2016).

For this publication, S. Khazaei carried out all the preparation, calculation, code development, analysis, and wrote the manuscript. D. Sebastiani supervised the project and discussed the results.

ACKNOWLEDGEMENTS

I would like to thank my supervisor, Daniel Sebastiani, for his insight and guidance throughout the whole period which I have been on this project. I am particularly grateful to him for all his attempts to provide the conditions in which I could progress and complete this study.

I would like to thank our collaborators, Prof. Stefan Berger, Prof. Jörg Matysik, and Corrina Dietrich for fruitful discussions. I am also grateful to Prof. Jeremy O. Richardson for the helpful discussions.

I appreciate the good times I had with the group members. I am grateful to Jörg Reichenwallner and Jan Vorrath for their warm encouraging words.

I would like to express my sincere gratitude to the German Academic Exchange Service (DAAD) for awarding me the doctoral scholarship to study in Germany.

My extreme gratitude belongs to my parents, who paved the path for me to higher education, and my brother who has simply helped me in my research.

“I HAVE NOT FAILED.

I’VE JUST FOUND 10,000 WAYS THAT DON’T WORK.”

-THOMAS A. EDISON

CONTENTS

1	INTRODUCTION	1
2	THEORETICAL AND COMPUTATIONAL METHODS	5
2.1	Density Functional Theory combined with Nudged Elastic Band method	5
2.1.1	Born-Oppenheimer approximation	6
2.1.2	Many-body electronic wavefunction	8
2.1.3	Hohenberg-Kohn theorems	9
2.1.4	Kohn-Sham equations	10
2.1.5	Exchange-correlation functional	12
2.1.6	Dispersion effects	15
2.1.7	Basis set	16
2.1.8	Pseudopotential approximation	20
2.1.9	Nudged elastic band method for finding minimum energy path	22
2.1.10	Numerical wavefunction of 1-Dimensional CH ₃ rotors	26
2.2	Ab-initio Molecular Dynamics approach combined with semiclassical method	33
2.2.1	Wentzel-Kramers-Brillouin (WKB) approximation	34
2.2.2	The Semiclassical tunneling method of Makri and Miller	37
2.3	Ring-Polymer instanton method	38
2.3.1	Path-integral formulation of tunneling splittings	39
2.3.2	Steepest descent approximation	41
2.3.3	Expression for the tunneling splitting	45
3	METHYL GROUP ROTATION AND TUNNELING IN CONDENSED PHASE	46
3.1	Methyl group dynamics within a parameter model potential	46
3.1.1	Tunnel splitting	50
3.2	Rotational tunneling in γ -picoline and toluene	51
3.2.1	Packing effect	53
3.2.2	Coupling effect	60
4	ROTATIONAL TUNNELING OF COUPLED METHYL QUANTUM ROTORS	65
4.1	Tunneling spectrum of coupled methyl groups within a coupled-pair model	66

4.1.1	Free rotation of two rotors	67
4.1.2	Two uncoupled rotors in hindered potentials	67
4.1.3	Two coupled rotors	68
4.1.4	Quantitative picture of the influence of coupling on tunneling spectrum	72
4.2	Coupled methyl quantum rotation in γ -picoline	72
4.2.1	Determination of two-dimensional potential energy surface . .	73
4.2.2	Energy-levels and density distribution of methyl protons . . .	75
5	CONCLUSIONS AND FUTURE WORK	79
	BIBLIOGRAPHY	81
	LIST OF FIGURES	95
	LIST OF TABLES	96
	APPENDICES	96
A	METHYL ROTOR IN A ONE-DIMENSIONAL POTENTIAL OF GENERAL SHAPE	97
B	ANALYTICAL SOLUTION TO THE COUPLED-PAIR MODEL HAMILTONIAN	101
C	NUMERICAL TESTS OF THE TWO DIMENSIONAL CODE	104
D	NUMERICAL IMPLEMENTATION OF THE AIMD APPROACH COMBINED WITH THE SEMICLASSICAL METHOD	110
E	NUMERICAL IMPLEMENTATION OF THE RING-POLYMER METHOD	116

CHAPTER 1

INTRODUCTION

This work is focused on explicit calculations of tunneling splittings of methyl groups in the condensed phase. At low temperature, methyl groups represent quantum rotors with quantized rotational states. The lowest excitation energy between the ground and first excited state, known as the tunnel splitting, is important in the context of hyperpolarization techniques in nuclear magnetic resonance (NMR) spectroscopy. Berger *et al.*^{1,2} reported a simple experimental approach, yielding a ^{13}C signal enhancement for the methyl carbon of γ -picoline ($\text{C}_5\text{H}_4\text{NCH}_3$) of about $\times 100$. This signal enhancement was ascribed to the very low barrier for methyl group rotation in γ -picoline, which leads to a large quantum rotor splitting and associated phenomena such as the Haupt effect.³ Recently, Levitt *et al.*⁴⁻⁶ presented a theoretical framework describing the relationship between nuclear quantum rotor states/tunnel splitting energies and the induced NMR polarization effect, which was termed quantum-rotor-induced polarization.⁴⁻⁷ Here, the focus is on the theoretical investigation of tunneling splitting phenomena in nanoscale, in particular methyl groups in molecular crystals are the subject of this work; γ -picoline as a specific case owing to its large tunneling splittings.

A number of theoretical approaches have been proposed to calculate tunneling splittings. The most accurate method is the direct solution of Schrödinger equation by diagonalization of the Hamiltonian. Other formally exact quantum statistical methods are based on an imaginary time formulation of quantum mechanics such as diffusion Monte Carlo⁸ (DMC) and imaginary time path integrals.^{9,10} DMC is a suitable method for determining the ground state energy of quantum system, which takes the advantage of the similarity between the imaginary time Schrödinger equation and a generalized diffusion equation. This equation can be solved by simulating random walks of many replicas of the system. The latter exact approaches, based on an imaginary-time path integral, have been used for the calculation of electron transfer in a fixed environment.^{11,12} However, their theories are related to the calculation of tunneling splittings between two degenerate wells and there is no straightforward generalization of them for treating systems with more than two wells. The common disadvantage of both above statistical approaches is that sampling over a great

number of independent configurations is required to reduce the statistical errors. In general, the application of all these exact methods are limited to small systems. To treat complex systems in full dimensionality is therefore required approximate methods which are mostly given based on reduced dimensionality and WKB approximation; after G. Wentzel, H. A. Kramers and L. Brillouin,¹³⁻¹⁵ in which the wavefunction is approximated as $e^{iS(x)/\hbar}$, where $S(x) = \int dx \sqrt{2m[E - V(x)]}$ is the classical action, which becomes imaginary in classically-forbidden region. The full system is then described by a nearly one-dimensional chosen reaction coordinate, x , and the tunneling splittings is estimated under WKB approximation along the tunneling path.^{16,17}

One of such approximate methods is based on the ab-initio molecular dynamics combined with semiclassical method of Makri-Miller.¹⁸ The semiclassical model of Makri-Miller¹⁹ for tunneling is based on the WKB approximation. A brief summary of this method is given in Chapter 2.2. The method is applied to the case of the umbrella inversion of Ammonia, given in Appendix D. The principle feature of the model is that it can be implemented within ab-initio trajectory simulation, in order to incorporate the multidimensional effects associated with the tunneling. The major drawback, however, is that it requires the prior knowledge of tunneling path and classical turning points. Furthermore, there is no straightforward recipe to generalize the tunneling model to multidimensional potential wells. All these drawbacks limit the application of method to polyatomic molecules and make it inappropriate to study the rotational tunneling of methyl groups.

The other approximate approach studied within this thesis is the ring-polymer instanton^{17,20} based on an imaginary-time path-integral representation of the Boltzmann operator. In the semiclassical approximation to the path integral, the principal exponential factor is given by the action along the periodic orbit, refer as to “instanton”, on the upside down potential surface.²¹ Similar to the WKB method, the instanton pathway is the one which minimizes the action integral but in multidimensional systems. The advantage of the instanton method over the WKB is that it requires no sampling and prior knowledge of the tunneling path and turning points. A review of the approach is given in Chapter 2.3. The disadvantage of the approach is that the fluctuations around the instanton are treated harmonically and the anharmonicity perpendicular to instanton is neglected, which may result in large errors in systems with low barriers. The method is investigated for the tunneling in one-dimensional three-fold cosine potential, given in Appendix E. As it

was expected, the error associated to the low barrier heights is large. In principle, this approach is promising to estimate the rotational tunneling splittings of methyl groups in molecular crystals. However, as the results of the one-dimensional test calculations show, it is not suitable to apply to γ -picoline, which is known to possess a low methyl rotational barrier. The other difficulty is due to the estimation of Hessian matrix, second derivative of ab-initio potential with respect to the atomic coordinates, which is computationally expensive especially for a system containing a large number of atoms. In the following, the approximate method presented within this work for the evaluation of tunneling splittings is discussed.

Over the years, many theoretical studies have been performed to extract the amplitude and shape of the rotational potential energy surface (PES) of methyl groups along the tunneling path using empirical or semi-empirical molecular mechanic calculations.²²⁻²⁵ In these studies, the dynamics of methyl group is approximated by the one-dimensional rotor as a function of its rotational angle rotating around the C-C bond axis. The rotational potential function is then approximated as the sum of intramolecular and intermolecular terms, which are fitted empirically with the limited data obtained mainly by inelastic neutron scattering (INS) experiments. In semi-empirical PESs, some terms of the potentials are obtained by the quantum chemistry methods for only one single molecule or a small cluster of molecules which are afterwards adjusted for the whole system. The correct description of methyl groups, however, requires an electronic structure calculation since the electron density plays an important role in the intermolecular interactions. Therefore, such PESs are not accurate enough especially for the application of calculating the tunnel splittings, which are highly sensitive to the PES. In this work, the accurate geometrical structures are obtained from the ab initio calculations and the methyl rotational potential energy surfaces along the tunneling path are determined with a more sophisticated method without any parameterization.

In this regard, a method of calculation for the tunneling splittings of methyl rotators is introduced based on the ab initio density functional theory and reduced dimensionality of Schrödinger equation. The method is inspired by the former studies in the field of methyl rotational tunneling.²⁴ The optimal tunneling path is computed with nudged elastic band method,²⁶⁻²⁸ in which a band of replicas of the system is minimized along the rotational tunneling path. The numerical solution of one-dimensional Schrödinger equation on the basis of the PES obtained via NEB scheme gives the rotational energy levels, and consequently tunnel splittings. The

theoretical background of the method is given in Chapter 2.1.

In Chapter 3, the most important characteristics of methyl tunneling within a one-dimensional three-fold cosine potential is presented. The eigenvalue dependence on the rotational barrier height is discussed in different regime of low, intermediate, and high rotational barrier heights. The method is explained and applied to the two real systems, γ -picoline and toluene. The large difference in magnitude of the tunneling splittings in these systems is explained in terms of the crystal packing and coupling effects. It turns out that coupling motion of methyl groups in γ -picoline has a significant effect on the reduction of rotational barrier. This point will be elaborated in the next chapter. This chapter is based on published material, Khazaei et al., 2016.

In some systems, such as γ -picoline²⁹ and lithium acetate dihydrate,^{22,23} an analysis of the low temperature complex INS spectrum goes beyond the single methyl rotation description. Generally, the experimentally observed multiple tunneling peaks arising from a single type of methyl group are assigned to the orientational interaction between near-lying neighboring pairs of methyl groups, i.e, rotor-rotor coupling. Chapter 4 presents a computational study of the effects of the rotational coupling between a pair of one-dimensional methyl rotors on the low-energy level structure of the system. The rotational potential of coupled pair of methyl rotors is approximated by three-fold periodic potential terms, describing intramolecular, and intermolecular interactions. A two-dimensional bound-state Schrödinger equation is solved by the product basis of two free-rotor functions. The objective is to investigate how the interplay between the strength of the single-rotor potential and the rotor-rotor coupling strength manifests in the pattern of the low-lying two-dimensional coupled-rotor levels. Three different cases are considered, with weak, intermediate, and strong coupling between the rotors. An important observation is that for the intermediate coupling, the degeneracy of the EE levels is partially lifted. In addition to these model calculations, the coupled rotations of methyl groups in γ -picoline in crystalline phase are investigated, which consists of methyl groups with spatially opposed to each other. The two-dimensional PES is calculated from condensed-phase DFT energy profiles. The two-dimensional Schrödinger equation is solved for this two-dimensional coupled-rotor PES. The results also show splitting of the EE states into a pair of doubly degenerate levels, due to the coupling. This chapter is based on published material, Khazaei et al., 2017.

CHAPTER 2

THEORETICAL AND COMPUTATIONAL METHODS

This chapter is intended to review important concepts for three theoretical approaches of calculating tunneling splittings.

2.1 DENSITY FUNCTIONAL THEORY COMBINED WITH NUDGED ELASTIC BAND METHOD

An accurate prediction of materials properties requires an excellent representation of the interactions between ions and electrons. This in principle could be done exactly by solving the many body Schrödinger equation of quantum theory, but is impossible to directly solve it for anything beyond simple systems without applying some approximations. A range of choices for these necessary simplifications have made it possible to investigate the electronic structure of many body systems, in particular in the condensed phases. Among different methods, the density functional theory³⁰⁻³³ (DFT) has vastly been proven to be a reliable approximation to treat the interactions of electrons and nuclei and consequently to study properties of materials. In this regard, DFT provides a computational quantum mechanical approach to treat many body systems non-empirically.

In this work, the structural optimizations and electronic structure calculations for methyl groups in crystal structure are performed using the DFT. In the following sections, the general idea and relevant aspects of DFT to this work are presented. The nudged elastic band (NEB) method²⁶⁻²⁸ is then introduced for finding the minimum energy path between two potential minima. The NEB method in combination with electronic structure density functional calculations are used to evaluate the rotational potential energy surface (PES) of the methyl groups along the tunneling path. The tunneling splitting is given by the numerical solution of the corresponding time independent Schrödinger equation for one-dimensional methyl rotors with the calculated PESs. In this regards, the Numerov method for numerically integrating the one-dimensional Schrödinger equation³⁴ is described and followed by the numerical solution of the two-dimensional Schrödinger equation³⁵ for a pair of methyl rotors.

2.1.1 BORN-OPPENHEIMER APPROXIMATION

The time independent non-relativistic Schrödinger equation for a system of interacting electrons and nuclei is given by

$$\mathcal{H} \Psi(\{\mathbf{r}_i\}, \{\mathbf{R}_\alpha\}) = E \Psi(\{\mathbf{r}_i\}, \{\mathbf{R}_\alpha\}) \quad (2.1)$$

where E is the total energy of the system and $\Psi(\{\mathbf{r}_i\}, \{\mathbf{R}_\alpha\})$ is the full electron-nuclear wave function. The many body Hamiltonian operator \mathcal{H} , is given by

$$\begin{aligned} \mathcal{H} = & \sum_{\alpha} -\frac{1}{2M_{\alpha}} \nabla_{\mathbf{R}_{\alpha}}^2 + \sum_i -\frac{1}{2} \nabla_{\mathbf{r}_i}^2 + \frac{1}{2} \sum_{i \neq j} \frac{1}{|\mathbf{r}_i - \mathbf{r}_j|} + \\ & - \sum_i \sum_{\alpha} \frac{Z_{\alpha}}{|\mathbf{r}_i - \mathbf{R}_{\alpha}|} + \frac{1}{2} \sum_{\alpha \neq \beta} \frac{Z_{\alpha} Z_{\beta}}{|\mathbf{R}_{\alpha} - \mathbf{R}_{\beta}|} \end{aligned} \quad (2.2)$$

The first two terms represent the nuclear and electronic kinetic energy operators, respectively, while the subsequent three terms describe electrons-electrons, electrons-nuclei, and nuclei-nuclei Coulomb interaction. Note that in this Hamiltonian, \mathbf{R}_{α} and \mathbf{r}_i denote the position of nuclei α and electronic particles i , respectively. M_{α} , and Z_{α} are the masses and charges of the nuclei in atomic units. Electronic charge and mass as well as \hbar in atomic units are equal to one.

The Born-Oppenheimer (BO) approximation³⁶ is based on the fact that the masses of the atomic nuclei are much larger than the ones of the electrons. This implies a large difference in time scales of their dynamics; the electrons respond instantaneously to the motion of the nuclei. The decoupling in dynamical evolution of electrons and nuclei results in a separation of the spectra in such a way that the electrons are always in their instantaneous ground-state for a given nuclear configuration. To a high degree the positions of the nuclei can be regarded as fixed. Vibrations of the nuclei around their equilibrium positions can be treated adiabatically, leading to a separation of electronic and nuclear parts in full electron-nuclear wave function. Then the total wavefunction can be written as the product of the nuclear and electronics parts

$$\Psi(\{\mathbf{r}_i\}, \{\mathbf{R}_{\alpha}\}) = \psi_{\mathbf{R}_{\alpha}}(\{\mathbf{r}_i\}) \Phi(\{\mathbf{R}_{\alpha}\}) \quad (2.3)$$

where $\Phi(\{\mathbf{R}_{\alpha}\})$ is a function of nuclear coordinates only and $\psi_{\mathbf{R}_{\alpha}}(\{\mathbf{r}_i\})$ is a function of electron coordinates which parametrically depends on a specific nuclear geometry $\{\mathbf{R}_{\alpha}\}$. Accordingly, at any given instant, the electrons feel a Hamiltonian that depends on the position of the nuclei at that instant. The essential element of this

approximation is that applying the nuclear kinetic energy operator to the electronic wavefunction yields zero, *i.e.*, the derivative of the electronic wavefunction with respect to the nuclear coordinates is approximated as zero, then

$$\sum_{\alpha} \frac{1}{2M_{\alpha}} \nabla_{\mathbf{R}_{\alpha}}^2 \left[\psi_{\mathbf{R}_{\alpha}}(\{\mathbf{r}_i\}) \Phi(\{\mathbf{R}_{\alpha}\}) \right] \approx \psi_{\mathbf{R}_{\alpha}}(\{\mathbf{r}_i\}) \sum_{\alpha} \frac{1}{2M_{\alpha}} \nabla_{\mathbf{R}_{\alpha}}^2 \left[\Phi(\{\mathbf{R}_{\alpha}\}) \right] \quad (2.4)$$

Accordingly, within this approximation, the Schrödinger equation can be decoupled into two equations for electrons in a constant field of nuclei and an equation for nuclei movement. The Hamiltonian for the electronic system becomes

$$\mathcal{H}^{el} = \sum_i -\frac{1}{2} \nabla_{\mathbf{r}_i}^2 + \frac{1}{2} \sum_{i \neq j} \frac{1}{|\mathbf{r}_i - \mathbf{r}_j|} - \sum_i \sum_{\alpha} \frac{Z_{\alpha}}{|\mathbf{r}_i - \mathbf{R}_{\alpha}|} \quad (2.5)$$

The ground-state energy of a system of interacting electrons in the constant field of fixed nuclei is obtained by solving the electronic Schrödinger equation

$$\mathcal{H}^{el} \psi_{\mathbf{R}_{\alpha}}(\{\mathbf{r}_i\}) = E^{el}(\mathbf{R}_{\alpha}) \psi_{\mathbf{R}_{\alpha}}(\{\mathbf{r}_i\}) \quad (2.6)$$

where the eigenvalues, $E^{el}(\mathbf{R}_{\alpha})$, have a parametric dependence on the particular nuclear configurations. Once the Eq. (2.6) is solved, one can write down the Schrödinger equation for the nuclei motion

$$\left[\sum_{\alpha} -\frac{1}{2M_{\alpha}} \nabla_{\mathbf{R}_{\alpha}}^2 + \underbrace{E^{el}(\mathbf{R}_{\alpha}) + \frac{1}{2} \sum_{\alpha \neq \beta} \frac{Z_{\alpha} Z_{\beta}}{|\mathbf{R}_{\alpha} - \mathbf{R}_{\beta}|}}_{E_{BO}(\{\mathbf{R}_{\alpha}\})} \right] \Phi(\{\mathbf{R}_{\alpha}\}) = E \Phi(\{\mathbf{R}_{\alpha}\}) \quad (2.7)$$

Therefore, the nuclei move on an effective potential energy surface defined by the electronic energy. The Born-Oppenheimer energy surface, $E_{BO}(\{\mathbf{R}_{\alpha}\})$, is defined as the potential energy of the system, which is a function of nuclear coordinates.

In most cases, the Born-Oppenheimer approximation turns out to be reasonably accurate, when electronic potential surfaces are well isolated from other surfaces; and the nuclei displacements are very small from an equilibrium configuration. However as with any approximation, it has certain limitations. This approximation becomes problematic when treating excited states and fails to address the effects of degeneracy, *i.e.*, the coupling between different eigenstates of the electronic Hamiltonian, known as non-adiabatic coupling. In non-adiabatic cases, two or more potential surfaces come close energetically or actually intersect one another.³⁷ Although using the framework suggested by the Born-Oppenheimer approximation leads to the electronic wavefunction which has only a parametric dependence on the nuclear positions, however the complexity of solving the electronic Schrödinger equation due to the electrons-electrons interaction remains. Thereby, additional simplifications are needed to solve the many body problem.

2.1.2 MANY-BODY ELECTRONIC WAVEFUNCTION

For the simplification of the electronic Schrödinger equation, two branches of approaches have arisen: wavefunction-based approaches and density functional theory.

The wavefunction-based approaches expand the many electron wavefunction as a sum of Slater determinants of atomic basis functions. The simplest method of this type is Hartree-Fock (HF),³⁸ where the many electron wavefunction is approximated by a single antisymmetrized product wavefunction, *i.e.*, a single Slater determinant made up of one spin orbital per electron. Employing the variational principle to minimize the total electronic energy with respect to single electron wavefunction, under the orthonormality constraint, yields a set of Hartree-Fock equations. The solutions to the non-linear Hartree-Fock equations behave as if each electron moves independently of all the others while it is subjected to: (1) the mean field created by the Coulomb repulsion due to the average positions of all electrons; and (2) the exchange interaction due to antisymmetrization. Essentially, Hartree-Fock equation is an eigenvalue problem of an effective single electron Hamiltonian. Although it is found that the Hartree-Fock method produces reasonable results for many molecular properties, nevertheless, it has certain limitations because of complete neglect of correlation between antiparallel spins. For example, a restricted closed shell (doubly occupied molecular orbitals) HF solution fails to provide a robust description of reactive chemical events and calculation of dissociation energies in which electron correlation has a significant role.³⁹

The post Hartree-Fock methods are then developed to improve the accuracy of HF method by going beyond the ansatz of a single-determinant wavefunction and considering not only occupied states but also unoccupied atomic orbitals. There exist two broad categories of such approaches: those based on the variational principle; as configuration-interaction⁴⁰/coupled cluster,⁴¹⁻⁴³ and those based on perturbation theory. Among the latter approaches, the second-order Moller-Plesset perturbation theory (MP2)⁴⁴ is the simplest and cheapest method for incorporating electron correlation effects. The common disadvantage of these wavefunction-based correlation methods is the high scaling of the computational cost. For instance, the scaling of the computational complexity for MP2 is $\mathcal{O}(N^5)$, where N is the number of atoms in molecule; the computational cost scale for the coupled cluster singles and doubles (CCSD) model is $\mathcal{O}(N^6)$ and $\mathcal{O}(N^7)$ for CCSD with perturbative triples corrections. By that means, the application range of these methods is restricted to small

molecules of rather modest size.⁴⁵

The second class of theoretical approaches of obtaining an approximate solution to the electronic Schrödinger equation is based on density functional theory (DFT). Unlike the previous approach, which deals directly with the many-body electronic wavefunction, the electron density is used as the fundamental property in DFT, which depends only on three spatial variables (as opposed to the dependence of electronic wave function to $3N$ coordinates of N electrons). For this reason, from computational complexity point of view, the density functional-based methods are highly attractive for treating large molecular systems. In this method, the difficult many-body interaction problem is mapped into a system of equations of non-interacting electrons. The method is described in details, in the following sections.

2.1.3 HOHENBERG-KOHN THEOREMS

Density functional theory is based on two theorems of Hohenberg-Kohn (1964).³⁰ The first Hohenberg-Kohn theorem states:

For systems with a nondegenerate ground-state; the external potential is uniquely determined by the corresponding ground-state electronic density, to within an additive constant.

The external potential is referred to the last term in Eq. (2.5); the interaction between electrons in external potential of the fixed nuclei,

$$V_{ext} = \sum_i v_{ext}(\mathbf{r}_i) = - \sum_i \sum_{\alpha} \frac{Z_{\alpha}}{|\mathbf{r}_i - \mathbf{R}_{\alpha}|} \quad (2.8)$$

The ground-state wavefunction ψ_0 for the electronic Hamiltonian, Eq. (2.5), is completely determined by the number of electrons N and the external potential. The electronic density $n_0(\mathbf{r})$ and N are related through normalization condition,

$$n_0(\mathbf{r}) = \int d\mathbf{r} |\psi_0(\mathbf{r})|^2 \quad (2.9)$$

$$N = \int d\mathbf{r} n_0(\mathbf{r}) \quad (2.10)$$

This theorem as stated above is saying that the ground-state density uniquely determines the external potential, from which it immediately follows that electron density also determines the ground-state wave function and all other electronic properties of the system.

For the proof, assume two distinct external potentials $v_1(\mathbf{r})$ and $v_2(\mathbf{r})$ that differ by more than a constant, with ground-state many body wavefunctions ψ_1 and ψ_2 , both leading to the same ground-state density. The ground-state energies are

$$\begin{aligned} E_1 &= \langle \psi_1 | \mathcal{H}_1 | \psi_1 \rangle \\ E_2 &= \langle \psi_2 | \mathcal{H}_2 | \psi_2 \rangle \end{aligned} \tag{2.11}$$

Then, the following inequalities hold

$$\begin{aligned} E_1 &< \langle \psi_2 | \mathcal{H}_1 | \psi_2 \rangle = \langle \psi_2 | \mathcal{H}_2 | \psi_2 \rangle + \langle \psi_2 | \mathcal{H}_1 - \mathcal{H}_2 | \psi_2 \rangle \\ &= E_2 + \int d\mathbf{r} n_0(\mathbf{r}) [v_1(\mathbf{r}) - v_2(\mathbf{r})] \end{aligned} \tag{2.12}$$

$$\begin{aligned} E_2 &< \langle \psi_1 | \mathcal{H}_2 | \psi_1 \rangle = \langle \psi_1 | \mathcal{H}_1 | \psi_1 \rangle + \langle \psi_1 | \mathcal{H}_2 - \mathcal{H}_1 | \psi_1 \rangle \\ &= E_1 + \int d\mathbf{r} n_0(\mathbf{r}) [v_2(\mathbf{r}) - v_1(\mathbf{r})] \end{aligned} \tag{2.13}$$

Adding Eq. (2.12) to Eq. (2.13) together results in the contradiction

$$E_1 + E_2 < E_1 + E_2 \tag{2.14}$$

Therefore, the first Hohenberg-Kohn theorem proved by reductio ad absurdum.

The second Hohenberg-Kohn theorem states:

For all ν -representable densities, the one that minimizes the energy functional, $E[n(\mathbf{r})]$, with a given external potential is the ground state density, $n_0(\mathbf{r})$.

The proof relies on a minimum variational principle for the density and following the direct consequence of the first theorem; so that the ground state energy satisfies the following inequality

$$E_0 = \langle \psi_0 | \mathcal{H} | \psi_0 \rangle \leq E[n(\mathbf{r})] \tag{2.15}$$

The Hohenberg-Kohn theorems show that the ground-state energy is then a functional of the ground-state density, from which all properties of the system can be calculated. But these theorems provide no prescription of how to construct the functional dependence of energy on the density. One year later, a practical scheme for approximating the functional energy becomes possible by the work of Kohn and Sham in 1965.³¹

2.1.4 KOHN-SHAM EQUATIONS

The Kohn-Sham approach is to replace the difficult interacting many-body system with a non-interacting auxiliary system, which has the same ground-state density

as the real, interacting system. Let the one electron orbitals $\Phi_i(\mathbf{r})$ being the eigenfunctions of the set of one-electron Schrödinger-like equations,

$$\mathcal{H}_{KS} \Phi_i(\mathbf{r}) = \epsilon_i \Phi_i(\mathbf{r}) \quad (2.16)$$

where the one electron orbitals are called the Kohn-Sham orbitals and the non-interacting electrons are moving in an effective potential. The kinetic energy and density are,

$$T_{KS}[\Phi_{[n]}] = -\frac{1}{2} \sum_i \langle \Phi_i | \nabla^2 | \Phi_i \rangle \quad (2.17)$$

$$n_{KS}(\mathbf{r}) = \sum_i |\Phi_i(\mathbf{r})|^2 \quad (2.18)$$

where $n_{KS}(\mathbf{r})$ by the Kohn-Sham assumption is equal to the ground-state density, $n(\mathbf{r})$, of the real system. The Kohn-Sham energy functional of the non-interacting system is

$$\mathcal{E}_{KS}[n] = T_{KS}[\Phi_{[n]}] + \mathcal{E}_H[n] + \mathcal{E}_{ext}[n] \quad (2.19)$$

where the electrostatic interactions between clouds of charge distribution is given by the Hartree energy of the system,

$$\mathcal{E}_H[n] = \frac{1}{2} \int d\mathbf{r} d\mathbf{r}' \frac{n(\mathbf{r})n(\mathbf{r}')}{|\mathbf{r} - \mathbf{r}'|} \quad (2.20)$$

and the interaction between electrons and the external potential provided by a given configuration of nuclei is

$$\mathcal{E}_{ext}[n] = \int d\mathbf{r} v_{ext}(\mathbf{r})n(\mathbf{r}) \quad (2.21)$$

The difference between the correct energy functional of the many-body interacting system of Eq. (2.6) and the energy functional of the non-interacting Kohn-Sham system, $\mathcal{E}_{KS}[n]$ in Eq. (2.19) is called as exchange-correlation functional $\mathcal{E}_{xc}[n]$ of the system. The exchange-correlation functional includes; (1) the difference between the exact electrons-electrons interaction energy and the one for the classical charge distribution of non-interacting system and (2) the energy difference between the exact kinetic energy of real system and the one for non-interacting system. The exact form of this $\mathcal{E}_{xc}[n]$ energy functional is unknown, and it is therefore in practice approximated, that will be discussed in next section.

According to the Hohenberg-Kohn theorem, the electron density that minimizes the total functional energy is the ground-state density. Applying the variational principle to total energy functional $\mathcal{E}_{KS} + \mathcal{E}_{xc}$ under the constraint that the total

number of electrons has to be conserved and equal to N , and μ as the Lagrange multiplier yields

$$\frac{\delta}{\delta n(\mathbf{r})} \left[\mathcal{E}_{KS}[n(\mathbf{r})] + \mathcal{E}_{xc}[n(\mathbf{r})] - \mu \int d\mathbf{r} n(\mathbf{r}) \right] = 0 \quad (2.22)$$

which is the Euler-Lagrange equation,

$$\frac{\delta}{\delta n(\mathbf{r})} \left[\mathcal{E}_{KS}[n(\mathbf{r})] + \mathcal{E}_{xc}[n(\mathbf{r})] \right] = \mu \quad (2.23)$$

To take the derivatives of the energy functionals with respect to the electron density gives,

$$\frac{\delta T_{KS}[\Phi_{[n]}]}{\delta n(\mathbf{r})} + v_{KS}(\mathbf{r}) = \mu \quad (2.24)$$

in which the effective Kohn-Sham potential is

$$v_{KS}(\mathbf{r}) = v_{ext}(\mathbf{r}) + v_H(\mathbf{r}) + v_{xc}(\mathbf{r}) \quad (2.25)$$

where the exchange-correlation potential is defined as

$$v_{xc}(\mathbf{r}) \equiv \frac{\delta \mathcal{E}_{xc}[n(\mathbf{r})]}{\delta n(\mathbf{r})} \quad (2.26)$$

Thereby the so-called Kohn-Sham equations, which read

$$\left[-\frac{1}{2} \nabla^2 + v_{KS}(\mathbf{r}) \right] \Phi_i(\mathbf{r}) = \epsilon_i \Phi_i(\mathbf{r}) \quad (2.27)$$

are then solved by the usual self consistent method, starting with a guess for the density. Accordingly, one obtains an initial set of Kohn-Sham orbitals, which is then used to compute an improved density from Eq. (2.18). This iteration is repeated until the density is converged to within some threshold. On each iterative procedure, the Kohn-Sham orbitals can be computed either numerically or expressed in terms of a set of basis set functions. In the latter case, the coefficients in the basis set expansion are found by the solution of KS equations.

At first glance, the Kohn-Sham equations are very similar to the Hartree-Fock self consistent one electron equations. In both non-interacting electrons are regarded as moving in an effective potential. However, the difference between two approaches is due to the exchange correlation potential term, which contains all the many body effects.

2.1.5 EXCHANGE-CORRELATION FUNCTIONAL

The success behind the density functional theory lies in the fact that the many body effects can be included via the exchange correlation functional. Nevertheless, the

challenge for DFT arises to find such a universal functional to fulfill its promise for description of the quantum nature of the matters. To date, a large number of such approximations have been developed that can be classified into six major groups; local density approximation⁴⁶ (LDA), generalized gradient approximation^{47,48} (GGA), meta-GGA,^{49,50} hybrid density functionals,^{51,52} double-hybrid density functionals,⁵³ and range separated density functionals.⁵⁴⁻⁵⁶ These approximations have different strengths and weaknesses, depending on the molecular systems, and the electronic properties that are studied.^{57,58} Here, the first two approximations are discussed in more details.

Local Density Approximation

The simplest method of describing the exchange-correlation energy of an electronic system is the local-density approximation. In the LDA, the exchange-correlation energy for the inhomogeneous system at the point \mathbf{r} in space with local density $n(\mathbf{r})$ is taken to be the same as the one for the uniform electron gas with the same density $n(\mathbf{r})$,

$$\mathcal{E}_{xc}^{LDA}[n] = \int d\mathbf{r} n(\mathbf{r}) \epsilon_{xc}[n(\mathbf{r})] \quad (2.28)$$

where $\epsilon_{xc}[n(\mathbf{r})]$ is the exchange correlation energy per electron in a uniform electron gas that depends locally on the density $n(\mathbf{r})$ at the position \mathbf{r} . This approximation is expected to be valid when the electronic density of the system varies slowly with the position in space. The LDA functional energy was then calculated, by dividing the exchange correlation energy per electron into two parts of exchange $\epsilon_x[n(\mathbf{r})]$, and correlation $\epsilon_c[n(\mathbf{r})]$ energy. The form of the exchange energy for the uniform electron gas was known due to the work of Dirac.⁵⁹ The functional for correlation was determined through Monte Carlo simulation of a uniform interacting electron gas at several limit of high and low densities,⁶⁰ which has been parameterized resulting to a function.^{47,61}

Surprisingly, such simple functional based on uniform electron gas yields results that reproduce well the experimental ground state properties of many solids. There is no concrete reason why LDA works well; it can be somehow due to the error cancelation between the exchange and correlation parts. The advantage of the DFT with LDA is the high convergence speed in the simulation of a huge number of atoms. This explains why DFT was first so popular in solid-state physics community. It has been shown that the LDA performs quite successfully for determination

of some molecular properties, particularly equilibrium structures, harmonic frequencies, and charge moments.⁶² However, it has serious problems in atomic and molecular physics; in molecules where the electron density can vary rapidly over small region of space; because the LDA ignores corrections to the exchange-correlation energy due to inhomogeneities in the electron density. It specifically fails to give a correct description of hydrogen bonds. One way to correct such problems is to build the exchange correlation functional as a function of both local density and the local gradient of the density.

Gradient corrections

The behavior of inhomogeneities in the electronic density and deviation from uniform electron gas can be expressed in terms of the gradient and higher order spatial derivatives of the total electron density. This improvement leads to the gradient corrected functionals, in which the gradient of the density as well as the local density is included in the exchange correlation energy,

$$\mathcal{E}_{xc}[n, \nabla n] = \int d\mathbf{r} n(\mathbf{r}) \epsilon_{xc}[n(\mathbf{r}), \nabla n(\mathbf{r})] \quad (2.29)$$

The gradient expansion (GE) is the most systematic nonlocal extension of LDA that developed first, in which the lowest Taylor expansion of the uniform density depends on $[\nabla n(\mathbf{r})]^2/[n(\mathbf{r})]^{\frac{4}{3}}$. However, it did not yield the desired accuracy as expected; it fails to treat the asymptotic region of system where the density exponentially decays. The remarkable improvement over GE functionals was made by the introduction of generalized gradient approximation (GGA), which has eventually received general acceptance of chemists. GGA functionals can be generically written as

$$\mathcal{E}_{xc}^{GGA}[n, \nabla n] = \int d\mathbf{r} f[n(\mathbf{r}), \nabla n(\mathbf{r})] \quad (2.30)$$

The freedom for defining the explicit dependence of the integrand f on the density and its gradient has lead to different version of generalized gradient approximation. The general form of these functionals can be determined either by fitting to a few empirical parameters of molecular properties, or using general rules of quantum mechanics, and limiting conditions.⁶³ Two most commonly used functionals of this type are Perdew-Burke-Ernzerhof (PBE),⁶¹ and BLYP exchange correlation functionals; which combines Becke’s 1988 exchange functional⁴⁸ with the correlation functional by Lee-Yang-Parr.⁵¹ Generally, GGA functionals lead to a number of improvements over LDA; most importantly they provide a good description of chemical bonds, particularly the hydrogen bonds, and bond dissociation energy. However, both GGA,

and LDA functionals present difficulties to describe weakly interacting molecules, which is beyond the description of a molecule at its equilibrium geometry. This error arises by formulation of these functionals; equations (2.28), and (2.29) are based on the local density and on its local derivatives. They imply that an electron at point \mathbf{r} in fragment “a” has no information about the electron at point \mathbf{r}' in remote fragment “b” (assume there is no overlap of between two fragments). This error has to be corrected to obtain a proper description of covalent bonding in chemistry, and transition states.

2.1.6 DISPERSION EFFECTS

The origin of the van der Waals (vdW) dispersion forces is the interaction of fluctuating charge distribution in one quantum system with those in an adjacent system. The charge fluctuations in each system with electrons yield an instantaneous polarization, and this sets up an induced dipole in the adjacent quantum system. The coupling of the fluctuations can be seen from perturbation theory arguments.^{64–66} The attractive part of the non-relativistic vdW interaction between two molecules (closed-shell species: all electrons are paired) has the asymptotic form,

$$E \sim -\frac{C_6}{\mathbf{r}^6} \quad (2.31)$$

where \mathbf{r} is the inter-molecular distance, and C_6 is the dispersion coefficient. A sum of interatomic pairwise potentials of the form Eq. (2.31) is then result to the vdW interaction. This form of potential is divergent in the limit of $\mathbf{r} \rightarrow 0$, where the dispersion energy remains finite. This problem is resolved when it is multiplied by a damping function.

There exist several different approaches based on a pragmatic consideration that the total DFT energy can be improved by adding to it an inter-atomic potential energy,

$$E_{DFT-D} = E_{DFT} + E_{disp} \quad (2.32)$$

The most prominent approaches introduced by Grimme,^{53,67,68} Tkatchenko and Scheffler (TS)⁶⁹ as well as Becke and Johnson (BJ).^{70,71} In the method developed by Grimme, known as DFT+D2, the dispersion energy is read,

$$E_{disp} = -s_6 \sum_{i<j} \frac{C_6^{ij}}{\mathbf{r}_{ij}^6} \frac{1}{1 + e^{-d(r_{ij}/s_R R_{ij}-1)}} \quad (2.33)$$

where s_6 is the global scaling parameter which has been optimized for each version of GGA functionals; r_{ij} is the distance between the pair of i -th and j -th atoms. The dispersion coefficient is computed using $C_6^{ij} = \sqrt{C_6^i C_6^j}$, where the value of C_6^i is tabulated for each element in the periodic table. The van der Waals radii R_{ij} is computed via $R_{ij} = R_i + R_j$, where R_i is the tabulated van der Waals radii that combined with the constants s_R and d define the behaviour of the damping function. The DFT-D2 is computationally quite efficient with rather low computation cost. However, it does not take into account the dependency of dispersion interactions on the chemical state and environment. It lacks the dependence on the electron distribution of atom, which may be influenced by its neighbors, and thereby the polarizabilities of molecules are ignored. This issue is addressed in DFT-D3, a later development of the Grimme method, in which the different chemical environment of atoms are taken into account by employing the coordination numbers; so that the dispersion coefficients, C_6^{ij} , are adjusted to the basis of local geometry. The DFT-D3 also includes triplets of atoms to account for three-body effects. As the dispersion correction is an additive term to the DFT energy, it does not directly change the wavefunction, electron density or any other molecular property. However, the dispersion correction contributes to the forces acting on the atoms, and therefore geometry optimization with dispersion correction leads to a different geometry.⁷² The other alternative approach for including dispersion correction within DFT is known as the van der Waals density functional (vdW-DF),⁷³ in which the non-locality has built in the exchange correlation functional. This approach is more accurate but computationally far more expensive than DFT-D type.

2.1.7 BASIS SET

For solving the electronic structure problem, either within the density functional theory (through the Kohn-Sham equations) or within wavefunction-based methods such as the Hartree-Fock and post-Hartree-Fock approaches, one needs to choose a mathematical representation for the one-electron orbital. The Kohn-Sham equations are solved self-consistently with the electron density generated by the sum of orbital densities. The basis functions $\{\eta\}$ can be either composed of atomic orbitals or plane waves.

Atomic orbitals

Atomic orbitals (AO) are the localized basis functions centered on different atoms. In the early days of quantum chemistry the so-called Slater type orbitals (STOs) were used as basis function due to their similarity with the eigenfunctions of the hydrogen atom. The STOs have the general form,

$$\eta^{STO} = NY_{lm}(\Theta, \phi)\mathbf{r}^{n-1}e^{-\zeta\mathbf{r}} \quad (2.34)$$

where N is the normalization factor, n is the principal quantum number, and Y_{lm} are the spherical harmonics that describe the angular part of the function. ζ controls the width of the orbitals; the large ζ gives a tight function, while a small ζ gives a diffuse function. Such functions that resemble hydrogen atomic orbitals are very suitable for expanding molecular orbitals as they have a correct shape near and far from the nucleus (decay like $e^{-\zeta\mathbf{r}}$). However, from a computational point of view the exponential part is inconvenient in the course of integrals in the self-consistent field procedure, which drastically decreases the speed of computation. For this reason, typically Gaussian type functions, also called as Gaussian type orbitals (GTOs) are used,

$$\eta^{GTO} = NY_{lm}(\Theta, \phi)\mathbf{r}^{2n-2-l}e^{-\zeta\mathbf{r}^2} \quad (2.35)$$

Accordingly, the integrals are much easier to compute because the product of Gaussians are Gaussian; for example, four center integrals can be reduced to one single center. But a single Gaussian does not accurately reproduce the sharp cusp at the center of an exponential, neither does it have the correct asymptotic decay. The GTO inaccuracies can be solved to some extent using linear combinations of Gaussian orbitals, referred as contracted GTOs (CGTOs) which are defined as,

$$\eta^{CGTO} = \sum_{j=1}^J N_j Y_{lm}(\Theta, \phi)\mathbf{r}^{2n-2-l}e^{-\zeta_j\mathbf{r}^2} d_j \quad (2.36)$$

where d_j is the contraction coefficient for the primitive with exponent ζ_j , and J is the total number of gaussian primitives used to represent the basis function. A combination of n Gaussians to mimic an STO is often called as “STO-nG” basis. The STO-3G basis is the minimal basis set, which contracts three Gaussian primitive functions to represent one Slater atomic orbital. Increasing the number of primitive basis functions can enhance the quality of contracted GTO in description of atomic orbitals. For instance, if two sets of basis functions for the description of each atomic orbital are employed, it is called “double- ζ ” or “double-zeta”. This can be further

expanded to “triple- ζ ”, and “quadruple- ζ ”, if three, and four basis functions for each atomic orbital are used, respectively.

In principle, the core electrons attend less in chemical reaction, and it is mainly the valence electrons which contribute to the properties such as chemical bonding or reactivity of chemical systems. Thereby, the so-called “split-valence-type” basis set can be employed, which treats each core AO with a minimal basis set, and the valence AOs with a larger basis set. For example, the split-valence double zeta basis set, 4-31G, employs four gaussian primitives for each core atomic orbital, and two sets of three and one CGTO functions for each valence orbital. This approach is also used for larger molecules, which allows to reduce the computational cost.

Including higher angular momentum orbitals, denoted as polarization functions, can augment the basis sets. For example, the only occupied orbital for the hydrogen atom is s-type, and if the p-type or d-type basis functions are added to the hydrogen atom, it is then considered as polarization basis functions. The basis functions with polarization allow for the atomic electron densities to be polarized, and particularly give a better representation of the electron density in bonding regions where a distortion of the atomic orbitals from their original symmetry occurs. Furthermore, the flexibility of the basis sets can be enhanced by adding extra basis functions (usually of s-type or p-type) with a small exponent ζ to account for the diffusion effect. This can be important for an accurate description of electron density far away from nucleus particularly in anions, and strongly electronegative atoms.⁷²

Plane waves

The other basis function, especially suited for periodic systems in solids are plane waves (PW). They are by nature periodic, and form a complete orthonormal set of functions that can be used to expand the wavefunctions. The Bloch’s theorem facilitates the use of plane waves (PW) as basis functions. According to the Bloch theorem, it is not necessary to determine the electronic wave function everywhere in an infinite periodic system, rather it is sufficient to know it in the unit cell. In neighboring cells, the electronic wave function is exactly the same but for a phase factor due to the translational symmetry, thus the electronic wave function in a periodic system can be written as,

$$\psi_{n,\mathbf{k}}(\mathbf{r}) = u_{n,\mathbf{k}}(\mathbf{r})e^{i\mathbf{k}\cdot\mathbf{r}} \quad (2.37)$$

where \mathbf{k} is a wave vector, and n is the band index. $u_{n,\mathbf{k}}(\mathbf{r})$ is arbitrary function but

always with the periodicity of the primitive cell, i.e.,

$$u_{n,\mathbf{k}}(\mathbf{r} + \mathbf{R}) = u_{n,\mathbf{k}}(\mathbf{r}) \quad (2.38)$$

for any lattice vector \mathbf{R} . Since $u_{n,\mathbf{k}}(\mathbf{r})$ is a periodic function, it can be expanded in terms of Fourier series,

$$u_{n,\mathbf{k}}(\mathbf{r}) = \frac{1}{\sqrt{\Omega}} \sum_{\mathbf{G}} c_{n,\mathbf{k},\mathbf{G}} e^{i\mathbf{G}\cdot\mathbf{r}} \quad (2.39)$$

with Ω as the volume of the direct lattice, and \mathbf{G} is the reciprocal lattice vector that satisfies the requirement,

$$\frac{1}{2\pi} |\mathbf{G}\cdot\mathbf{R}| \in \mathbb{N} \quad (2.40)$$

Thereby, the electronic wavefunction is written as a linear combination of plane waves,

$$\psi_{n,\mathbf{k}}(\mathbf{r}) = \frac{1}{\sqrt{\Omega}} \sum_{\mathbf{G}} c_{n,\mathbf{k},\mathbf{G}} e^{i(\mathbf{k}+\mathbf{G})\cdot\mathbf{r}} \quad (2.41)$$

By the use of Bloch's theorem, the problem of determining the wavefunction over an infinitely large periodic system has been mapped onto the one of solving for the wavefunction in terms of an infinite number of possible values for \mathbf{k} within the first Brillouin zone of the periodic cell. In principle, the electronic wavefunction at each \mathbf{k} -point is an infinite discrete plane wave basis set. In practice, the Fourier expansion of the wave function in Eq. (2.41) is truncated by keeping the maximum value of plane wave vector for the contribution to the kinetic energy less than a given cut-off energy,

$$\frac{1}{2} |\mathbf{k} + \mathbf{G}|^2 \leq E_{cut} \quad (2.42)$$

For metallic systems, where rapid changes in electronic structure may occur along the energy band that crosses the Fermi level, a large number of \mathbf{k} -points are needed to sample the first Brillouin zone. The nonmetallic systems are less sensitive to the quality of \mathbf{k} -point sampling, and it is often sufficient to consider only one particular high symmetry wave vector $\mathbf{k} = 0$, the so called Γ point. The maximum value for reciprocal lattice vector at Γ point is obtained to be $|\mathbf{G}_{max}| = \sqrt{2E_{cut}}$, which corresponds to a sphere with radius \mathbf{G}_{max} centered at the origin of the reciprocal lattice. All reciprocal lattice vectors inside this sphere are included into the basis set. The truncation of the basis set at a finite cutoff energy will lead to an error in the computed total energy and its derivatives, which can be reduced by increasing the value of the cutoff energy in systematic way. In principle, the cutoff energy

should be increased until the calculated total energy converges within the required tolerance.

In contrast to the Gaussian basis functions, the plane waves are orthonormal and site independent and hence are free of basis set superposition errors. Total energies and forces on the atoms can be calculated using computationally efficient fast Fourier transform techniques, which transform a physical quantity from real-space (R-space) to reciprocal-space (G-space). A major disadvantage of PWs over atom-center basis function is that tens or hundreds of thousands of basis functions must be used to get the same level of accuracy as can be obtained with a few hundred Gaussian basis functions. Specifically, a huge number of plane waves are needed to describe regions of high electronic density near atomic cores that leads to the necessity for employing pseudopotentials as will be described in the next section.

2.1.8 PSEUDOPOTENTIAL APPROXIMATION

The plane wave basis set is poorly suited to be used directly for expanding the electronic wave function in Kohn Sham formalism since an extremely large number of them are required to expand the tightly bounded core orbitals, and to follow the rapid oscillations from the atomic valence orbitals in this core region. The oscillations of valence orbitals maintain the orthogonality to the core orbitals, which is required by the exclusion principle. However, it is generally the valence electrons, which actively participate in determining the chemical and physical properties to a much greater extent than the core electrons. It is therefore convenient to approximate the deep core electrons to be “frozen” in their configuration, and to remove all core-electron degrees of freedom. This is done by replacing the strong ion-electron potential by a weaker “pseudopotential”. Thereby a considerable simplification of the computational effort is achieved as the integrals arising from core orbitals are avoided and substituted by corresponding pseudopotential integrals.

In the pseudopotential approach, only the valence electrons are explicitly considered, and the all-electron wave function inside the core region is replaced by a function, which behaves much more smoothly as it has no radial nodes in this region. These new functions are pseudo wavefunctions. The pseudopotential is constructed such that its scattering properties for the pseudo wavefunctions to be the same as the true wavefunctions outside the localized core region which is defined by a certain core radius. The scattering at the core will be different for each angular momen-

tum of the valence wavefunction, and therefore the pseudopotential must be angular momentum dependent. This type of pseudopotential is called non-local pseudopotential, with different projector for different angular momentum components. A local pseudopotential is independent of the angular momentum, and is a function of the distance from the nucleus. One further important criteria is known as norm-conservation, which states that the all-electron valence wavefunction and the pseudo valence wavefunction inside the core region must have the same norm to guarantee that both wavefunctions generate identical electron densities in the outside region. Next to this condition, a suitable pseudopotential should be capable of describing the scattering due to the ion in a variety of atomic environments, a property referred to as transferability. The other desired key property is referred to as softness, which means the softer the pseudopotential is, the smoother the pseudovalence, and consequently a smaller number of plane wave is required to expand the pseudo wavefunction. These properties are closely related to the cutoff radius, and compete with each other. The smaller the value of core radius, the more transferable the potential is. However, the larger cutoff radius results in the softer pseudopotentials, and therefore, a compromise has to be made between the two properties.

The general form of norm-conserving pseudopotential is written as,

$$V^{\text{PS}}(\mathbf{r}) = V_{\text{loc}}^{\text{PS}}(\mathbf{r}) + \sum_{l=0}^{l_{\text{max}}} V_{\text{nl},l}^{\text{PS}}(\mathbf{r})\mathcal{P}_l \quad (2.43)$$

where \mathcal{P}_l is a projection operator on the angular momentum,

$$\mathcal{P}_l = \sum_{m=-l}^{m=l} |l, m\rangle\langle l, m| \quad (2.44)$$

with the spherical harmonics l, m . In Eq. (2.43), $V_{\text{loc}}^{\text{PS}}(\mathbf{r})$ is the local radial part of pseudopotential, which is usually chosen with the largest value of angular momentum that is occupied in the reference configuration,

$$V_{\text{loc}}^{\text{PS}}(\mathbf{r}) = V_{l=l_{\text{max}}}^{\text{PS}}(\mathbf{r}) \quad (2.45)$$

for which a pseudopotential is generated. The nonlocal radial part of pseudopotential, $V_{\text{nl},l}^{\text{PS}}(\mathbf{r})$ is defined as a difference between the original l -dependent pseudopotential $V_l^{\text{PS}}(\mathbf{r})$, and the local part of the pseudopotential. The form of pseudopotential defined in Eq. (2.43) is called semilocal because $V^{\text{PS}}(\mathbf{r})$ is still a local operator with respect to the radius \mathbf{r} , and it is only nonlocal in the angular coordinates. There exist several versions of this class of pseudopotential, which differ from one another by the expressions for the local and non-local functions.⁷⁴⁻⁸¹

2.1.9 NUDGED ELASTIC BAND METHOD FOR FINDING MINIMUM ENERGY PATH

The minimum energy configuration of a system can be found by performing the electronic structure calculation within density functional theory, as reviewed in previous sections. However, another method needs to be employed for determination of the minimum energy path (MEP) taken by a group of atoms from one stable configuration to another. The MEP is defined as a path in coordinate space, which connects two points on a potential surface of the lowest possible energy by passing the saddle point of the PES. This path follows the direction of steepest descent from saddle point downhill to the two adjacent minimums. Such path is frequently used to define a “reaction coordinate” for transitions in chemical reactions, changes in conformation of molecules, or diffusion process in solids.

Many different methods have been proposed for finding the MEPs and saddle points on high dimensional PESs. They are always dealing with some kind of maximization of one degree of freedom and minimization in the other degrees of freedom, followed by the definition of saddle point; a point at which the potential has been maximized along the direction of lowest curvature, and minimized in all other directions. The strategy of traditional methods, referred as “mode following”, is to climb up the potential energy surface from a minimum by following the local normal modes to find saddle points without using any knowledge of the final states. This type of methods are the rational function optimization methods, which uses the second derivative matrix of the potential energy with respect to the nuclear coordinates, the so called Hessian matrix, so as to find the local normal modes of the potential energy surface. Each step in this procedure requires evaluation and inversion of the Hessian matrix, which is often very costly, particularly at the level of density functional theory calculations; and is therefore limited to rather small systems. Accordingly, the methods that only require potential energy and its first derivative with respect to the atom coordinates, i.e, the force on the system, are computationally more feasible.⁸²

Other methods make use of a two point boundary condition to find a MEP between a pair of stable states, *i.e.* both the initial and final configuration which are local minima on the potential energy surface are required. The chain-of-states is the recent class of two point methods which has been developed. There, a chain of images of the system between the two end point configurations is generated and

all the intermediate images are optimized simultaneously. After an optimization calculation acting on all band of images, the images lie near the MEP. An important aspect of this type of methods is that parallel computers or a cluster of networked computers can be used very efficiently for finding the MEP, in contrast to those that are based on a sequential “walk” along the potential energy surface.^{83–93} The following part describes the theoretical basis of the “Nudged Elastic Band” (NEB) method,^{26,27,92} which is an example of chain-of-states methods and some extensions of it, referred as the “Climbing Image Nudged Elastic Band” (CINEB) method.²⁸

In chain-of-states methods, discrete sequence of images consisting of two fixed end points and $N - 1$ intermediate movable images of the system are connected together to trace out the minimum energy path. The images are connected by springs to ensure a quasi-equal spacing along the pathway. An elastic band of images can be denoted by $[\mathbf{R}_0, \mathbf{R}_1, \mathbf{R}_2, \dots, \mathbf{R}_N]$ where $N - 1$ intermediate images are adjusted by the optimization algorithm, while both end points \mathbf{R}_0 , and \mathbf{R}_N are fixed. The straightforward approach is to construct an object function defined as,

$$\mathcal{S}(\mathbf{R}_1, \dots, \mathbf{R}_N) = \sum_{i=1}^{N-1} V(\mathbf{R}_i) + \sum_{i=1}^N \frac{k}{2} (\mathbf{R}_i - \mathbf{R}_{i-1})^2 \quad (2.46)$$

with spring constant k , and to minimize the object function with respect to the intermediate images while keeping the end point images fixed. This is called as plain elastic band method (PEB), which made up $N - 1$ beads and N spring constants. But this band fails in most of situations to provide the MEPs. This is due to two problems known as “corner-cutting”: the spring forces tend to prevent the band following a curved minimum energy path; and “sliding-down”: the true forces along the path causes the images to slide down from high energy regions towards the end points, thereby giving lowest resolution in the region of the saddle point, where they are most needed. Both problems can be solved by projecting out the component of the spring force perpendicular to the path, and the parallel component of the true force coming from the interaction between atoms in the system. To make these projections, the tangent to the path at each image, and every iteration during minimization has to be estimated in order to decompose the true force and spring forces into two components of perpendicular and parallel to the path, respectively. The force acting on image i is given by,

$$\mathbf{F}_i = -\nabla(\mathbf{R}_i) + \mathbf{F}_i^s \quad (2.47)$$

where the first term is the gradient of the energy with respect to the atomic coordi-

nates in the system at image i , and second term is the spring force acting on image i , defined as,

$$\mathbf{F}_i^s \equiv k_{i+1}(\mathbf{R}_{i+1} - \mathbf{R}_i) - k_i(\mathbf{R}_i - \mathbf{R}_{i-1}) \quad (2.48)$$

The tangent at an image i is estimated from two adjacent images along the path, \mathbf{R}_{i+1} and \mathbf{R}_{i-1} , using the normalized line segment between two images,

$$\hat{\tau}_i = \frac{\mathbf{R}_{i+1} - \mathbf{R}_{i-1}}{|\mathbf{R}_{i+1} - \mathbf{R}_{i-1}|} \quad (2.49)$$

but a better way is to bisect the two unit vectors,

$$\tau_i = \frac{\mathbf{R}_i - \mathbf{R}_{i-1}}{|\mathbf{R}_i - \mathbf{R}_{i-1}|} + \frac{\mathbf{R}_{i+1} - \mathbf{R}_i}{|\mathbf{R}_{i+1} - \mathbf{R}_i|} \quad (2.50)$$

and then normalize $\hat{\tau} = \tau/|\tau|$; which ensures the images are equally spaced even in high curvature regions. The force on each image should only contain the parallel component of the spring force, and perpendicular component of the true force;

$$\mathbf{F}_i = -\nabla(\mathbf{R}_i)_\perp + (\mathbf{F}_i^s)_\parallel \quad (2.51)$$

where the perpendicular component of the gradient (true force) is obtained by subtracting out the parallel component,

$$\nabla(\mathbf{R}_i)_\perp = \nabla(\mathbf{R}_i) - \nabla(\mathbf{R}_i) \cdot \hat{\tau}_i \quad (2.52)$$

and the spring force parallel to the band is given by,

$$(\mathbf{F}_i^s)_\parallel = \left[k_{i+1}(\mathbf{R}_{i+1} - \mathbf{R}_i) - k_i(\mathbf{R}_i - \mathbf{R}_{i-1}) \right] \cdot \hat{\tau}_i \quad (2.53)$$

The images along the band are then relaxed to the minimum energy path through the force projection scheme defined in Eq. (2.51). This force projection is referred to as “nudging”, because the spring forces act only along the band, and the potential forces act only perpendicular to the band. These force projections guarantee the decoupling between the dynamics of the path from the chosen discretization for the path. In fact, the spring forces only control the distribution of images within the path as it has no component perpendicular to the path to interfere with the relaxation of the images. Thereby, the convergence to the minimum energy path is independent from the spring stiffness, and the choice of the spring constant is quite arbitrary. The minimization of an elastic band under such force projection is called Nudged Elastic Band (NEB), and when it combines with the bisection of the tangent, it is referred as the “Bisection-Nudged Elastic Band” (B-NEB) method.

The estimation of the tangent within B-NEB method turned out to be inefficient, especially when the covalent bonds are broken and formed. In such cases, the path forms kinks and convergence to the MEP may never be reached. This occurs because the force along the minimum energy path is large compared to the restoring force perpendicular to the path. This problem is then solved by improving the estimation of the local tangent at each image, as is described in the following.

The tangent at an image i is defined by a vector between the image and the neighboring image with the higher energy,

$$\tau_i = \begin{cases} \tau_i^+ & \text{if } E_{i+1} > E_i > E_{i-1} \\ \tau_i^- & \text{if } E_{i+1} < E_i < E_{i-1} \end{cases} \quad (2.54)$$

where

$$\tau_i^+ = \mathbf{R}_{i+1} - \mathbf{R}_i \quad \text{and} \quad \tau_i^- = \mathbf{R}_i - \mathbf{R}_{i-1} \quad (2.55)$$

and $E_i = E(\mathbf{R}_i)$. In special cases that the image i is at maximum or minimum, the tangent is taken to be a weighted average of the vectors to the two neighboring images. If the image i is at a maximum $E_{i+1} < E_i > E_{i-1}$, or at a minimum $E_{i+1} > E_i < E_{i-1}$, the tangent is defined,

$$\tau_i = \begin{cases} \tau_i^+ \Delta E_i^{\max} + \tau_i^- \Delta E_i^{\min} & \text{if } E_{i+1} > E_{i-1} \\ \tau_i^+ \Delta E_i^{\min} + \tau_i^- \Delta E_i^{\max} & \text{if } E_{i+1} < E_{i-1} \end{cases} \quad (2.56)$$

where

$$\begin{aligned} \Delta E_i^{\max} &= \max(|E_{i+1} - E_i|, |E_{i-1} - E_i|) \\ \Delta E_i^{\min} &= \min(|E_{i+1} - E_i|, |E_{i-1} - E_i|) \end{aligned} \quad (2.57)$$

Including this modification in the estimate of tangent to path is referred as ‘‘Improved Tangent-Nudged Elastic Band’’ (IT-NEB) method.⁹⁴

Although the IT-NEB method provides a smooth convergence, however it results in the low resolution of the barrier near to the saddle point, and the interpolation gives an underestimation of the activation energy barrier. This happens because all the intermediate images between two end points are kept equal in distance, and therefore one needs to sample the MEP with numerous intermediate images in between to get a better resolution near the saddle point. However, a small modification to the regular nudged elastic band, referred as to ‘‘Climbing Image Nudged Elastic Band’’ (CI-NEB) method,²⁸ has solved this issue. There, after one or a few relaxation steps of IT-NEB, the image with the highest energy is made to climb up to

converge on the highest saddle point. This is done by removing the spring force acting on this image, and including the inverted true force at this image along the tangent. The total force at this image is not given by Eq. (2.51) but rather by,

$$\mathbf{F}_i^{max} = -\nabla(\mathbf{R}_i^{max})_{\perp} + 2\nabla(\mathbf{R}_i^{max})_{\parallel} \quad (2.58)$$

Therefore, the climbing image does not feel the spring forces along the band, and accordingly the spacing of images on either side of this image will differ. In this way, the inverted component of the true force drives this image right to the saddle point along the band, and its convergence results to the activation energy precisely with insignificant additional computational effort.

In this work, the CI-NEB method within density functional theory, implemented in CP2K⁹⁵ code, is employed to evaluate the rotational potential energy surfaces of the methyl rotors. Once the PES of the methyl rotors is known, the rotational energy levels are obtained by the numerical solution of the corresponding time independent Schrödinger equation, as will be discussed in next sections.

2.1.10 NUMERICAL WAVEFUNCTION OF 1-DIMENSIONAL CH₃ ROTORS

The dynamics of a methyl group can be represented by a one-dimensional rotor with one single rotational angle. The quantized rotational energy levels of the methyl rotor are calculated under the assumption that the environment can be represented by a potential, which is a function of methyl rotational angle. The rotor levels are given by the solution of the one-dimensional time independent Schrödinger equation. Although, the majority of the experimental spectra can be explained within single methyl rotation; however there exists systems whose their experimentally measured multiplet tunneling peaks arising from one crystallographically distinct methyl groups are beyond one single rotor description. In such cases, rotor-rotor coupling should be taken into account, and therefore the two-dimensional Schrödinger equation with a coupling rotational potential as a function of two rotational angles has to be solved. Here, the methods used for solving numerically the one- and two-dimensional Schrödinger equation are discussed, follows the notations of the main references. In the context of this work, the variables x and y stand for the rotational angles, and the mass m is replaced by the moment of inertia, I , for three protons of the methyl rotor.

One dimensional Schrödinger equation

Since Erwin Schrödinger formulated his famous equation 90 years ago, there have been various analytical and numerical methods proposed for the solution of this central quantum mechanics equation. The numerical approaches to one-dimensional solutions are being for example, finite difference method,⁹⁶ b-spline,⁹⁷ the Fourier grid representation,⁹⁸ the shooting method,⁹⁹ and Numerov method.³⁴ They differ in the level of accuracy, computational speed, and the simplicity of their representations. In this work, the matrix representation of the Numerov method is used for the calculation of energies and wavefunctions, in which the kinetic energy operator is discretized on a lattice and the potential energy operator is a diagonal matrix of the potential energy evaluated at each lattice point. The high-accuracy solutions are obtained using the matrix diagonalization.

The Numerov method, developed by the Russian astronomer Boris Vasil'evich Numerov, is a specialized integration method for numerically integrating ordinary differential equations of second-order, in which the first-order term does not appear. An example of such differential equations is the time-independent one-dimensional Schrödinger equation,

$$-\frac{\hbar^2}{2m} \frac{d^2\psi(x)}{dx^2} + V(x)\psi(x) = E\psi(x) \quad (2.59)$$

where $\psi(x)$ is the wavefunction, and $V(x)$ is the potential energy. This equation can be rewritten of the form,

$$\psi^{(2)}(x) = f(x)\psi(x) \quad (2.60)$$

where

$$\begin{aligned} \psi^{(n)} &= \frac{d^n}{dx^n} \psi(x) \\ f(x) &= -\frac{2m}{\hbar^2} [E - V(x)] \end{aligned} \quad (2.61)$$

A Taylor series expansions of the wave function $\psi(x)$ gives,

$$\psi(x \pm h) = \psi(x) \pm h\psi^{(1)}(x) + \frac{1}{2!}h^2\psi^{(2)}(x) \pm \frac{1}{3!}h^3\psi^{(3)}(x) + \frac{1}{4!}h^4\psi^{(4)}(x) + \dots \quad (2.62)$$

where $x_n = x_0 + nh$ and h is the spacing between points in the grid. It follows that,

$$\psi(x+h) + \psi(x-h) = 2\psi(x) + h^2\psi^{(2)}(x) + \frac{1}{12}h^4\psi^{(4)}(x) + O(h^6) \quad (2.63)$$

To rearrange the above equation, the second derivative of the wave function can be written as,

$$\psi^{(2)}(x) = \frac{\psi(x+h) + \psi(x-h) - 2\psi(x)}{h^2} - \frac{1}{12}h^2\psi^{(4)}(x) + O(h^4) \quad (2.64)$$

In order to evaluate the term involving the 4th derivative in Eq. (2.64), act on Eq. (2.60) with $(1 + \frac{1}{12}h^2\frac{d^2}{dx^2})$,

$$(1 + \frac{1}{12}h^2\frac{d^2}{dx^2})[\psi^{(2)}(x)] = (1 + \frac{1}{12}h^2\frac{d^2}{dx^2})[f(x)\psi(x)] \quad (2.65)$$

which gives

$$\psi^{(2)}(x) + \frac{1}{12}h^2\psi^{(4)}(x) = f(x)\psi(x) + \frac{1}{12}h^2\frac{d^2}{dx^2}[f(x)\psi(x)] \quad (2.66)$$

Substituting Eq. (2.66) into Eq. (2.64),

$$f(x)\psi(x) + \frac{1}{12}h^2\frac{d^2}{dx^2}[f(x)\psi(x)] = \frac{\psi(x+h) + \psi(x-h) - 2\psi(x)}{h^2} + O(h^4) \quad (2.67)$$

The second term in the above equation can be evaluated by using finite difference formula. This introduces an error of order $\mathcal{O}(h^2)$, but since it is multiplied by h^2 when substituted in Eq. (2.67), the accuracy of $\mathcal{O}(h^4)$ is preserved,

$$\frac{d^2}{dx^2}[f(x)\psi(x)] = \frac{f(x+h)\psi(x+h) + f(x-h)\psi(x-h) - 2f(x)\psi(x)}{h^2} + \mathcal{O}(h^2) \quad (2.68)$$

Substituting Eq. (2.68) into Eq. (2.67) yields an equation to $\mathcal{O}(h^4)$,

$$\begin{aligned} f(x)\psi(x) + \frac{f(x+h)\psi(x+h) + f(x-h)\psi(x-h) - 2f(x)\psi(x)}{12} \\ = \frac{\psi(x+h) + \psi(x-h) - 2\psi(x)}{h^2} \end{aligned} \quad (2.69)$$

This can be rearranged into the form,

$$\frac{\psi_{i+1} + \psi_{i-1} - 2\psi_i}{h^2} = \frac{1}{12}f_{i+1}\psi_{i+1} + \frac{10}{12}f_i\psi_i + \frac{1}{12}f_{i-1}\psi_{i-1} \quad (2.70)$$

where

$$\begin{aligned} f_{i-1} &\equiv f(x-h), & f_i &\equiv f(x), & f_{i+1} &\equiv f(x+h) \\ \psi_{i-1} &\equiv \psi(x-h), & \psi_i &\equiv \psi(x), & \psi_{i+1} &\equiv \psi(x+h) \end{aligned} \quad (2.71)$$

Recall from Eq. (2.61) that,

$$f_{i-1} = -\frac{2m}{\hbar^2}(E - V_{i-1}), \quad f_i = -\frac{2m}{\hbar^2}(E - V_i), \quad f_{i+1} = -\frac{2m}{\hbar^2}(E - V_{i+1}) \quad (2.72)$$

Therefore, the Schrödinger equation can be written into the form,

$$-\frac{\hbar^2}{2m} \frac{\psi_{i-1} - 2\psi_i + \psi_{i+1}}{h^2} + \frac{V_{i-1}\psi_{i-1} + 10V_i\psi_i + V_{i+1}\psi_{i+1}}{12} = E \frac{\psi_{i-1} + 10\psi_i + \psi_{i+1}}{12} \quad (2.73)$$

If ψ is represented as the column vector $(\dots, \psi_{i-1}, \psi_i, \psi_{i+1}, \dots)$, and defining matrices,

$$A = \frac{(\mathbb{I}_{-1} - 2\mathbb{I}_0 + \mathbb{I}_1)}{h^2}$$

$$B = \frac{(\mathbb{I}_{-1} + 10\mathbb{I}_0 + \mathbb{I}_1)}{12} \quad (2.74)$$

$$V = \text{diag}(\dots, V_{i-1}, V_i, V_{i+1}, \dots)$$

where \mathbb{I}_p is a matrix of 1s along the p th diagonal, and zeros elsewhere; this becomes the matrix representation of the one-dimensional Schrödinger equation,

$$-\frac{\hbar^2}{2m} A\psi + BV\psi = EB\psi \quad (2.75)$$

and multiplying by B^{-1} gives,

$$-\frac{\hbar^2}{2m} B^{-1}A\psi + V\psi = E\psi \quad (2.76)$$

where the first term is the Numerov representation of the kinetic energy operator. On an N -point grids, the boundary conditions are implemented by taking the square matrices A and B to be $N \times N$, which effectively implied to a boundary condition $\psi_0 = \psi_{N+1} = 0$. The periodic boundary conditions can be applied by $A_{1,N} = A_{N,1} = 1/d^2$ and $B_{1,N} = B_{N,1} = 1/12$. An in-house Fortran code is developed to solve the Hamiltonian, Eq. (2.76), with the calculated one-dimensional rotational potential of methyl rotor from DFT to obtain the eigenvalues and eigenfunctions.

Two-dimensional Schrödinger equation

For solving a two dimensional Schrödinger equation, there are variational and finite difference methods. In the variational methods, a trial wavefunction composing of many terms is used, and the coefficients are found such that the expectation value of the energy is minimized. Such types of methods are complicated as they lead to the evaluation of difficult integrals. In the finite difference methods, a mesh of points dots the space with a fixed local distance between adjacent points, and the discrete solution is sought at each point of the mesh. The basic idea is to replace

the continues partial differential equation with a discrete approximation using the Taylor expansion, such that the Schrödinger equation is reduced to a set of linear equations. In this approach, the two-dimensional problem can be treated by the discretization of either both variables x and y at once¹⁰⁰⁻¹⁰² or one by one.³⁵ In the latter approach, which is employed in this work, the two dimensional problem is first partially discretized with respect to one variable and then the partial differential equation is transformed into a system of ordinary differential equations of the second order that can be solved by the classical Numerov method,³⁵ described in the previous section, or the other methods such as the exponentially fitted¹⁰³ and the trigonometrically fitted modified Numerov method.¹⁰⁴

The two dimensional time independent Schrödinger equation is defined as,

$$-\frac{1}{2} \frac{\partial^2 \psi(x, y)}{\partial x^2} - \frac{1}{2} \frac{\partial^2 \psi(x, y)}{\partial y^2} + V(x, y)\psi(x, y) = E\psi(x, y) \quad (2.77)$$

where E is the energy eigenvalue, $V(x, y)$ is the potential, and $\psi(x, y)$ the wavefunction. For the sake of simplicity, this equation is written in atomic units, where \hbar and m are set to one. Both variables x and y are considered in the interval $[-R_x, R_x]$ and $[-R_y, R_y]$, respectively. The boundary conditions are defined as,

$$\begin{aligned} \psi(x, -R_y) = 0 \quad \text{and} \quad \psi(x, R_y) = 0 \\ \psi(-R_x, y) = 0 \quad \text{and} \quad \psi(R_x, y) = 0 \end{aligned} \quad (2.78)$$

As it was pointed out before, the partial discretization is first applied with respect to the y variable,

$$-R_y = y_{-N}, y_{-N+1}, \dots, y_{-1}, y_0, y_1, \dots, y_{N-1}, y_N = R_y \quad (2.79)$$

where $y_{j+1} - y_j = h_y = R_y/N$. Using the Taylor series expansions of the wave function, the second partial derivative of the wave function can be approximated as,

$$\frac{\partial^2 \psi}{\partial y^2} = \frac{\psi(x, y_{j+1}) - 2\psi(x, y_j) + \psi(x, y_{j-1}))}{h_y^2} \quad (2.80)$$

Substituting the Eq. (2.80) into Eq. (2.77) gives,

$$\frac{\partial^2 \psi}{\partial x^2} = -\frac{1}{h_y^2} \psi(x, y_{j+1}) - 2\left[E - V(x, y_j) - \frac{1}{h_y^2}\right] \psi(x, y_j) - \frac{1}{h_y^2} \psi(x, y_{j-1}) \quad (2.81)$$

with

$$\psi(-R_x, y_j) = 0 \quad \text{and} \quad \psi(R_x, y_j) = 0 \quad (2.82)$$

for $j = -N+1, \dots, 0, \dots, N-1$. The vector $\Psi(x)$ with $k = 2N-1$ length is defined as,

$$\Psi(x) = \begin{pmatrix} \psi(x, y_{-N+1}) \\ \psi(x, y_{-N+2}) \\ \vdots \\ \psi(x, y_0) \\ \vdots \\ \psi(x, y_{N-2}) \\ \psi(x, y_{N-1}) \end{pmatrix}_{k \times 1} \quad (2.83)$$

Then the Eq. (2.77) can be written as,

$$\frac{\partial^2 \Psi}{\partial x^2} = -S(x)\Psi(x) \quad (2.84)$$

with $\Psi(-R_x) = 0$, and $\Psi(R_x) = 0$, and $S(x)$ as a $k \times k$ matrix,

$$S(x) = 2EI - 2V(x) + \frac{1}{h_y^2}M \quad (2.85)$$

In the above equation, $V(x)$ is a diagonal $k \times k$ matrix with diagonal elements,

$$V(x, y_{-N+1}), V(x, y_{-N+2}), \dots, V(x, y_{N-1}) \quad (2.86)$$

and the matrix M is tridiagonal with diagonal elements -2 and off diagonal elements 1 .

Turn to the discretization with respect to the other variable; the variable x is taken in the interval $[-R_x, R_x]$ with boundary conditions $\Psi(-R_x) = 0$ and $\Psi(R_x) = 0$;

$$-R_x = x_{-N}, x_{-N+1}, \dots, x_{-1}, x_0, x_1, \dots, x_{N-1}, x_N = R_x \quad (2.87)$$

where $x_{j+1} - x_j = h_x = R_x/N$.

In previous section, it is shown that the classical Numerov method for ordinary differential equations of the form $d^2\psi(x)/dx^2 = f(x)\psi(x)$ yields,

$$\psi_{n+1} + \psi_{n-1} - 2\psi_n = h^2 [b_0 f_{n+1} \psi_{n+1} + b_1 f_n \psi_n + b_0 f_{n-1} \psi_{n-1}] \quad (2.88)$$

where the coefficients are,

$$b_0 = \frac{1}{12} \quad \text{and} \quad b_1 = \frac{10}{12} \quad (2.89)$$

To apply Eq. (2.88) to Eq. (2.84),

$$\psi_{n+1} + \psi_{n-1} - 2\psi_n = -h_x^2 [b_0 S_{n+1} \psi_{n+1} + b_1 S_n \psi_n + b_0 S_{n-1} \psi_{n-1}] \quad (2.90)$$

and substitution of $S(x)$ from Eq. (2.85) into the above equation leads to the following generalized eigenvalue problem,

$$\begin{aligned}
\psi_{n+1} + \psi_{n-1} - 2\psi_n = & \\
& -2h_x^2 E(b_0\Psi_{n+1} + b_1\Psi_n + b_0\Psi_{n-1}) \\
& +2h_x^2 E(b_0V_{n+1}\Psi_{n+1} + b_1V_n\Psi_n + b_0V_{n-1}\Psi_{n-1}) \\
& -b_0\frac{h_x^2}{h_y^2}M(\Psi_{n+1} + \Psi_n + \Psi_{n-1})
\end{aligned} \tag{2.91}$$

Eq. (2.91) can be represented in terms of matrices,

$$\mathbb{A}\Psi = -2h_x^2 E\mathbb{B}\Psi + 2h_x^2 \mathbb{B}\mathbb{V}\Psi - \frac{h_x^2}{h_y^2}\mathbb{C}\mathbb{B}\Psi \tag{2.92}$$

To rearrange the above equation, the final general form of eigenvalue equation obtained as,

$$-\frac{1}{2h_x^2}\mathbb{B}^{-1}\mathbb{A}\Psi - \frac{1}{2h_y^2}\mathbb{B}^{-1}\mathbb{C}\mathbb{B}\mathbb{A}\Psi + \mathbb{V}\Psi = E\Psi \tag{2.93}$$

where Ψ is a $k^2 = (2N - 1)^2$ length vector,

$$\Psi = (\Psi_{-N+1}, \Psi_{-N+2}, \dots, \Psi_0, \dots, \Psi_{N-1})^T \tag{2.94}$$

and the matrices \mathbb{A} , \mathbb{C} , and \mathbb{B} are defined as,

$$\begin{aligned}
\mathbb{A}_{k^2 \times k^2} &= \mathbb{P}_{k \times k} \otimes \mathbb{I}_{k \times k} \\
\mathbb{C}_{k^2 \times k^2} &= \mathbb{I}_{k \times k} \otimes \mathbb{P}_{k \times k} \\
\mathbb{B}_{k^2 \times k^2} &= \mathbb{Q}_{k \times k} \otimes \mathbb{I}_{k \times k}
\end{aligned} \tag{2.95}$$

where the matrix elements of the \mathbb{I} , \mathbb{P} , and \mathbb{Q} are,

$$\mathbb{I}_{k \times k} = \begin{pmatrix} 1 & 0 & 0 & \dots & 0 \\ 0 & 1 & 0 & \dots & 0 \\ 0 & 0 & 1 & \dots & 0 \\ \vdots & \vdots & \vdots & \ddots & \vdots \\ 0 & 0 & 0 & \dots & 1 \end{pmatrix}_{k \times k} \tag{2.96}$$

$$\mathbb{P}_{k \times k} = \begin{pmatrix} -2 & 1 & 0 & \dots & 0 \\ 1 & -2 & 1 & \dots & 0 \\ 0 & 1 & -2 & \dots & 0 \\ \vdots & \vdots & \vdots & \ddots & \vdots \\ 0 & 0 & 0 & \dots & -2 \end{pmatrix}_{k \times k} \tag{2.97}$$

$$\mathbb{Q}_{k \times k} = \begin{pmatrix} b_1 & b_0 & 0 & \dots & 0 \\ b_0 & b_1 & b_0 & \dots & 0 \\ 0 & b_0 & b_1 & \dots & 0 \\ \vdots & \vdots & \vdots & \ddots & \vdots \\ 0 & 0 & 0 & \dots & b_1 \end{pmatrix}_{k \times k} \quad (2.98)$$

The potential in Eq. (2.93) is a diagonal matrix that has blocks as,

$$\mathbb{V}_{k^2 \times k^2} = \begin{pmatrix} \boxed{V(x_{-N+1})}_{k \times k} & 0 & 0 & \dots & 0 \\ 0 & \boxed{V(x_{-N+2})}_{k \times k} & 0 & \dots & 0 \\ 0 & 0 & \boxed{V(x_{-N+3})}_{k \times k} & \ddots & 0 \\ \vdots & \vdots & \vdots & \ddots & \vdots \\ 0 & 0 & 0 & 0 & \boxed{V(x_{N-1})}_{k \times k} \end{pmatrix} \quad (2.99)$$

The matrix elements of the first block, for instance, are defined as

$$\boxed{V(x_{-N+1})}_{k \times k} = \begin{pmatrix} V(x_{-N+1}, y_{-N+1}) & 0 & 0 & \dots & 0 \\ 0 & V(x_{-N+1}, y_{-N+2}) & 0 & \dots & 0 \\ 0 & 0 & V(x_{-N+1}, y_{-N+3}) & 0 & 0 \\ \vdots & \vdots & \vdots & \ddots & \vdots \\ 0 & 0 & 0 & 0 & V(x_{-N+1}, y_{N-1}) \end{pmatrix} \quad (2.100)$$

The periodic boundary conditions are then applied using the same hints given for solving one-dimensional equation within Numerov method;³⁴ i.e., $\mathbb{P}_{1,k} = \mathbb{P}_{k,1} = 1$, and $\mathbb{Q}_{1,k} = \mathbb{Q}_{k,1} = b_0$. These matrices are real, symmetric, sparse, and very large even for small value of N , for example; $k^2 \times k^2 = 9801 \times 9801$ for $N=50$. Therefore, they have to be treated as sparse matrices in terms of storage and computational cost.

An in-house Python^{105,106} code is developed to construct and solve the Eq. (2.93) with the two dimensional DFT energy profile of methyl rotors. In the next two chapters, the quantum rotational levels of methyl rotors will be discussed in details.

2.2 AB-INITIO MOLECULAR DYNAMICS APPROACH COMBINED WITH SEMICLASSICAL METHOD

The other alternative approaches to the calculation of tunneling splittings are provided by the application of the correspondence principle, which states that the laws of quantum mechanics must reduce to those of classical mechanics in the limit

$\hbar \rightarrow 0$. One such semiclassical method is the WKB approximation, after G. Wentzel, H. A. Kramers and L. Brillouin.¹³⁻¹⁵ In the WKB approximation the wavefunction is constructed in the classically-allowed and forbidden regions separately, which are then matched at the so-called classical “turning-points”. The wavefunction is proportional to $e^{iS(x)/\hbar}$, in which the high orders of \hbar in $S(x)$ are neglected and $S(x) = \int dx \sqrt{2m[E - V(x)]}$ is the classical action, which becomes imaginary in classically-forbidden regions. In such manner the WKB approximation extends classical mechanics to treat tunneling phenomena.^{17,20} However, easy application of this method is restricted to one-dimensional problem. There do exist the multidimensional semiclassical theories that describe how classical trajectories tunnel, e.g., the instanton theory as will be reviewed in section 2.3 and the Makri-Miller¹⁹ model of tunneling, which can be implemented in a classical trajectory simulation of full molecular dynamics. In the latter approach, the classical trajectory evolving in one classically-allowed region of space will, at specific times, have a probability for making an instantaneous transition to another allowed region of space. The probability of tunneling through the barrier is calculated under the WKB approximation.

In a study done by Ootani et al.,¹⁸ the semiclassical Makri-Miller approach is combined with ab-initio molecular dynamics (AIMD) to estimate tunneling splitting in polyatomic molecules. In the AIMD, the nuclear motions are evolved by integrating the Newton’s equation of motion, while forces acting on the nuclei are computed from electronic structure calculations that are performed “on-the-fly”, as the molecular dynamics trajectory is generated. In this way, the electrons are treated quantum mechanically, while the nuclear motion is treated by classical mechanics. The Makri-Miller¹⁹ model of tunneling is therefore combined with the AIMD to include the quantum effects associated with the nuclear motion and tunneling.

This approach is examined by reproducing the results for the estimation of tunneling splitting in the umbrella inversion of Ammonia. The obtained results, given in Appendix D, are in good agreement with those of Ootani et al.¹⁸ The following sections present the basic concepts of the method.

2.2.1 WENTZEL-KRAMERS-BRILLOUIN (WKB) APPROXIMATION

In general, the WKB approximation is a method for finding approximate solutions to the linear, second order differential equations with spatially varying coefficients;

a class that includes the time independent one-dimensional Schrödinger equation,

$$-\frac{\hbar^2}{2m} \frac{d^2\psi}{dx^2} + V(x)\psi = E\psi \quad (2.101)$$

in which the particle moves along a slowly varying one-dimensional potential $V(x)$. The fact that the potential is “slowly varying” means that the local wave number,

$$k(x) = \frac{1}{\hbar} \sqrt{2m[E - V(x)]}, \quad (2.102)$$

is expected to change only slightly over one de Broglie wave length, λ . The criterion of validity for the WKB approximation is written as

$$\left| \frac{\Delta k}{k} \right| \approx \left| \frac{k'\lambda}{k} \right| = \left| \frac{k'}{k^2} \right| \ll 1 \quad (2.103)$$

where $\Delta k = |k(x + \lambda/2) - k(x - \lambda/2)|$ is the variation of the local wave vector. In the other words, the potential must change slowly in comparison with the wavelength λ in a way that it is essentially constant over many wavelengths.

The WKB ansatz for the wave function is,

$$\psi(x) = Ae^{\frac{i}{\hbar}S(x)} \quad (2.104)$$

where A is an arbitrary constant and $S(x)$ is a complex function. Inserting the ansatz of Eq. (2.104) into the Schrödinger equation gives,

$$\left(\frac{dS}{dx}\right)^2 - i\hbar \frac{d^2S}{dx^2} - k^2(x)\hbar^2 = 0 \quad (2.105)$$

where,

$$k^2(x) = \frac{2m}{\hbar^2} [E - V(x)] \quad (2.106)$$

The Eq. (2.105) is the Hamilton-Jacobi equation in quantum mechanics, which reduces to the classical Hamilton-Jacobi equation in the limit $\hbar \rightarrow 0$. So far, no approximation has been made, and this equation is equivalent to the original Schrödinger equation. However, this is a non-linear equation which is in fact more complicated than the original Eq. (2.101) itself, and hence has to be solved approximately. In the WKB approximation, \hbar is treated as a parameter of smallness and expand the function $S(x)$ in power series of \hbar ,

$$S(x) = S_0(x) + \hbar S_1(x) + \hbar^2 S_2(x) + \dots \quad (2.107)$$

Usually the first two terms of the expansion are kept, *i.e.*,

$$S(x) = S_0(x) + \hbar S_1(x) \quad (2.108)$$

which leads to the so called the first-order WKB approximation. Substituting Eq. (2.108) into Eq. (2.105) gives,

$$\left(\frac{dS_0(x)}{dx}\right)^2 - k^2(x)\hbar^2 + \left[2\frac{dS_0(x)}{dx}\frac{dS_1(x)}{dx} - i\frac{d^2S_0(x)}{dx^2}\right]\hbar = 0 \quad (2.109)$$

in which the higher powers of \hbar are neglected. For the above equation to be valid, the coefficient of each power of \hbar must vanish separately, therefore,

$$\left(\frac{dS_0(x)}{dx}\right)^2 - k^2(x)\hbar^2 = 0 \quad (2.110)$$

and

$$2\frac{dS_0(x)}{dx}\frac{dS_1(x)}{dx} - i\frac{d^2S_0(x)}{dx^2} = 0 \quad (2.111)$$

From Eq. (2.110),

$$\begin{aligned} S_0(x) &= \pm \int dx \hbar k(x) \\ &= \pm \int dx \sqrt{2m(E - V(x))} \end{aligned} \quad (2.112)$$

and when the above result for $S_0(x)$ is inserted into Eq. (2.111),

$$S_1(x) = \frac{i}{2}\ln(k(x)) \quad (2.113)$$

Putting all together, the first-order of the linearly independent WKB wave functions are

$$\psi_{WKB}^{(1)}(x) = \frac{1}{\sqrt{k(x)}} \left[C_1 \exp\left(+i \int_x dx' k(x')\right) + C_2 \exp\left(-i \int_x dx' k(x')\right) \right] \quad (2.114)$$

In the classically-allowed region, where $E > V(x)$, the local wave number is real, and the wavefunction is an oscillatory function of x . In the classically-forbidden region, where $E < V(x)$, the local wave number is imaginary, i.e., $k(x) = i\gamma(x)$; and the wavefunctions exponentially decay, and have the asymptotic behavior.

The Eq. (2.114) gives an approximate solution to the one-dimensional Schrödinger equation in any region in which the condition of validity, Eq. (2.103), holds. The method fails if $k(x)$ changes too rapidly or if it is zero, which occurs at the border of two classically-allowed and forbidden regions, *i.e.*, at the turning points as the classical particle has zero speed. This is a serious difficulty because the wave function diverges at the turning points and the usual procedure of matching wavefunctions and their derivatives cannot be followed. A fairly complex matching formalism of the wave functions in the classically-allowed and forbidden regions at turning points

has been developed that yields the connection formulas and WKB quantization condition.¹⁰⁷⁻¹¹⁰

In the classical framework, a particle which hits the barrier is always transmitted or reflected, determined by whether the particle's kinetic energy is greater or less than the barrier height. But whereas in quantum mechanics there is a probability that a particle, which is represented by a wavefunction, can penetrate the barrier and appear on the other side even if its energy is less than the potential energy. By convention, the tunneling probability of a particle with the total energy E through the barrier is defined as the ratio of the transmitted current density to the incident current density. Accordingly, the most common WKB expression for tunneling probability is obtained as,

$$T_{WKB}(E) = e^{-2\theta} \quad (2.115)$$

with

$$\theta = \exp\left[\frac{1}{\hbar} \int_{x_1}^{x_2} dx \sqrt{2m(V(x) - E)}\right] \quad (2.116)$$

where x_1 and x_2 are the classical turning points, and $x_1 - x_2$ corresponds to the barrier length. It should be stressed that this expression is only valid if the energy is not near or above the top of the barrier ($E \ll V(x)$). This equation shows the explicit exponential sensitivity of the tunneling effect to the mass of the particle and the shape of potential energy surface.

The tunneling probability in one-dimensional systems can be estimated using the WKB expression, in which the particle reaches the turning point at a constant position with a constant time interval. But in multidimensional systems, due to the energy transfer between tunneling and vibrational modes, the turning points and time interval of hitting the barrier change. In the next section, the inclusion of the multidimensional effects within the semiclassical method of Makri-Miller is discussed.

2.2.2 THE SEMICLASSICAL TUNNELING METHOD OF MAKRI AND MILLER

In this method, a trajectory is propagated in a classically-allowed region around one of its minima. The trajectory is monitored and each time it reaches a classical turning point, the tunneling probability of crossing the barrier, $\exp(-\theta)$, is calculated

under the WKB approximation. θ is the action integral through the barrier,

$$\theta(t_n) = \frac{1}{\hbar} \int_0^{\xi_n} \sqrt{2m(V(\xi) - V_n)} d\xi \quad (2.117)$$

where t_n corresponds to the times that the classical trajectory hits the barrier at the n th turning point and ξ_n is the value of tunneling coordinate ξ at which the integrand of the above equation is zero, *i.e.*, the value for which the tunneling trajectory reaches the other classically-allowed region of space. $V(\xi)$ is the potential energy at ξ and V_n is the potential energy of the trajectory at the n th turning point.

To include the multidimensional effects, the *net tunneling amplitude* needs to be averaged over many different trajectories, yielding different tunneling amplitudes,

$$S_{net}(t) = \sum_n h(t - t_n) \exp[-\theta(t_n)] \quad (2.118)$$

where $h(t - t_n)$ is the Heaviside step function ($= 1$ if $t > t_n$, $= 0$ if $t < t_n$). The tunneling splitting ΔE is then expressed by the slope of the average net tunneling probability, *i.e.*,

$$\Delta E = 2\hbar \frac{d}{dt} \langle S_{net}(t) \rangle \quad (2.119)$$

where the bracket implies an average over many the trajectories.

The most critical part of such semiclassical treatment of tunneling is the choice of the tunneling direction; the determination of the tunneling path and turning point in multidimensional space. The most easiest and simplest choice in general for the tunneling direction, $\hat{\mathbf{n}}_0$, is a straight line that connects the manifolds that correspond to the initial and final state in the shortest way, which however, may not always be the best choice. The turning points can be determined by monitoring the component of momentum \mathbf{p} along the tunneling path direction $\hat{\mathbf{n}}_0$. Each time the trajectory experiences a classical turning point, $\mathbf{p} \cdot \hat{\mathbf{n}}_0$ goes to zero, which corresponds to the times that the component of the coordinate vector \mathbf{q} goes through a relative maximum. More details concerning the numerical implementation and application of this method to the umbrella inversion of Ammonia can be found in Appendix D.

2.3 RING-POLYMER INSTANTON METHOD

The alternative semiclassical approach to the tunnel splitting calculation is the ring polymer instanton method.^{17,20} The instanton method is based on the discretized imaginary time path integral approach, which gives an expression for the tunnel splitting in terms of a minimum on the potential energy surface of a linear polymer.

The Linear polymer is a section cut out of a ring polymer consisting of an infinite number of beads. The term “instanton” refers to the periodic orbit in pure imaginary time. In this approach, the need of taking the zero temperature limit, or the infinity limit of the imaginary time duration of the instanton theory is replaced with the imaginary time duration (τ) to be long in combination with the time increment ($\Delta\tau$) to be short enough.

The method is examined by reproducing the results of the tunnel splitting in a double well system. In this regard, an in-house python code based on the ring polymer instanton method is developed. The obtained results are in agreement with those of Richardson et al.,¹⁷ given in Appendix E. The accuracy of the method is investigated for addressing the tunnel splitting in one-dimensional three-fold cosine potentials (see Appendix E). In the next sections, the most important concepts for derivation of the instanton method within the one-dimensional double potential wells are presented. The generalization of the approach to multidimensional systems and multi degenerate wells is straightforward and can be found in the main references.^{16,17,20}

2.3.1 PATH-INTEGRAL FORMULATION OF TUNNELING SPLITTINGS

In the scope of path integral formalism, the ground state tunnel splitting can be derived from the zero temperature limit of the quantum partition function. Consider the problem of tunneling splitting of energy levels in a one-dimensional symmetric double potential well. When the barrier between two minima is large enough such that both potential wells are essentially isolated from one another, the tunneling between two symmetric wells can be neglected. Thereby, each well can be approximated by a harmonic well. The solutions to the Schrödinger equation in such non-tunneling system yields a double degenerate ground state with energy E_0 , corresponding to the Gaussians ψ_1 , and ψ_2 being localized in one or the other of the wells. In the tunneling system, the quantum particle tunnels through the barrier between two potential wells, assuming the height of tunneling barrier to be low enough. The total wave functions are then a linear combination of the wavefunctions corresponding to the two separate wells; $\Psi_{\pm} = \psi_1 \pm \psi_2$, and the degenerate ground energy splits apart by tunneling; $E_{\pm} = E_0 \pm \Delta/2$ where the energy difference, Δ , is called tunneling splitting.

The instanton theory of tunneling splitting is based on a premise,

$$\lim_{\beta \rightarrow \infty} \frac{Q(\beta)}{Q_0(\beta)} \approx \frac{\exp[-\beta(E_0 - \Delta/2)] + \exp[-\beta(E_0 + \Delta/2)]}{2\exp[-\beta E_0]} = \cosh\left(\frac{\beta\Delta}{2}\right) \quad (2.120)$$

where $Q(\beta)$, and $Q_0(\beta)$ are the partition function of the system in the non-tunneling, and tunneling cases, respectively. It is assumed that $\beta = 1/k_B T$ is large, *i.e.*, the temperature is very low such that only the lowest energy states contribute to the partition function. The instanton theory gives an expression for Δ by representing the partition functions in terms of ring polymers as is discussed in the following.

The exact partition function is the trace of the quantum Boltzmann operator. For large and anharmonic systems, it is not possible to enumerate the energy levels. A transformation is required to ease the computation; which is provided by the path-integral representation. The Boltzmann operator can be expanded in any complete set of states, for instance in the position representation as

$$Q(\beta) = \text{tr}[e^{-\beta\hat{H}}] = \int_{-\infty}^{+\infty} dx \langle x | e^{-\beta\hat{H}} | x \rangle \quad (2.121)$$

where the Hamiltonian for one dimensional systems is of the form,

$$\hat{H} = \frac{\hat{p}^2}{2m} + \hat{V} \quad (2.122)$$

where $\hat{p} = -i\hbar d/dx$, and $\hat{V} = V(\hat{x})$. In general, the exponential of Hamiltonian in Eq. (2.121) cannot be evaluated in either position or momentum representation because \hat{x} and \hat{p} do not commute. However, an approximation of the Boltzmann operator is possible by using the split-operator method or Trotter splitting,

$$\langle x | e^{-\beta\hat{H}} | x \rangle \approx \langle x | e^{-\beta\frac{\hat{V}}{2}} e^{-\beta\hat{T}} e^{-\beta\frac{\hat{V}}{2}} + O(\beta^3) | x \rangle \quad (2.123)$$

where an error of order β^3 is introduced by the Trotter decomposition. In the high temperature limit, this error diminishes, however the interest of this context is the low temperature regime as the quantum nuclear dynamical effects are apparent. One way to calculate the trace efficiently and yet accurately is to split the Boltzmann operator into N equally spaced steps in imaginary time of length $\beta_N \hbar$, with $\beta_N = \beta/N$,

$$Q(\beta) = \text{tr}[e^{-\beta\hat{H}}] = \text{tr}[(e^{-\frac{\beta}{N}\hat{H}})^N] = \text{tr}[(e^{-\beta_N\hat{H}})^N] \quad (2.124)$$

To insert N-1 complete sets of position Eigenstates,

$$Q(\beta) = \int_{-\infty}^{+\infty} dx_1 \dots \int_{-\infty}^{+\infty} dx_N \langle x_1 | e^{-\beta_N\hat{H}} | x_2 \rangle \dots \langle x_N | e^{-\beta_N\hat{H}} | x_1 \rangle \quad (2.125)$$

and making an approximation for each matrix element using Trotter splittings gives,

$$\langle x_{N-1} | e^{-\beta_N \hat{H}} | x_N \rangle \approx \langle x_{N-1} | e^{-\beta_N \frac{\hat{V}}{2}} e^{-\beta_N \hat{T}} e^{-\beta_N \frac{\hat{V}}{2}} + O(\beta_N^3) | x_N \rangle \quad (2.126)$$

in which now an error only of order β_N^3 in each case is introduced, and the method in the limit $N \rightarrow \infty$ becomes exact. Evaluating each density matrix gives,

$$\langle x_{N-1} | e^{-\beta_N \hat{H}} | x_N \rangle \approx \left(\frac{1}{2\pi\beta_N} \right)^{\frac{1}{2}} e^{-\beta_N \left[V(x_N) + \frac{1}{2(\beta_N \hbar)^2} \sum_{i=1}^N (x_{i+1} - x_i)^2 \right]} \quad (2.127)$$

putting all together, the partition function can be written,

$$Q(\beta) = \lim_{N \rightarrow \infty} \left(\frac{1}{2\pi\beta_N \hbar^2} \right)^{N/2} \int \mathbf{d}\mathbf{x} e^{-\beta_N U_N(\beta, \mathbf{x})} \quad (2.128)$$

where $\mathbf{x} = (x_1, \dots, x_N)$ and $U_N(\beta, \mathbf{x})$ is,

$$U_N(\beta, \mathbf{x}) = \left[\sum_{i=1}^N V(x_i) + \frac{1}{2(\beta_N \hbar)^2} \sum_{i=1}^N (x_{i+1} - x_i)^2 \right]_{x_{N+1}=x_1} \quad (2.129)$$

In the above equation, the mass-scaled coordinates are employed, such that $x = \sqrt{m} \times \text{position}$, where m is the physical mass of the particle. The obtained $Q(\beta)$ is equivalent to a classical partition function for an extended system, in which the particle is replaced by a set of N replica or "beads" connected into a ring, known as "ring polymer". The frequency of harmonic springs are equal to $1/\beta_N \hbar$, which imply that the stiffness of the springs is temperature dependent. The integrals in Eq. (2.128) is then approximated using the method of steepest descent.

2.3.2 STEEPEST DESCENT APPROXIMATION

The steepest descent approximation is based on the principle that a function of the form $e^{-S(x)/\hbar}$ is dominated by the region in which $S(x)$ is minimal. In one dimension, the method of steepest descent is expressed as,

$$\int_{-\infty}^{\infty} dx e^{-S(x)/\hbar} \approx \int_{-\infty}^{\infty} dx e^{-[S(\tilde{x}) + \frac{1}{2} S''(\tilde{x})(x-\tilde{x})^2]/\hbar} \approx \sum_{\text{minima}} \sqrt{\frac{2\pi\hbar}{S''(\tilde{x})}} e^{-S(\tilde{x})/\hbar} \quad (2.130)$$

where the sum is over the minima in $S(x)$, \tilde{x} is the minimum of $S(x)$, and $S''(\tilde{x})$ is the second derivative of $S(x)$ with respect to x . The steepest descent is considered as a semi-classical approximation which in the limit $\hbar \rightarrow 0$ becomes exact. For the application of steepest descent to the integral in Eq. (2.128), the position of the minima \tilde{x} is identified by solving $\partial U_N(\beta, \mathbf{x})/\partial x_i$. Expanding $U_N(\beta, \mathbf{x})$ to the second order Taylor series about each minima gives,

$$U_N(\beta, \mathbf{x}) \approx U_N(\beta, \tilde{x}) + \frac{1}{2} \sum_{i=1}^N \sum_{j=1}^N (x_i - \tilde{x}_i) G_{ij} (x_j - \tilde{x}_j) \quad (2.131)$$

where G_{ij} are the elements of the Hessian matrix,

$$G_{ij} = \frac{2\delta_{ij} - \delta_{ij-1} - \delta_{ij+1}}{(\beta_N \hbar)^2} + V''(\tilde{x}_i) \delta_{ij} \quad (2.132)$$

with cyclic boundary conditions on the Kronecker δ -function. A transformation to normal mode coordinates can be obtained by diagonalisation of the Hessian matrix, \mathbf{G} , which yields \mathbf{s} and η_i as the normal mode coordinates and frequencies, respectively. Evaluating the integrals in Eq. (2.128) by transforming from the coordinates \mathbf{x} to normal coordinates \mathbf{s} , and applying this procedure to all the minima, the partition function is obtained as

$$Q(\beta) \approx \tilde{Q}(\beta) = \left(\frac{1}{\beta_N \hbar} \right)^N \sum_{\text{minima}} \frac{1}{\sqrt{\det \mathbf{G}}} e^{-\beta_N U_N(\beta, \tilde{\mathbf{x}})} \quad (2.133)$$

where “ $\det \mathbf{G}$ ” is determinant of \mathbf{G} equal to $\prod_{i=1}^N \eta_i^2$. The partition function of tunneling and non-tunneling systems are then evaluated from Eq. (2.133).

In the following part, the relation between imaginary-time path-integral representation of the Boltzmann operator and U_N as the ring-polymer potential is described, which is the foundation of the ring-polymer instanton method.

Periodic orbits, kinks, and zero frequency modes

Path integral approach of Feynman^{9,10} is an alternative but equivalent methodology to the usual wave-function description of quantum mechanics, in which the propagator is expressed as the sum over all possible trajectories $x(t)$ of a particle moving through a time-independent potential $V(x)$ between two spacetime points (x_i, t_i) and (x_f, t_f) . Feynman posits that the contribution to the propagator from each trajectory is $\exp[\mathbf{i}S[x(t)]/\hbar]$,

$$\langle x_f | e^{-\mathbf{i}\frac{\hat{H}t}{\hbar}} | x_i \rangle = N \int Dx(t) e^{\frac{\mathbf{i}S[x(t)]}{\hbar}} \quad (2.134)$$

with $S[x(t)] = \int dt [T - V]$

where $S[x(t)]$ is the action integral. A comparison between the quantum Boltzmann operator $\exp(-\beta \hat{H})$ and quantum time evolution operator $\exp(-\mathbf{i}\hat{H}t/\hbar)$, gives,

$$t = -\mathbf{i}\beta \hbar \quad (2.135)$$

which implies $\tau = \beta \hbar$ has units of “imaginary time” and the propagator of a system with respect to imaginary time $\tau = \mathbf{i}t$ resembles the partition function. Using $\tau = \beta \hbar$, and $\tau_N = \tau/N$,

$$\tau_N = \beta_N \hbar \quad (2.136)$$

Using Eq. (2.129), $\tau_N U_N$ in imaginary time formalism can be written as,

$$\tau_N U_N = \sum_{i=1}^N \tau_N \left[V(x_i) + \frac{1}{2\tau_N^2} (x_{i+1} - x_i)^2 \right] \quad (2.137)$$

which is the discretized version of,

$$\int_0^\tau d\tau' \left[V(x(\tau')) + \frac{1}{2} \left(\frac{dx(\tau')}{d\tau'} \right)^2 \right] \quad (2.138)$$

that is the action integral,

$$S = \int_0^\tau d\tau' [T - \tilde{V}] \quad (2.139)$$

in a discretized form of N time slices of width τ_N , for a periodic motion in $\tilde{V}(x) = -V(x)$. with $x(0) = x(\tau)$ such that $x_{j+1} = x(j\cdot\hbar\beta_N)$. Therefore, the action integral and the ring-polymer potential are related to each other through,

$$S_N = \tau_N U_N = \sum_{i=1}^N \tau_N \left[V(x_i) + \frac{1}{2\tau_N^2} (x_{i+1} - x_i)^2 \right] \quad (2.140)$$

which means the discretized version of path integral is equivalent to a classical partition function of many replicas of the system connected together by harmonic springs. In fact, $\tau_N U_N$ is a finite difference approximation to the action of a periodic classical trajectory in the inverted potential. As it can be seen, the complex oscillatory integrand of the standard path integral becomes a positive real decaying exponential in imaginary time formulation, which is far easier to work with. The relation between the action of periodic motions in the inverted potential and the ring-polymer potential, Eq. (2.140) also implies that the sequence of beads at each minimum geometry $\tilde{\mathbf{x}}$ of U_N are minimizing the action of periodic orbit on the inverted potential $-V(x)$, with period $\beta\hbar$.

The inverted potential $-V(x)$ in a one-dimensional double well potential consists of a pair of inverted wells centered around $\pm x_0$. For the non-tunneling case that two wells are not interacting via tunneling, the only possible orbits are those where particle remains at $\pm x_0$ for the entire duration $\tau = \beta\hbar$ of the trajectory. This corresponds to a polymer, in which all the beads are collapsed at either minima. For the tunneling case, there is an infinite set of orbits in which the particle passes back and forth between $\pm x_0$. In the limit $\beta \rightarrow \infty$, the classical trajectory can run infinite number of times, n , between two equivalent potential minima, which is referred as “ n -kinks”. Most of beads, however, are tending to rest for an arbitrary length of imaginary time at one of the minima before moving to the other minima, means that the kinks are contributed from only very few beads.

For evaluating tunnel splittings, all the contributions from even number of kinks (the number of kinks is even because of the closed ring nature of orbits) need to take into account as each kink increases the value of the exponent $\beta_N U_N(\beta, \tilde{\mathbf{x}})$. The description of such orbits by ring polymers is known to be a difficult problem. However, according to the instanton theory,²¹ the tunnel splitting can be obtained from a single kink. Therefore, it is only sufficient to consider a linear polymer containing a single kink, *i.e.*, the classical paths connecting equilibrium states, which minimize an imaginary time action of the system. Hence, as the stationary beads do not contribute to the ring-polymer potential, Eq. (2.131), and the non-zero contributions come from the beads in the kinks, U_N factors into kinks,

$$U_N(\beta, \tilde{\mathbf{x}}) = \frac{n S_{kink}}{\beta_N \hbar} \quad (2.141)$$

where S_{kink} is the finite difference approximation to the action along a kink, defined as,

$$S_{kink} = \sum_{i \in kink} \frac{(\tilde{x}_{i+1} - \tilde{x}_i)^2}{\beta_N \hbar} \quad (2.142)$$

The linear polymer containing M beads with a length $\beta \hbar$ is defined such that the beads are separated by the same imaginary time intervals as in the ring polymers, $\beta \hbar / M = \beta_N \hbar$. If the ends of the linear polymer are connected to the minima $\pm x_0$, it results in the fixed ended linear polymer subject to the potential defined as

$$U_M(\beta, x) = \sum_{i=1}^M V(x_i) + \frac{1}{2(\beta_M \hbar)^2} \times \left[(x_1 + x_0)^2 + \sum_{i=1}^{M-1} (x_{i+1} - x_i)^2 + (x_0 - x_M)^2 \right] \quad (2.143)$$

where M is the number of beads. By minimizing the linear polymer potential, the minimum geometry $\tilde{\mathbf{x}}$ can be obtained. The action of a single kink is obtained by finding a single kink minimum on the M bead linear polymer surface just described in Eq. (2.138).

In the evaluation of partition function of non-tunneling system, zero frequencies mode need to be excluded, which appear due to the cyclic permutation of the beads. For instance, the 2-kink ring polymer minimum had one imaginary and one zero frequency mode. As the temperature is lowered, the imaginary mode reduces in magnitude until it goes to zero at absolute zero temperature. In general, each n -kink minimum possesses n modes of very small value, tending to zero in the limit of $\beta \rightarrow \infty$. Instead, their contributions to the quantum partition function need to be

treated separately. The result is that each of the zero-frequency modes contributes a factor of $\sqrt{\beta_N \hbar S_{kink}}$ to the path integral, where S_{kink} is the action integral of a single kink.^{16, 17, 20, 111}

2.3.3 EXPRESSION FOR THE TUNNELING SPLITTING

Putting all this together and evaluating the quantum partition of the tunneling and non-tunneling systems, the final expression for tunneling splitting is obtained as,

$$\Delta = \lim_{\beta \rightarrow \infty} \frac{2\hbar}{\Phi} \sqrt{\frac{S_{kink}}{2\pi\hbar}} e^{-S_{kink}/\hbar} \quad (2.144)$$

where single kink action and Φ are defined as,

$$\Phi = \left(\frac{\det \mathbf{J}'}{\det \mathbf{J}_0} \right)^{(1/2)} \quad (2.145)$$

$$S_{kink} = \beta_N \hbar U_M(\beta, \tilde{\mathbf{x}})$$

and the matrix \mathbf{J} is the Hessian matrix for the single-kink linear polymer,

$$J_{ij} = \frac{T_{ij}}{(\beta_N \hbar)^2} + V''(\tilde{x}_i) \delta_{ij} \quad (2.146)$$

where

$$\begin{aligned} T_{ij} &= 2\delta_{ij} - \delta_{ij-1} \quad \text{for } i = 1 \\ &= 2\delta_{ij} - \delta_{ij+1} \quad \text{for } i = M \\ &= 2\delta_{ij} - \delta_{ij-1} - \delta_{ij+1} \quad \text{otherwise} \end{aligned} \quad (2.147)$$

The Hessian matrix \mathbf{J}' in Eq. (2.145) corresponds to a linear polymer that the zero frequencies have been taken out of the determinant. The Hessian matrix \mathbf{J}_0 corresponds to a linear polymer with the same number of beads M and time interval $\beta_N \hbar$ as the single kink polymer, but which has collapsed to a point at either $\pm x_0$.

The method is applied to the one-dimensional double well potential and the one-dimensional three-fold cosine potential for the estimation of tunneling splittings (see Appendix E).

CHAPTER 3

METHYL GROUP ROTATION AND TUNNELING IN CONDENSED PHASE

In this chapter, tunneling and librational dynamics of the methyl groups within a model of rotational potential will be discussed. A general approach is introduced for the calculation of the methyl rotor quantum states in actual crystal structures. The specific focus is on γ -picoline and toluene, which are chemically very similar, however, by contrast γ -picoline obtains a larger tunnel splitting than toluene. The rotational potential energy surfaces of the methyl groups are computed using a set of first principle calculations combined with the nudged elastic method. The tunnel splitting is calculated by an explicit diagonalization of the one-dimensional time-independent Hamiltonian matrix with the obtained potential energy profile.

3.1 METHYL GROUP DYNAMICS WITHIN A PARAMETER MODEL POTENTIAL

A methyl rotor in a molecular crystal performs hindered rotation around the carbon-molecule bond axis. The resultant rotational potential has a typical three-fold symmetry because of the indistinguishability of the protons. At low temperatures, the motion of the methyl group is reduced to a libration around the identical minima of the rotational potential. As the wave-like characteristics of the methyl group gives rise to quantum tunneling through connected potential minima, the three-fold degenerate ground state of methyl groups, E_0 , splits into double degenerate levels $E_{a/b}$ and a non-degenerate ground state A , where the symmetry labels refer to the irreducible representation of the methyl rotor with $C_3(M)$ molecular symmetry.¹¹² Applying Pauli principle to this group imposes that the spatial A state must be associated with the nuclear triplet spin state $3/2$. Accordingly, the spatial E_a and E_b states must be associated with the nuclear singlet spin state $1/2$, respectively. The correlation between spin and rotational quantum states has important consequences for tunneling spectroscopy because a change in rotational state requires a change in spin state.

The tunneling dynamics of hydrogen atoms in methyl rotors can be modeled in terms of a methyl group rotating around its C-C bond axis in a rigid environment. A single rotational coordinate ϕ describes the orientation of protons for single methyl rotation.²⁴ The one-dimensional Hamiltonian is defined as,

$$H = -\frac{\hbar^2}{2I} \frac{\partial^2}{\partial \phi^2} + V(\phi) \quad (3.1)$$

where I , ϕ , and $V(\phi)$ stand for the moment of inertia of the methyl group, the rotation angle, and rotational potential, respectively. The motion of the methyl group can be approximately described in terms of a potential $V(\phi)$ composed of an intramolecular term and intermolecular van der Waals and Coulomb terms. An overall contribution of these terms can often result in a simplification where the threefold symmetry of the methyl group constrains the symmetry of the total intermolecular potential to be at least threefold.¹¹³ Therefore, the rotational potential can be written as a Fourier series in which only those terms whose order is a multiple of three occur due to the three fold symmetry of the methyl group,

$$V(\phi) = \sum_{i=1}^{\infty} \frac{V_{3i}}{2} [1 - \cos(3i\phi + \alpha)] \quad (3.2)$$

This series is usually truncated after the second term without loss of generality, yielding,

$$V(\phi) = \frac{V_3}{2} [1 - \cos(3\phi + \alpha)] + \frac{V_6}{2} [1 - \cos(6\phi + \alpha)] \quad (3.3)$$

where α is the phase angle. In Appendix A, the ground state tunnel splitting and librational energies of methyl group in such potential of general shape are given. Here, the discussion is restricted to the contribution of the three fold potential with $\alpha = 0$. Accordingly, the following Hamiltonian is considered,

$$H = -\frac{\hbar^2}{2I} \frac{\partial^2}{\partial \phi^2} + \frac{V_3}{2} (1 - \cos 3\phi) \quad (3.4)$$

which is solved numerically using matrix representation of Numerov method.¹¹⁴ The dependence of eigenvalues of the methyl group on the barrier height over a broad range of V_3 is shown in Fig. 3.1. In the following, three limits of high, intermediate, and low strength of V_3 for the methyl motion are discussed.

A. High barrier

In this limit, small deviations from one of the three equilibrium positions results in

nearly harmonic motion with the usual quantized energy levels,

$$E_n = (n_{\text{LIB}} + \frac{1}{2})\hbar\omega_0 \quad (3.5)$$

where ω_0 is the oscillation frequency. An estimation of the oscillation frequency of the motion at the lowest energy state can be obtained in the harmonic approximation via Taylor series expansion about $\phi = 0$ for the cosine potential term,

$$V(\phi) = \frac{V_3}{2}(1 - \cos 3\phi) \approx \frac{V_3}{2}(1 - 1 + \frac{(3\phi)^2}{2!} + \dots) = \frac{1}{2} \frac{9V_3}{2} \phi^2 \quad (3.6)$$

A comparison between the above potential and harmonic potential gives,

$$\omega_0 = 3\sqrt{\frac{V_3}{2I}} \quad (3.7)$$

Thus, the librational transitions, the energy difference between the librational levels, are approximately constant, given by

$$\Delta E_n = E_n - E_{n-1} = \hbar\omega_0 = 3\hbar\sqrt{\frac{V_3}{2I}} \quad (3.8)$$

B. Intermediate barrier

In the intermediate regime, the rotational dynamics can be simplified to the energy-level diagram shown in Fig. 3.2, in which the lowest two librational levels, n_{LIB} , and their tunnel split sub levels are shown. The transition from the ground state to the first excited librational state, denoted by $\hbar\omega_{01}$ can differ from the ground state tunnel splitting $\hbar\omega_{\text{tunnel}}^0$ by several orders of magnitude, which is an important practical point in the measurements of rotational tunneling. This means that at low temperature where the thermal population of the excited librational states is negligible, the system can be approximated by a two-state model.¹¹³

C. Low barrier

In this limit, the energy levels are approximately the free rotation levels, $E_n = Bn^2$, where B is the rotational constant. The librational transitions are given by

$$\Delta E_n = E_n - E_{n-1} = (2n - 1)B \quad \text{for } n = 1, 2, 3, \dots \quad (3.9)$$

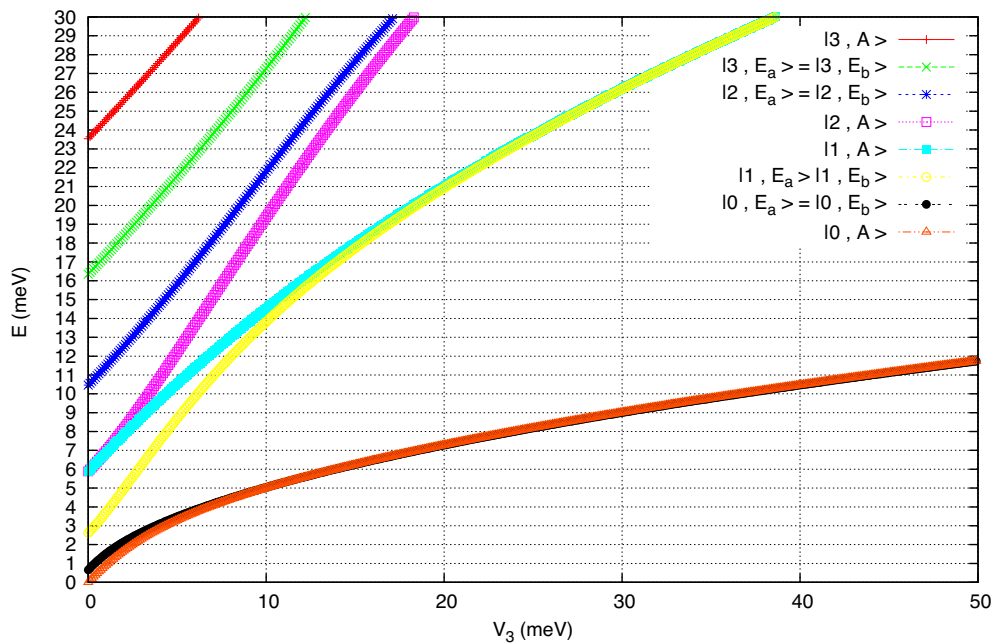


Figure 3.1: Eigenvalues for a methyl group as a function of the barrier height, V_3 .

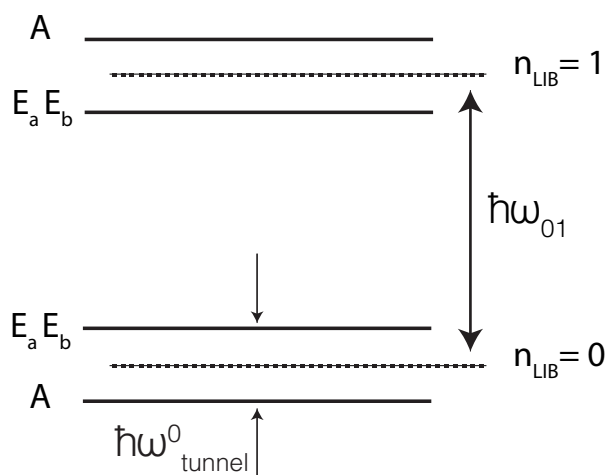


Figure 3.2: Schematic illustration of the first two lowest librational levels and tunnel split. The symmetries of the eigenstates are denoted by labels A , E_a and E_b .

3.1.1 TUNNEL SPLITTING

The tunnel splitting, $\hbar\omega_{\text{tunnel}}^0$, also called tunneling transition, is the energy difference between the ground spatial A state and the first excited rotational state with symmetry E_a and E_b .⁴ Fig. 3.3 shows the dependence of tunnel splitting to the barrier height, in which the exponential dependence of the tunnel energy on the barrier height, V_3 , can be clearly seen. The frequency corresponding to the tunneling energy decreases as the barrier increases due to the fact that for larger barriers, the wave functions tend to overlap less. This is the origin of the practical sensitivity of the tunneling in the context of characterizing the potential energy surfaces. Fig. 3.4 shows the barrier height dependence of the first librational transition calculated from the numerical diagonalization of the Hamiltonian, Eq. (3.4), and the harmonic approximation. The first librational transition is simply the difference between the average of the lowest two and the following two eigenvalues in the limit of high barriers (see Fig. 3.2). Fig. 3.4 clearly shows that when $V_3/B \gg 1$, the slopes of the curves agree, but the harmonic approximation systematically overestimates the actual value. In fact the agreement improves with increasing barrier height but the convergence is quite slow.

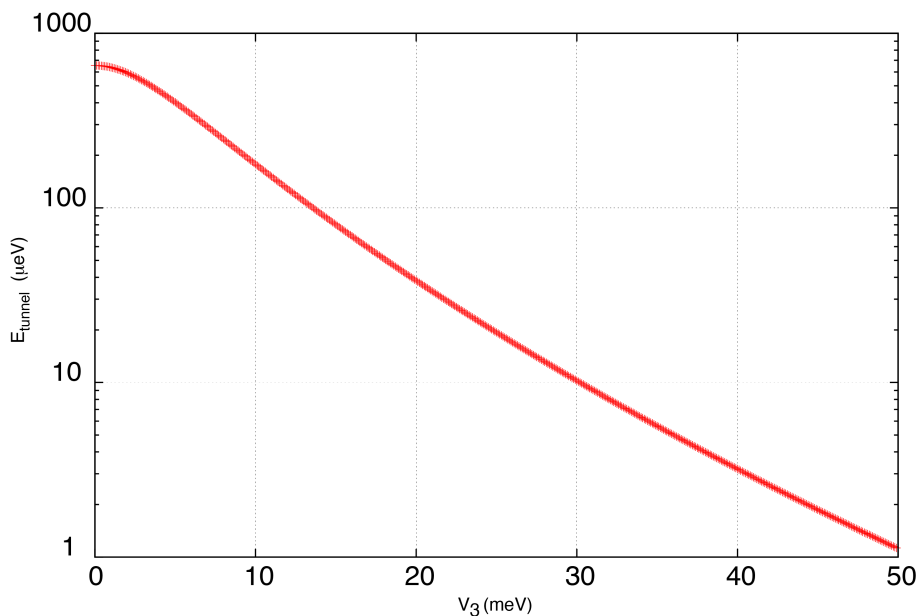


Figure 3.3: Tunnel splitting of the ground librational state. The approximate exponential dependence of the tunnel splitting on the barrier height is clearly seen.

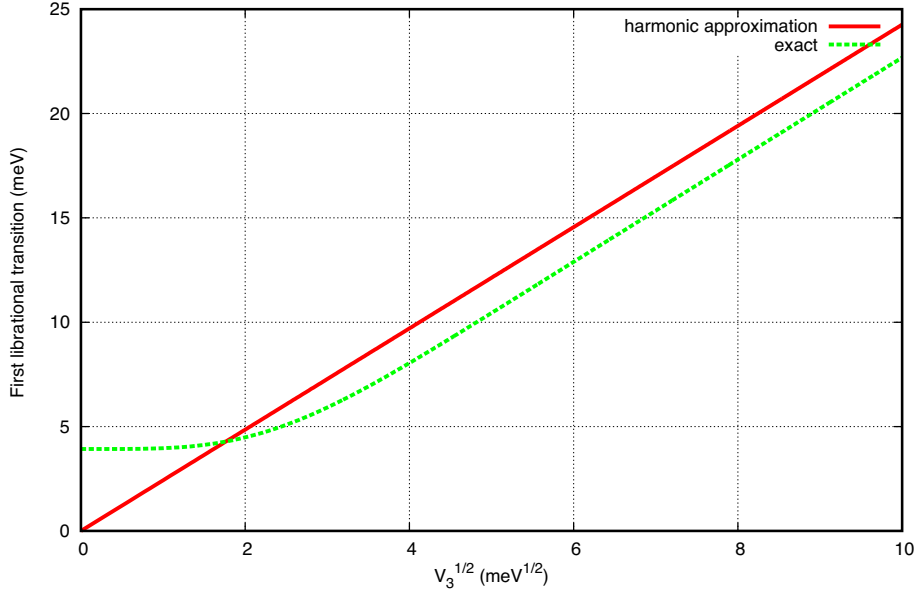


Figure 3.4: Barrier height dependence of the first librational transition (dashed line). The solid line is the harmonic approximation, $E = \hbar\omega_0$.

3.2 ROTATIONAL TUNNELING IN γ -PICOLINE AND TOLUENE

Turning from the discussion of the abstract model Hamiltonian to the actual crystal structures; the methyl dynamics in crystal structures is defined by the one-dimensional Hamiltonian, Eq. (3.1). In order to obtain the rotational potential form $V(\phi)$ accurately, the first-principles calculations are employed. The tunnel splittings are calculated numerically by diagonalization of the Hamiltonian using matrix representation of Numerov method.¹¹⁴

The initial geometrical structures were extracted from the reported experimental data obtained by neutron scattering technique.^{115,116} In this regard, γ -picoline possesses space group of $I4_1/a$ with eight molecules per unit cell with $a = b = 7.62$ and $c = 18.62$ Å lattice parameters. The crystalline structure of toluene is monoclinic with space group $P2_1/c$ and eight molecules per unit cell with $a = 7.66$, $b = 5.83$ and $c = 26.98$ Å lattice parameters and $\beta = 105.73^\circ$. In order to avoid the interaction between the probe rotor molecule with its neighboring periodic images, a super cell of $2 \times 2 \times 1$ was used in obtaining the minimum energy paths for the molecular crystals of γ -picoline and toluene.

The first-principles calculations were performed within the context of density functional theory (DFT) using the generalized gradient approximation with the

Becke-Lee-Yang-Parr (BLYP) exchange correlation functional^{48,51} and Gaussian Plane Wave (GPW) method. The plane wave cutoff energy was set to 400 Ry. A gaussian basis sets of triple zeta with valence polarization(TZVP) together with GTH pseudopotentials was employed. The positions of atoms were fully optimized using Broyden-Fletcher-Goldfarb-Shanno (BFGS) method. After optimization, the maximum force acting on each atom became less than 0.00035 hartree/bohr. Dispersion effects were included via semiempirical atom pairwise interactions using the DFT-D3 method developed by Grimme *et al.*^{53,67,68} After structural optimization, the minimum energy path experienced by methyl group in molecular crystal was computed as a function of the rotation angle, ϕ , by performing DFT calculations combined with climbing image nudged elastic band (CI-NEB) method.²⁸ In this regard, all degrees of freedom of the environment as well as the probe methyl group were allowed to relax under periodic boundary condition. For the CI-NEB calculations, a band with 24 replicas of the molecular crystal was set by rotating a single methyl group by 5° over 120° . All the calculations were done using CP2K code.⁹⁵ The binding energies per molecules are computed as $E_{binding} = (E_{crystal} - n \times E_{molecule})/n$, where $E_{crystal}$, $E_{molecule}$, and n stand for the total energy of the crystal, total energy of an isolated molecule, and the number of molecules in the cell, respectively. Figures 3.5(a) and 3.5(b) show the rotational potential of γ -picoline and toluene, respectively. For toluene, two different rotational potential profiles are given because of the presence of two inequivalent molecules in the crystallographic unit cell. Figs 3.6(a) and 3.6(b) present the rotational potential barriers with van der Waals correction. Table 3.1, and 3.2 summarize the computed tunneling frequencies and binding energies for the molecular crystals of γ -picoline and toluene. Experimentally, the magnitude of the rotational potential is only measured indirectly via a potential of general shape¹¹⁷ (see Appendix A). The positive values of binding energy of these systems in the absence of dispersion correction show that including the van der Waals correction is essential to gain a correct description of intermolecular interactions. Regarding the height of the energy barriers, it is seen that irrespective of including or excluding the van der Waals interaction, the rotational barriers of methyl groups is larger in toluene than in γ -picoline. This is due to the packing effect, which will be discussed in the following section. Including the dispersion correction in the calculations leads to rotational potentials, which are about two times larger than the ones obtained from uncorrected calculations. For the γ -picoline system, inclusion of dispersion correction leads to a large deviation of the tunnel splitting from the experimental

value, which is not the case for the toluene system. This is because of neglecting the methyl-methyl rotational coupling in γ -picoline. Hence, in the next sections, the two effects of packing and coupling on the rotational energy barrier are elaborated.

Table 3.1: Experimental and calculated tunnel splittings for γ -picoline and toluene.

Molecular crystal	γ -picoline		toluene			
			First type of methyl group		Second type of methyl group	
Method/Basis set	barrier height	tunnel splitting	barrier height	tunnel splitting	barrier height	tunnel splitting
BLYP/TZVP-GTH	3.53 meV	482.3 μ eV	19.53 meV	27.6 μ eV	13.34 meV	67.0 μ eV
BLYP+DFTD3/TZVP-GTH	7.66 meV	224.0 μ eV	33.28 meV	4.5 μ eV	22.04 meV	17.9 μ eV
Experimental values	<i>n/a</i>	520.0 μ eV ¹¹⁷	<i>n/a</i>	26.0 μ eV ¹¹⁷	<i>n/a</i>	28.5 μ eV ¹¹⁷

Table 3.2: Binding energy of molecules in molecular crystals of γ -picoline and toluene.

Molecular crystal	γ -picoline	toluene	
		First type of methyl group	Second type of methyl group
Method/Basis set	Binding energy	Binding energy	
BLYP/TZVP-GTH	016 eV	0.27 eV	
BLYP+DFTD3/TZVP-GTH	-0.83 eV	-0.72 eV	

3.2.1 PACKING EFFECT

Typically, the effective rotational energy barrier of methyl rotors consists of two contributions: internal (within the rotor) and environmental (non-bonded interactions). It is clearly seen from Figs. 3.5(a) and 3.5(b) that the rotational energy barrier of the methyl group is substantially larger for toluene than that for γ -picoline. This can be attributed to the steric effect. Figures 3.7(a) and 3.7(b) illustrates the local environments around methyl rotors of γ -picoline and toluene, respectively, along with shortest distances to their close neighboring molecules. Based on these contact distances, it appears that the probe methyl group in toluene is more tightly surrounded by the neighboring molecules, and such crowded environment around probe molecule leads to steric hindrance and increases the rotational barriers.¹¹⁸

To reveal how far a probe molecule affects the neighboring molecules, difference charge density analysis is performed. Difference charge density $\Delta\rho$ is obtained by

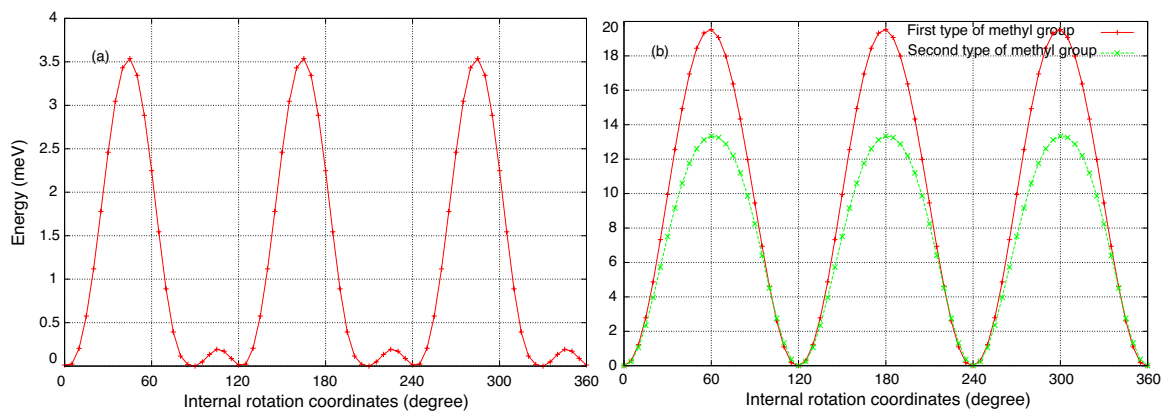


Figure 3.5: The methyl group rotational potential for a) γ -picoline and b) toluene obtained from first-principles calculations.

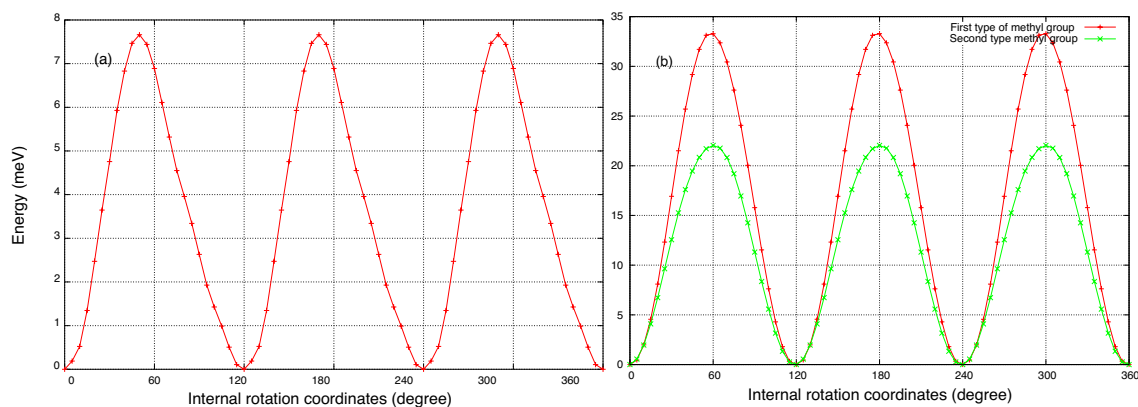


Figure 3.6: The methyl group rotational potential for a) γ -picoline and b) toluene obtained from first-principles calculations when the dispersion correction was included.

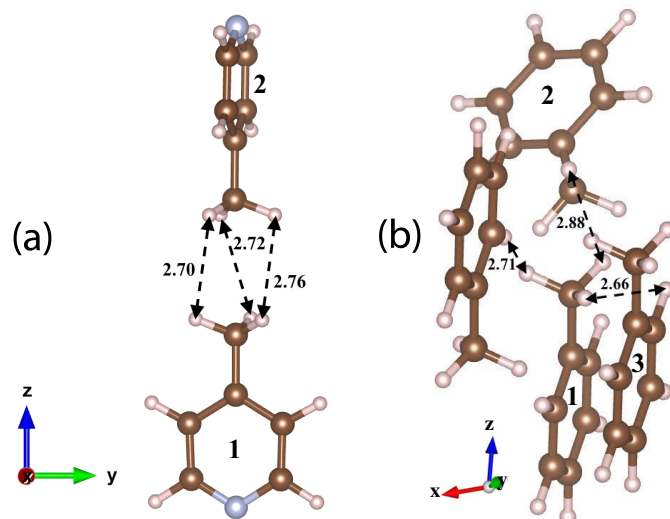


Figure 3.7: The ground state geometrical arrangements of the nearest molecule(s) to the probe molecule in a) γ -picoline and b) toluene (for first type methyl group). The probe molecule is labeled 1 and the nearest molecules to the probe molecule are labeled 2 and 3. The distances are in Å.

subtracting the charge density of the probe molecule and the crystal in the absence of the probe molecule from the total charge density of the crystal. Figures 3.8(a) and 3.8(b) show difference charge density isosurfaces for γ -picoline and toluene, respectively. The results for the difference charge density obtained from DFT-D3 calculations are the same. It is clearly seen that upon removing the probe molecule from the system, the charge redistribution occurs mainly within its first shell of neighboring molecules of the probe molecule. Therefore, in order to discuss the contributions of the neighboring molecules in the rotational potential of the crystal, the focus will be mainly on the molecules surrounding the probe molecule.

The potential decomposition analysis of rotational potential is processed as follows: the super cell of both γ -picoline and toluene crystals include 32 molecules. Thereby, as it is pointed out in the previous paragraph, there merely needs to consider the contribution of surrounding molecules around the γ -picoline probe rotor (16 molecules) and toluene probe rotor (13 molecules) in total rotational potentials as shown in Figs. 3.9 and 3.10, respectively. Here, the geometrical structure with minimum energy, which were obtained from the NEB calculations, is used. The intermolecular interactions between the probe methyl group and each set of labeled neighboring molecules in Figs. 3.9 and 3.10 for γ -picoline and toluene are plotted separately in Figs. 3.11(a) and 3.12(a), respectively. It is clearly seen in

Figs. 3.11(b) and 3.12(b) that the superposition of the potential contributions of sets of nearest neighboring molecules to the probe molecule reproduces the potential barrier of the crystal structure. It is verified that intermolecular interaction potential of nearest neighboring molecules to the probe molecule is virtually equal to the corresponding potential in the full periodic crystal structure. This is another evidence that the shell of nearest neighbor molecules has the main influence on the probe molecule, and consequently has the main contribution in the total rotational barrier.

The steric interaction between the in plane hydrogen of the peri-methyl group and the peri-hydrogen on the benzene ring arises during the methyl rotation leads to intramolecular interaction. The interaction between the probe molecule and the neighboring molecules leads to intermolecular interaction. From the decomposed potential analysis, it is seen that the intermolecular interactions have a larger influence on the potential barrier than the intramolecular interactions.

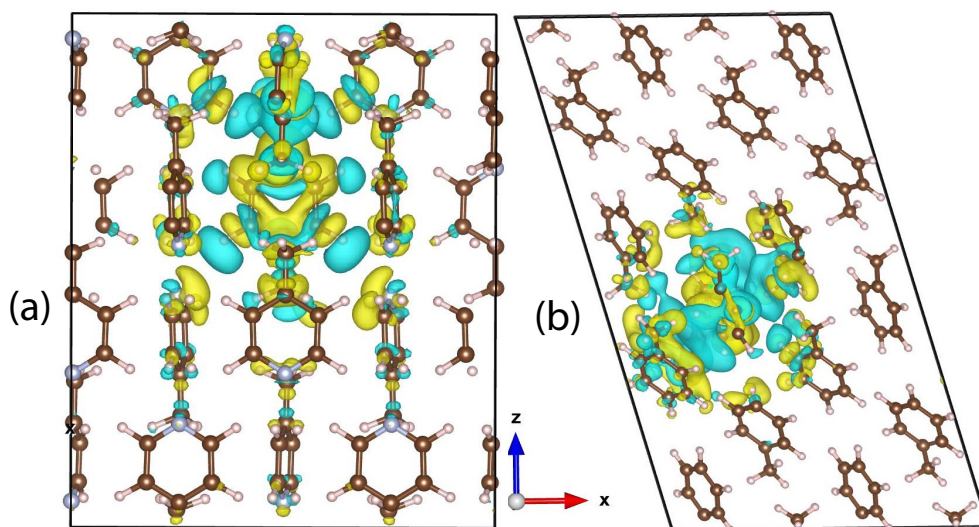


Figure 3.8: Charge density differences for crystal structures of a) γ -picoline and b) toluene (for first type methyl group). Excess and depletion charges are shown by yellow and blue isosurfaces, respectively.

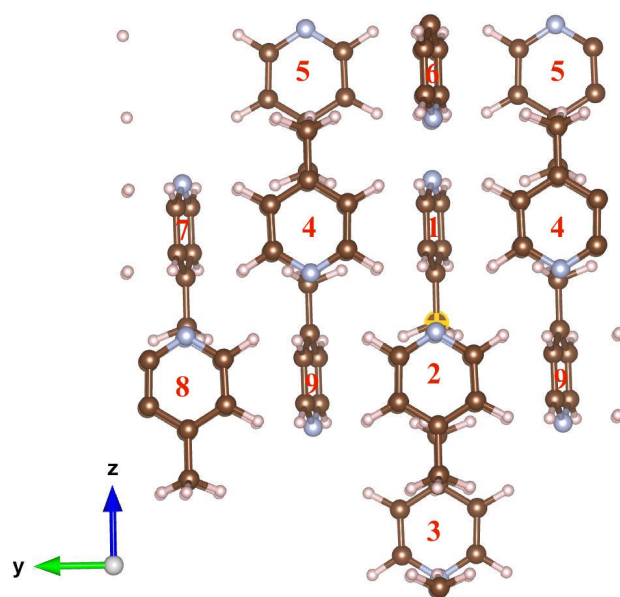


Figure 3.9: Geometrical arrangements of the molecules (labeled 2-9) around the probe molecule (labeled 1) in γ -picoline.

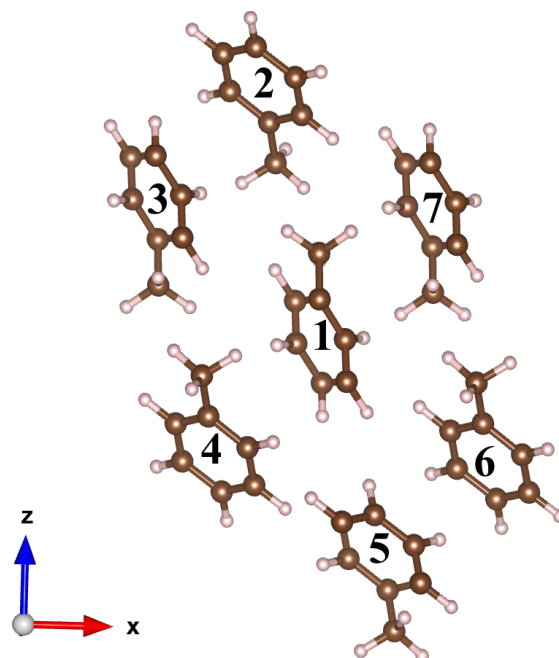


Figure 3.10: Geometrical arrangements of the molecules (labeled 2-7) around the probe molecule (labeled 1) in toluene.

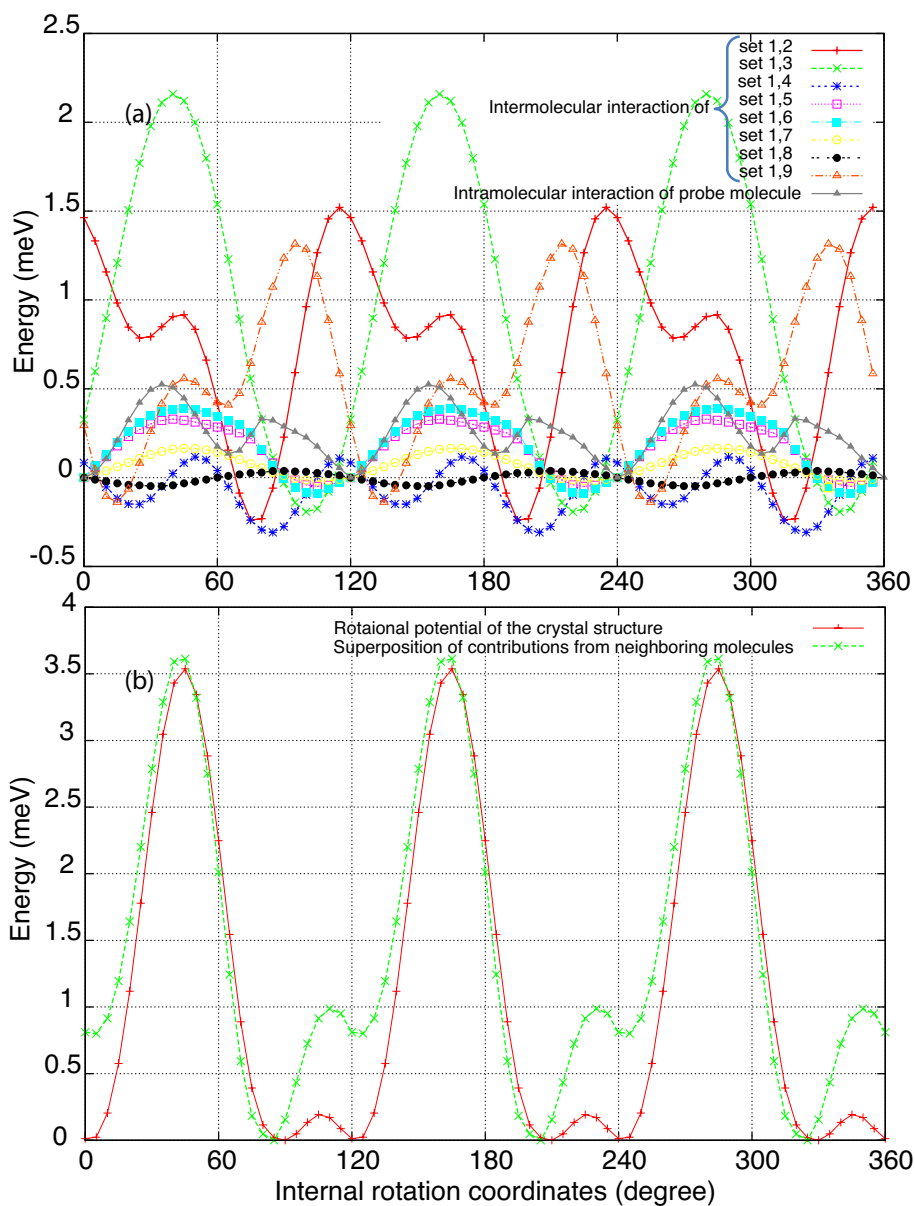


Figure 3.11: a) Decomposition of rotational barrier for γ -picoline into sets of inter- and intra-molecular interactions, and b) comparison of the total rotational barrier of the probe molecule in the crystal with superposition of the decomposed potentials. Numbers 1-9 in panel (a) indicate the labels of molecules in Figure 3.9.

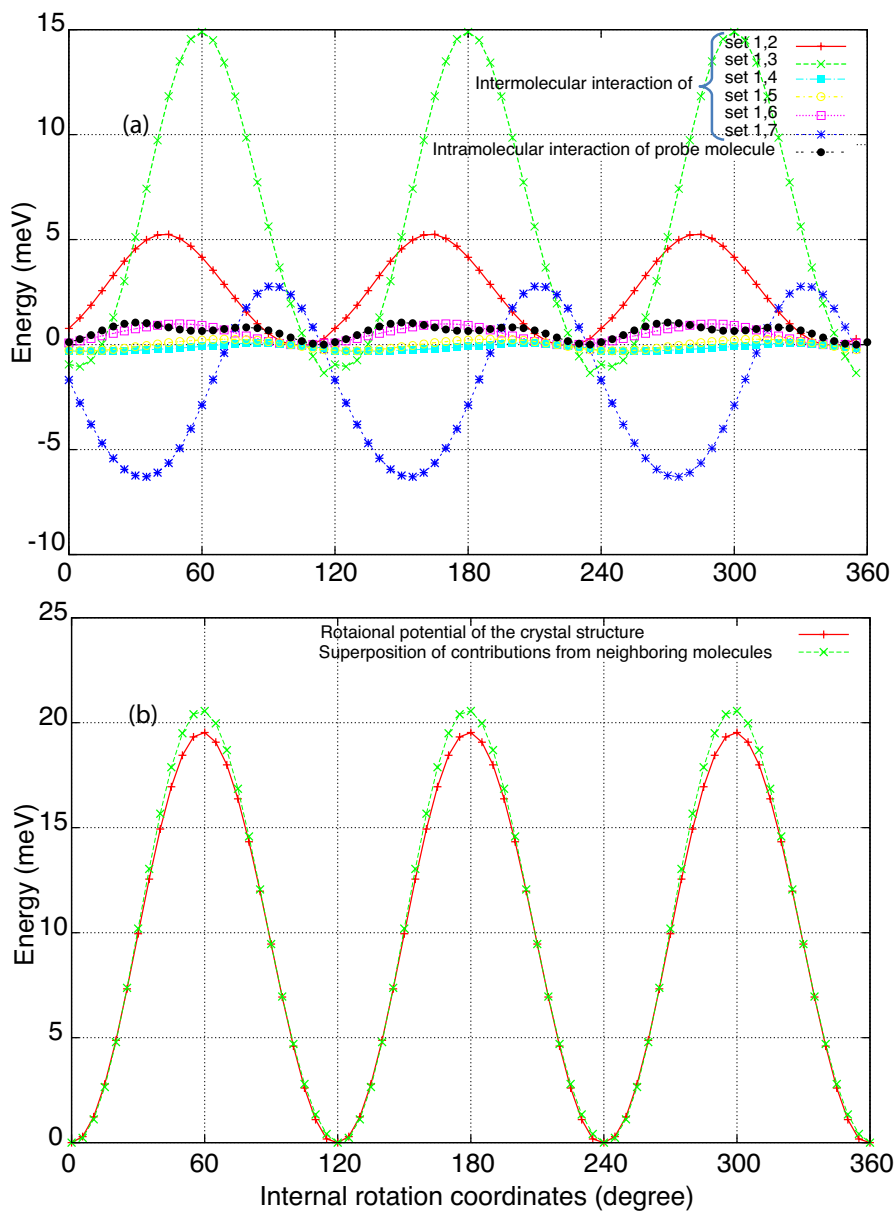


Figure 3.12: a) Decomposition of rotational barrier for toluene into sets of inter- and intra-molecular interactions, and b) comparison of the total rotational barrier of the probe molecule in the crystal with superposition of the decomposed potentials. Numbers 1-7 in panel (a) indicate the labels of molecules in Figure 3.10.

3.2.2 COUPLING EFFECT

Generally, methyl groups perform a wide amplitude librational motion even at low temperatures. Therefore, a coupled rotational motion can be particularly important when the methyl groups locate close to each other. Hence, the effect of coupled motion of the methyl groups should be taken into account in obtaining the rotational energy barrier.^{22–25,119} In this regard, according to relatively close arrangements of methyl groups in crystal structure of γ -picoline and toluene, the possibility of methyl-methyl coupling in these systems are evaluated.

Respecting the molecular environment in γ -picoline, the dominant rotor-rotor coupling is between coaxial pairs of methyl groups, *i.e.*, coupling between the probe molecule and the coaxial methyl rotor facing to it. In toluene, two sets of couplings between the probe toluene molecule and the nearest neighboring molecules as labeled with numbers 2 and 3 in Fig 3.7(b) are considered. In order to compute the two-dimensional potential energy surface (2D PES) of coupled methyl groups, the geometrical structure of the molecular dimer is taken from the last step of the CI-NEB band optimization of the molecular crystal, in which the rotational potential of the crystal was derived. All coupling calculations are carried out using the same method and level of theory as described for the crystal structure.

Figure 3.13 shows the calculated 2D PES of the coupled rotors in γ -picoline and toluene. The computed 2D rotational potentials are obtained at 5 degree rotations of each methyl groups. Due to C_3 rotational symmetry, only data points in the range from 0° to 120° are needed to obtain the 2D PES. In Fig. 3.13, the rotation angles ϕ_1 and ϕ_2 refer to the rotational angles of the probe rotor and its counterpart rotor, respectively. From the 2D PES of γ -picoline in Fig. 3.13(a), it is seen that due to the rotor-rotor coupling between two facing γ -picoline, rotational barrier is effectively reduced along line $\phi_1 + \phi_2 = 120^\circ$, offering a path with low barrier height. In the case of toluene, as it is observed in Fig. 3.13(b) and 3.13(c) no particular path with significant low barrier was observed. Similar results were obtained for 2D rotational potentials when the van der Waals interactions were included (see Fig. 3.14).

In the previous paragraphs is discussed that the dynamics of the coaxial pairs of methyl groups in γ -picoline are strongly coupled. It is also demonstrated that the computed rotational potential energy of probe molecules in crystal could be mainly decomposed into the contributions of its neighboring molecules. This, consequently,

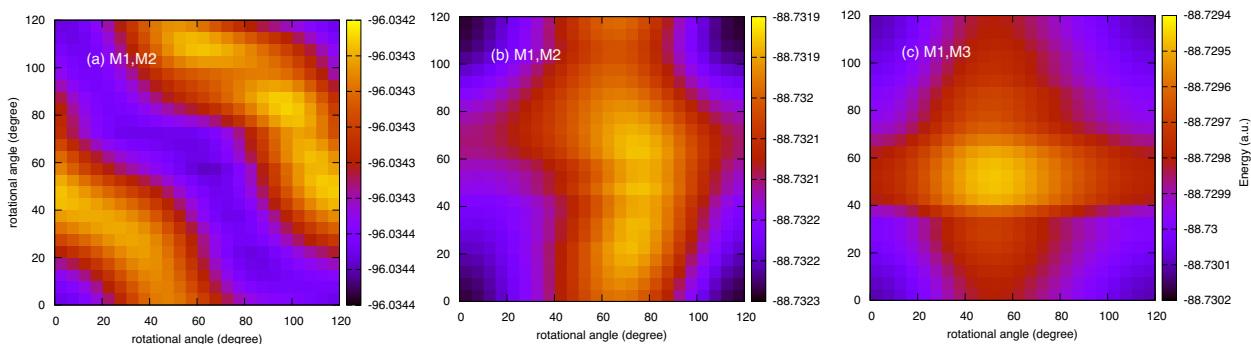


Figure 3.13: Calculated 2D potential energy surfaces for rotor-rotor couplings in (a) γ -picoline, (b) and (c) for toluene. X and Y axes indicate the rotational angles of the rotors. The M1, M2, and M3 represent the molecules, labeled as 1-3, in Figure 3.7 .

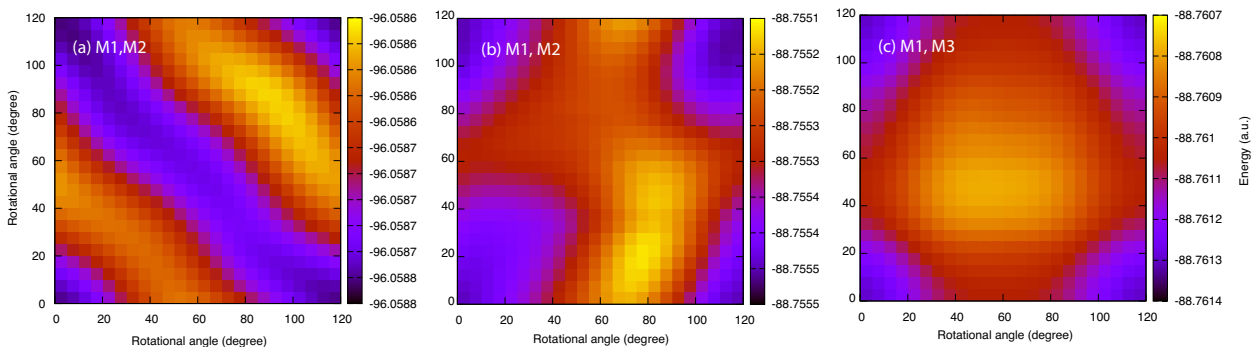


Figure 3.14: Calculated 2D potential energy surfaces of rotor-rotor couplings for (a) a dimer of γ -picoline, (b) and (c) for dimers of toluene when the dispersion correction is included. X and Y axes indicate the rotational angles of the rotors. The M1, M2, and M3 represent the molecules, labeled as 1-3, in Figure 3.7.

allows to include the coupling effect on the tunnel splitting within the scope of the SPM by replacing the rotational barrier of coupled molecules obtained from the NEB calculations with that obtained through considering 2D PES, *i.e.*, the minimum path along the line $\phi_1 + \phi_2 = 120^\circ$.

In order to explicitly find the minimum energy path for the coupled methyl groups in γ -picoline, the obtained 2D PES is fitted to the form:

$$V(\phi_1, \phi_2) = a_0 + a_1[\cos(3\phi_1) + \cos(3\phi_2)] + a_2\cos(3\phi_1 + 3\phi_2) \quad (3.10)$$

where the terms $a_1\cos(3\phi_i)$ ($i=1$ or 2) with three-fold symmetry represent the so-called static potential for each molecule. It is noted that the minimum potential energy surface of an individual γ -picoline has a six fold symmetry, however in the crystal environment, the minimum potential energy surface has three-fold symmetry.^{119,120} Owing to the indistinguishability of the molecules, coefficient parameter a_1 is assumed to be identical for both coupled molecules. The last term in the Eq. (3.10) represents the coupling potential, which depends on the relative rotational angles of two coupled rotors and as the simplest approximation is a three-fold symmetric Fourier component.¹²⁰ Using Gnuplot fitting program, the potential function Eq. (3.10) is fitted to the 2D PES data, where the fitting parameters are given in Table 3.3. Excellent correspondence has been obtained between the original 2D PES data and the fitted data. The result of the fitted 2D PES data is presented in Fig. 3.15.

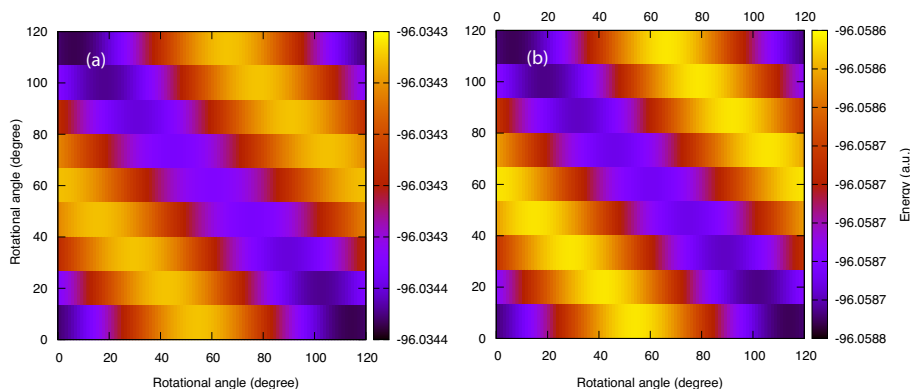


Figure 3.15: The calculated 2D rotational potential through fitting of Eq. (3.10) onto the first-principles rotational potential results for a dimer of γ -picoline molecules (a) without and (b) with considering dispersion correction. X and Y axes indicate the rotational angles of rotors 1 and 2, respectively.

As mentioned earlier, the line $\phi_1 + \phi_2 = 120^\circ$ crossing the 2D-PES represents the

Table 3.3: Fitted parameters of Eq. (3.10) to the 2D potential energy surface of a dimer of γ -picoline molecules.

Method/Basis set	a_0	a_1	a_2
BLYP/GTH-TZVP	-96.0343 (a.u)	-0.177 (meV)	-1.321 (meV)
BLYP+DFTD3/GTH-TZVP	-96.0587 (a.u)	-0.172 (meV)	-1.936 (meV)

Table 3.4: Experimental and calculated tunnel splittings for γ -picoline when the coupling effect is taken into account.

Method/Basis set	Barrier height	Tunnel splitting
BLYP/TZVP-GTH	2.48 meV	623.8 μ eV
BLYP+DFTD3/TZVP-GTH	3.57 meV	475.7 μ eV
Experimental values	n/a	520.0 μ eV ¹¹⁷

rotational pathway for the coupled motion of rotors with minimum energy barrier in γ -picoline. The minimum energy path can be easily obtained via $V(\phi_1, 120^\circ - \phi_1)$ as a function of ϕ_1 , plotted in Fig. 3.16. Figure 3.17 shows the result when dispersion correction is included. According to the calculations, the contribution of the coupling term in Eq. (3.10) along the minimum path is seven times larger than the summation of the static terms ($V_{coupling} > 7 \times V_{static}$). As it is seen from Fig. 3.16, including the coupling effect of the rotors in the calculations yields a rotational barrier, which is more than five times smaller than otherwise. Tunnel splitting values for γ -picoline, including rotor-rotor coupling effects are given in Table 3.4. It is observed that including the coupling effect of the rotors leads to a much better agreement between the calculated tunnel splitting using DFT-D3 energy barrier and the experimental value.

It is worth mentioning that although a single methyl rotation was able to predict the main tunneling transition in γ -picoline, however it fails to predict the multiplet structure of tunneling transitions observed in its experiment. In the next chapter, the multiple tunneling peaks in such systems, in which the coupling motion of a pair of methyl groups plays has such significant effect, will be discussed in more details.

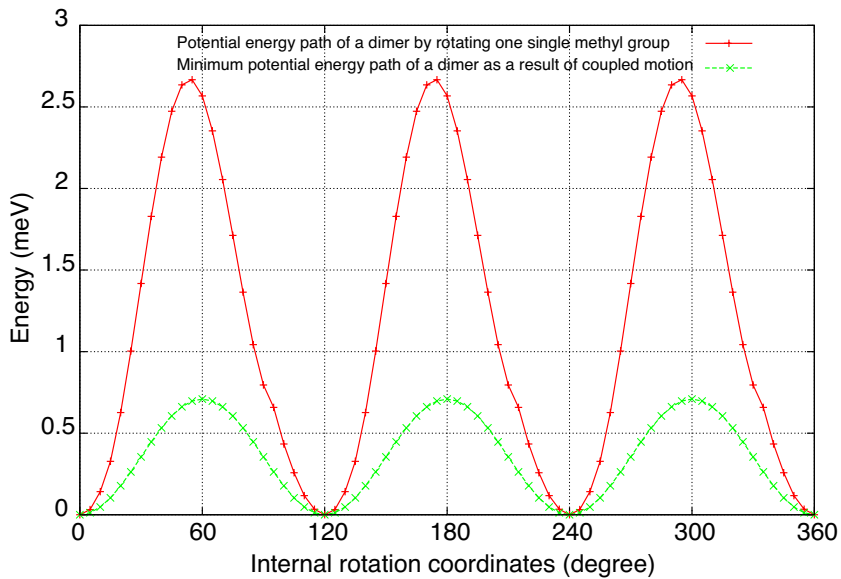


Figure 3.16: A comparison of the minimum energy potential path along line $\phi_1 + \phi_2 = 120$ for a dimer of γ -picoline molecules obtained from Eq. (3.10) (green curve) with the energy potential obtained by rotating one single methyl group of a dimer in the crystal (red curve).

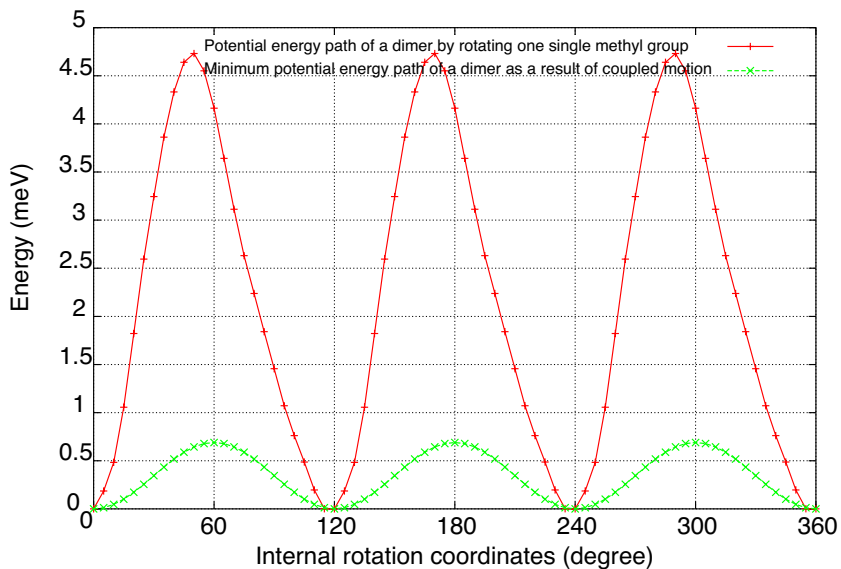


Figure 3.17: A comparison of the minimum energy potential path along line $\phi_1 + \phi_2 = 120$ for a dimer of γ -picoline molecules obtained from Eq. (3.10) (green curve) with the energy potential obtained by rotating one single methyl group of a dimer in the crystal (red curve). The results have been obtained when the dispersion correction was included.

CHAPTER 4

ROTATIONAL TUNNELING OF COUPLED METHYL QUANTUM ROTORS

In this chapter, the influence of rotational coupling between a pair of methyl rotators on the tunneling spectrum is studied. Two interacting adjacent methyl groups are simulated within a coupled-pair model composed of static rotational potential created by the chemical environment and the interaction potential between two methyl groups. The two-dimensional time-independent Schrödinger equation is solved analytically by expanding the wave functions on the basis set of two independent free rotor functions. Three scenarios are investigated, which differ with respect to the relative strength of single-rotor and coupling potential. For each scenario, the dependence of the energy level scheme on the coupling strength is illustrated.

It is found that the main determinant of splitting energy levels tends to be a function of the ratio of strengths of coupling and single-rotor potential. The tunnel splitting caused by coupling is maximized for the coupled rotors in which their total hindering potential is relatively shallow. Such a weakly hindered methyl rotational potential is predicted for γ -picoline at low temperature. The experimental observation of multiple tunneling peaks arising from a single type of methyl group in γ -picoline in the inelastic neutron scattering spectrum is widely attributed to the rotor-rotor coupling.

In this regard, the rotational potential energy surface (PES) of the coaxial pairs of rotors in γ -picoline is calculated using a set of first-principles calculations combined with the nudged elastic band method. Numerov-type method is used to numerically solve the two-dimensional time-independent Schrödinger equation for the calculated 2D-DFT profile. The computed energy levels reproduce the observed tunneling transitions well. Moreover, the calculated density distribution of the three methyl protons resembles the experimental nuclear densities obtained from the Fourier difference method. By mapping the calculated first-principles PES on the model, it is confirmed that the hindering potential in γ -picoline consists of proportionally shallow single-rotor potential to coupling interaction.

4.1 TUNNELING SPECTRUM OF COUPLED METHYL GROUPS WITHIN A COUPLED-PAIR MODEL

The coupled rotation of methyl rotors with parallel axes can be modeled in terms of rotational coordinates. The Hamiltonian operator of two interacting methyl groups can be written down as following:

$$\mathcal{H} = -B\left(\frac{\partial^2}{\partial\phi_1^2} + \frac{\partial^2}{\partial\phi_2^2}\right) + V(\phi_1, \phi_2) \quad (4.1)$$

where I , ϕ_1 , and ϕ_2 stand for the moment of inertia, and the rotational coordinates of two methyl groups, respectively. $B = \hbar^2/2I = 654\mu eV$ is the rotational constant. $V(\phi_1, \phi_2)$ is the potential for a coupled pair of methyl rotors, which can be approximated by:

$$V(\phi_1, \phi_2) = V_3\cos 3\phi_1 + V_3\cos 3\phi_2 + W_3\cos(3\phi_1 - 3\phi_2) \quad (4.2)$$

where the first two terms are threefold periodic potentials with strength V_3 describing the single rotor potential of each individual methyl group. The third term in Eq. (4.2) represents the rotor-rotor coupling with strength W_3 . The Schrödinger equation for the above potential can be solved analytically by expanding the wave functions on linear combinations of products of two free rotor eigenfunctions as shown in Appendix B.

In section 4.2, the energy levels of γ -picoline with the 2D DFT potential profile are calculated, which has no explicit analytical form. In this regard, the two-dimensional Schrödinger variable problem is treated by means of partial discretization with respect to one variable and transforming the partial differential equation into a system of ordinary differential equations, which is solved via classical Numerov-method.³⁵ The discretization has been done in a fine grid of $N = 250$ for the interval $[0, 2\pi]$ that represents a very large Hamiltonian matrix of dimension $N^2 \times N^2$. Periodic boundary conditions are applied using the technique proposed in Ref.³⁴ The Hamiltonian matrices is diagonalized using Lanczos algorithm, which has been well adapted to sparse matrices. The in-house developed Python^{105,106} code is validated by reproducing the eigenvalues of two-dimensional harmonic oscillator and Henon-Heils potential in Ref.³⁵ Furthermore, the eigenvalues for two coupled methyl rotors in the potential defined in Eq. (4.2) are numerically computed (see the Appendix C).

Experimentally, the fingerprint of coupling would show as an asymmetric profile in tunneling spectra that is observable best above $\approx 1\mu eV$ in inelastic neutron

scattering (INS) spectroscopy.¹²¹ Theoretically, the amount of asymmetry can be determined by the strength of potential parameters within the coupled-pair model. Here, the behavior of the lowest energy states of Hamiltonian Eq. (4.1) is studied over a broad ranges of V_3 and W_3 . The results are discussed in three different regimes of: two uncoupled free rotors ($V_3 = 0, W_3 = 0$); two uncoupled rotors in hindered potentials ($V_3 \neq 0, W_3 = 0$); and two coupled rotors ($V_3 \neq 0, W_3 \neq 0$). As it will be discussed, the degeneracy of states depends on the magnitude of V_3 and W_3 . It is shown that the assumption of a pre-defined group of degenerate states over the broad range of potential parameters at once, which is usually seen in the previous studies in this field,^{119,120} may lead to misinterpretation of the spectra. Thereby, the quantum rotational states in terms of methyl symmetry group in different limiting cases is first analyzed. Then a quantitative picture of the influence of coupling on tunneling spectrum is presented.

4.1.1 FREE ROTATION OF TWO ROTORS

The molecular symmetry group of a methyl rotor is C_3 with three irreducible energy state representations: A, E^a , and E^b . Accordingly, the symmetry species of two methyl groups can be represented as the direct product groups $C_3 \times C_3$. In the particular limit of two completely uncoupled free rotors, *i.e.*, $V(\phi_1, \phi_2) = 0$ in Eq. (4.1), the solution to the partial differential equation gives the wavefunction:

$$\Psi_{nm}(\phi_1, \phi_2) = \frac{1}{2\pi} e^{in\phi_1} e^{im\phi_2} \quad (n, m = 0, \pm 1, \pm 2, \pm 3, \dots) \quad (4.3)$$

Where n and m are the rotational quantum numbers. The level scheme of each methyl groups is labeled by their symmetry composed of the non degenerate ground state AA at $\varepsilon=0$, four fold AE level at $\varepsilon=B$, and four fold EE level at $\varepsilon=2B$ (see Figure 4.1).

4.1.2 TWO UNCOUPLED ROTORS IN HINDERED POTENTIALS

Figure 4.2 shows the dependence of the lowest lying energy eigenvalues of the two uncoupled methyl groups as a function of V_3 , *i.e.*, coupling strength W_3 is set to zero in Eq. (4.2). It is evident that the energy levels are equidistant, *i.e.*, the energy difference of AA and AE is equal with that for EE and AE at any strength of V_3 . This means that each of the identical rotors feels the same single-rotor potential and therefore yields the same $A - E$ level splitting. With increasing V_3 , the splitting

$C_3 \times C_3$	n	m	$\varepsilon = B(n^2+m^2)$	Degeneracy	
AA	0	0	0	1	
AE	$\left\{ \begin{array}{l} AE^b \\ E^bA \\ AE^a \\ E^aA \end{array} \right.$	$\left\{ \begin{array}{l} 0 \\ -1 \\ 0 \\ +1 \end{array} \right.$	$\left\{ \begin{array}{l} -1 \\ 0 \\ +1 \\ 0 \end{array} \right.$	B	4
EE	$\left\{ \begin{array}{l} E^aE^b \\ E^bE^a \\ E^aE^a \\ E^bE^b \end{array} \right.$	$\left\{ \begin{array}{l} +1 \\ -1 \\ +1 \\ -1 \end{array} \right.$	$\left\{ \begin{array}{l} -1 \\ +1 \\ +1 \\ -1 \end{array} \right.$	2B	4

Figure 4.1: The energy levels of two completely uncoupled free rotors. n and m are the rotational quantum numbers of the free-rotor wavefunction.

decreases quickly. In the limit of large single rotor potential $V_3 > 15$ meV, the first order of Taylor series expansion about the minima of the cosine potential leads to harmonic approximation with the oscillation frequency $\omega_0 = \sqrt{9V_3/I}$. In this limit, the next energy levels are approximately equally spaced with the energy $\hbar\omega_0$ as the level spacing of the harmonic oscillator is constant $\Delta E = E_{n+1} - E_n = \hbar\omega_0$.

4.1.3 TWO COUPLED ROTORS

The low temperature dynamics of weakly hindered methyl rotation is experimentally interesting because it yields a large tunnel splitting. Hence, to take a closer look at the behavior of the lowest eigenvalues, a shallow potential of $V_3 = 5$ meV is chosen. Figure 4.3 shows the energetical behavior of the lowest rotational quantum levels of two coupled rotors with strength of $V_3 = 5$ meV along with energy level scheme for a large range of couplings W_3 . The dashed lines in Fig. 4.3 indicate the different limits of coupling strength. The following trends can be seen:

(1) For $W_3 < V_3$ (see Fig. 4.3(a)), two rotors are weakly coupled. Thus, the same characteristics described in section 4.1.2 can be seen. The degeneracies of eigenvalues are similar to those for two uncoupled free rotors.

(2) For $V_3 < W_3 < 1.5V_3$ (see Fig. 4.3(b)), the rotor-rotor coupling W_3 is reasonably strong compared to the single-rotor potential. It is seen that the coupling causes the shift in the energy levels and removes the degeneracies of EE level. Therefore, four possible transitions are expected in the ground-state multiplet as $|AA\rangle \rightarrow |AE\rangle$, $|AE\rangle \rightarrow |E^aE^b\rangle$, $|AE\rangle \rightarrow |E^aE^a\rangle$, and $|E^aE^b\rangle \rightarrow |E^aE^a\rangle$.¹²⁰

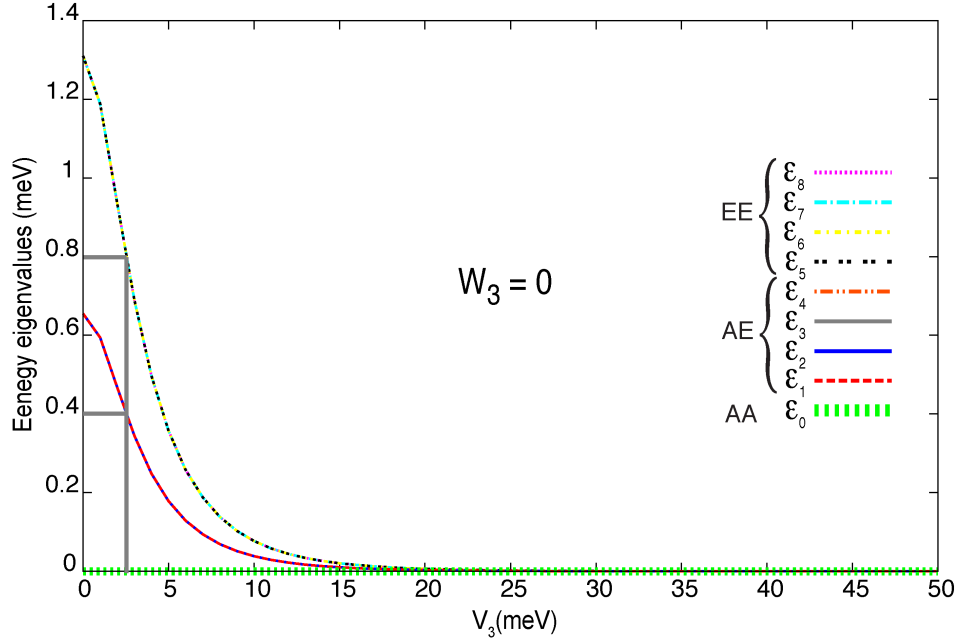


Figure 4.2: Dependence of the lowest lying energy eigenvalues of the two uncoupled methyl groups on the strength V_3 . Note that $\varepsilon(\text{EE})-\varepsilon(\text{AE})=\varepsilon(\text{AE})-\varepsilon(\text{AA})$ for any V_3 , i.e, the energy levels are equidistant. The vertical line at $V_3= 2.5$ meV is drawn to illustrate an example of equidistant energy levels.

(3) In the previous studies,^{119,120} it has been speculated that AE energy level remains four fold degenerate for all cases and coupling merely breaks the degeneracy of EE level. Figure. 4.3(c) supports the above speculations. However, upon close inspection of the evolution of the eigenvalues as function of W_3 , it turns out that there is a level crossing¹²²⁻¹²⁴ at about $W_3 \approx 12$ meV, in which $\varepsilon(\text{E}^a\text{E}^b) < \varepsilon(\text{AE})$.

(4) In the limit of very strong coupling $W_3 > 30$ meV, the energy $\varepsilon(\text{E}^a\text{E}^b) \rightarrow 0$, and the first three levels become degenerate following with a six fold degenerate states.

In order to indicate that the above trends are general and seen at all single particle potential strengths either lower or larger than $V_3 = 5$ meV, the dependence of the lowest energy eigenvalues of coupled-pair model are presented as a function of W_3 for different single particle potentials, $V_3 = 0$, $V_3 = 10$, and $V_3 = 30$ meV (see Fig. 4.4).

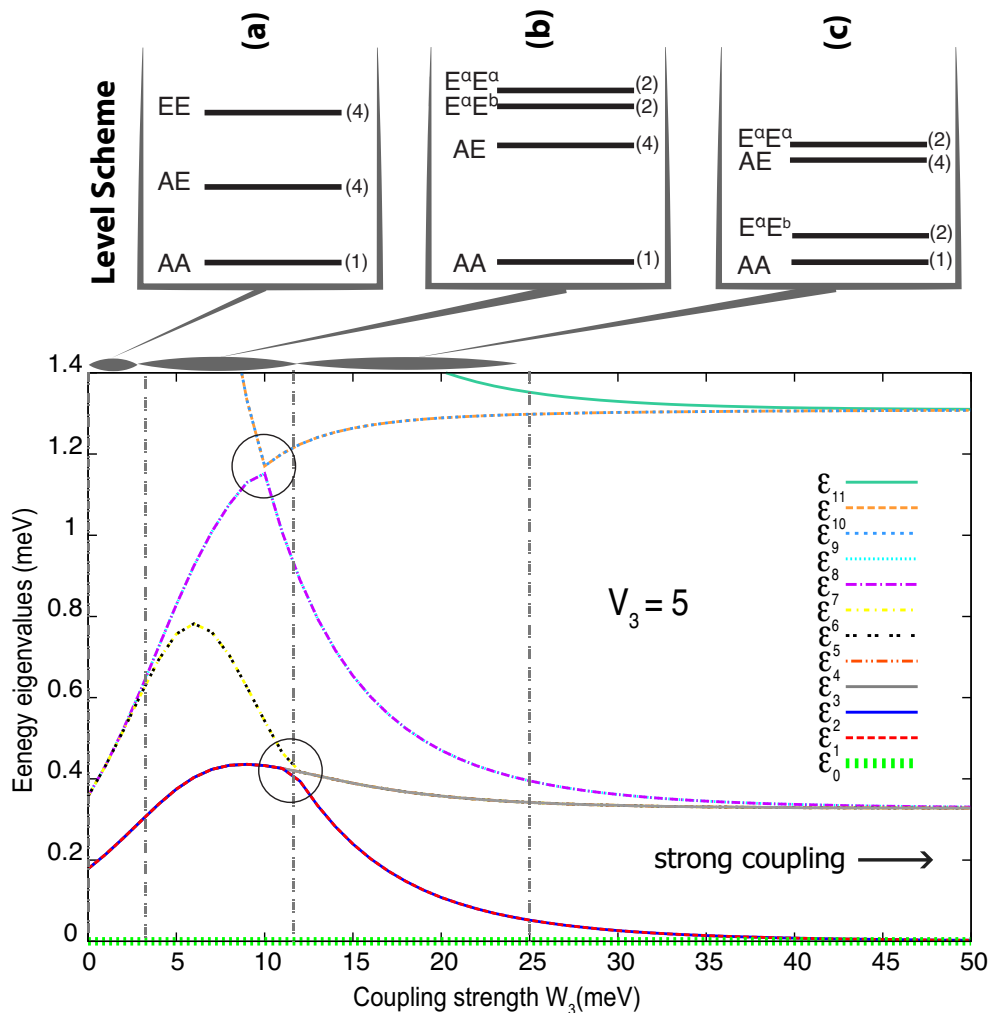


Figure 4.3: (Bottom) Dependence of the lowest lying energy eigenvalues of the two coupled methyl groups on the coupling strength W_3 . Each single CH_3 rotors is subject to a potential of strength $V_3=5$ meV. (Top) The energy level schemes of a pair of CH_3 groups corresponding to regions labeled a, b, and c of coupling strength. Avoided level crossings are highlighted by the black circles.

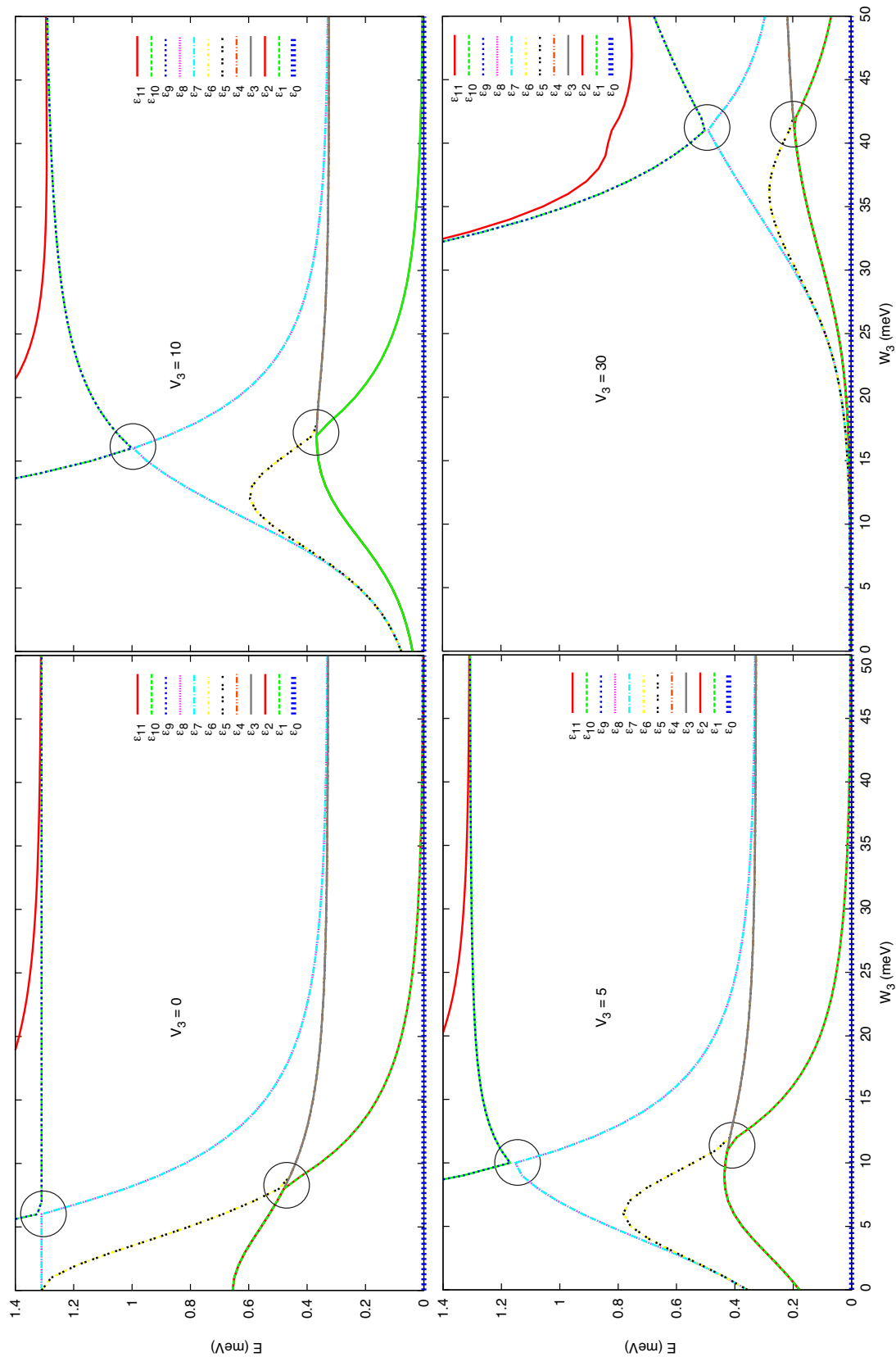


Figure 4.4: Dependence of the lowest lying energy eigenvalues of the two coupled methyl groups on the coupling strength W_3 . Each single CH_3 rotors is subject to a potential of strength V_3 .

4.1.4 QUANTITATIVE PICTURE OF THE INFLUENCE OF COUPLING ON TUNNELING SPECTRUM

Figure 4.5 shows the energy difference between the two lowest eigenvalues of Eq. (4.1) as a function of the strength of coupling and single rotor potential, which can also be considered as a measure of the influence of coupling on splitting the tunneling lines. The following trends can be seen:

(1) The rotation splitting in the order of rotational constant ($B = 654\mu eV$) originates from two almost free uncoupled methyl groups.

(2) The large value of splitting above $500\mu eV$ and less than rotational constant is obtained for weakly hindered potential in which, the single rotor potential is shallow and coupling term is less than 5 meV .

(3) In the limit of strong V_3 and shallow W_3 , tunnel splitting goes to zero, and vice versa.

(4) The effect of coupling on splitting of energy levels not only is visible for shallow single-rotor potential of V_3 , but also for deep potentials as long as the interaction between two methyl rotors are strong enough. As it can be seen, when both V_3 and W_3 are large, the tunnel splitting decreases gradually for the ratio $W_3/V_3 \approx 1.5$, and quickly vanishes for ratios above ≈ 1.5 .

4.2 COUPLED METHYL QUANTUM ROTATION IN γ -PICOLINE

Turning from the discussion of the more abstract model Hamiltonian Eq. (4.1) to the real system, the specific case of γ -picoline has been chosen as it exhibits two spatially opposed methyl groups in the crystal structure. Crystalline γ -picoline (also called 4-methylpyridine, $\text{CH}_3\text{C}_5\text{H}_4\text{N}$) has been the subject of many NMR and INS experimental studies.^{1-5,7,121,125,126} The interest is arising from the remarkable freedom of methyl rotation at low temperature. As it is outlined in previous chapter, the possibility of a mechanical coupling between coaxial pairs of methyl groups makes γ -picoline as an ideal choice to be studied within coupled-pair model. The geometrical structure extracted by combined x-ray and neutron diffraction¹¹⁵ has the space group of $(I4_1/a)$. The tetragonal structure has eight equivalent molecules per unit cell with $a = b = 7.62$ and $c = 18.62$ Å lattice parameters (see Fig. 4.6). The methyl rotational axes are parallel to the c axis and the shortest intermolecular distance occurs between face-to-face methyl groups. The following sections present the ro-

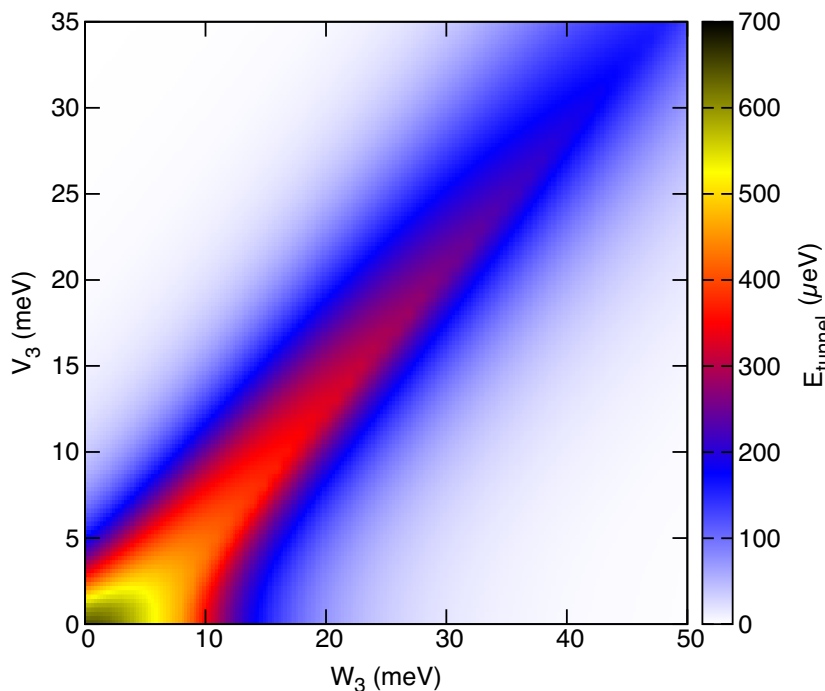


Figure 4.5: Dependence of tunnel splitting (*i.e.*, the energy difference between the first two rotational states) of two coupled methyl groups on coupling strength W_3 and single particle potential strength V_3 (see Eq. (4.1)).

tational quantum states of two face-to-face methyl groups in the actual γ -picoline crystal structure while the rotational potential is obtained from DFT calculations.

4.2.1 DETERMINATION OF TWO-DIMENSIONAL POTENTIAL ENERGY SURFACE

In previous chapter, the tunnel splitting in γ -picoline was investigated within single particle model (SPM). The 2D rotational potential was calculated for a cluster of two γ -picoline molecules, and the obtained minimum path was adjusted within 1-D single particle model. Accordingly, the energy levels were obtained by solving the 1-D Schrödinger equation. Although the SPM was able to predict the main tunnel splitting energy successfully, however it failed to predict higher tunneling transitions.¹²⁷ Here, a set of first principles calculations are performed to compute the 2D PES for a pair of interacting methyl groups while full details of crystal environments, *i.e.*, all neighboring molecules are taken into accounts in the calculations. Correspondingly, here the 2-D Schrödinger equation is numerically solved using the obtained 2D PES without assuming any particular energy path to obtain multiplet

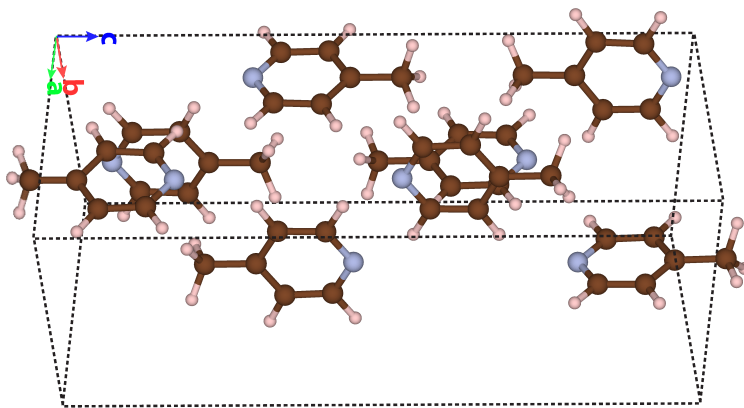


Figure 4.6: Unit cell of γ -picoline.

structure of tunneling transitions.

The first-principles calculations were performed within the Kohn-Sham density functional theory (DFT) with the Becke-Lee-Yang-Parr (BLYP) exchange correlation functional^{48,51} and dispersion correction DFT-D3 by Grimme *et al.*^{53,67,68} The Gaussian Plane Wave (GPW) method^{128,129} with GTH pseudopotentials^{74,75} were employed. A gaussian basis sets of triple zeta with valence polarization(TZVP) with a cutoff energy of 400 Ry was used. A super cell of $2 \times 2 \times 1$ was used to avoid the interaction between the probe rotor molecule and its neighboring periodic images. The positions of atoms were fully optimized using Broyden-Fletcher-Goldfarb-Shanno (BFGS) method.

After structural optimization, the 2D PES of face-to-face methyl groups was computed as a function of the rotation angles ϕ_1 and ϕ_2 by performing DFT calculations combined with climbing image nudged elastic band (CI-NEB) method.²⁸ ϕ_1 and ϕ_2 refer to the rotational angles of the probe rotor and its counterpart rotor. The computed 2D rotational potential is obtained at 5 degree rotations of each methyl groups. Due to C_3 rotational symmetry, only data points in the range from 0° to 120° are needed. Therefore, for each CI-NEB calculations, a band with 24 replicas of the molecular crystal was set. In this regard, all degrees of freedom of the environment as well as both methyl groups were allowed to relax under periodic boundary condition. All the calculations were carried out using CP2K code.⁹⁵ Figure 4.7 shows the calculated 2D PES of the coupled rotors in γ -picoline. Subsequently, the obtained rotational potential from the DFT calculation is used to solve the 2D Schrödinger for the coupled rotors in γ -picoline.

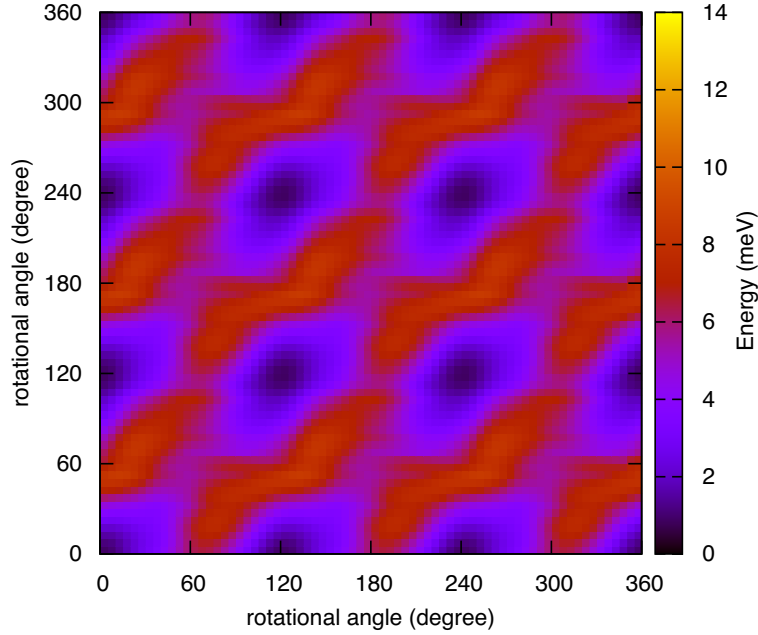


Figure 4.7: 2D potential energy surface for two face-to-face methyl groups in γ -picoline crystal obtained by DFT calculation. The dispersion correction is included. X and Y axes indicate the rotational angles of the rotors.

4.2.2 ENERGY-LEVELS AND DENSITY DISTRIBUTION OF METHYL PROTONS

Initially, the INS experiments on rotational tunneling of γ -picoline revealed a tunneling transition at ≈ 0.500 meV. However, further INS experiments using higher resolution spectrometers ($\approx 9\mu\text{eV}$) done at low temperature of 0.5 K revealed there exists three bands: an intense band at 0.516 meV, and two weaker bands at 0.470 meV, and 0.537 meV,¹²¹ in which the weaker bands are tentatively assigned to the coupled pair of methyl groups.¹²⁶ In this regard, Figure 4.8 shows the calculated eigenvalues and the energy level schematic for the low-energy transitions for γ -picoline. Among the four transitions predicted in Figure 4.8, three of them can be assigned to the experimentally observed transitions. Within the coupled-pair model, it is indicated that the largest transition $|AE\rangle \rightarrow |E^a E^b\rangle$ at 0.515 meV and the transition $|AE\rangle \rightarrow |E^a E^a\rangle$ at 0.431 result from coupling effect on splitting the EE level. The second largest transition $|AA\rangle \rightarrow |AE\rangle$ at 0.486 is interpreted as so-called tunnel splitting. The results confirm that a coupled motion of methyl librations can be considered as the most likely effective factor describing methyl dynamics and corresponding experimentally observed transitions in γ -picoline.

The strength of coupling and single particle potential in γ -picoline crystal can be estimated by fitting the model of coupled-pair potential, Eq. (4.2), to the calculated first principle 2D PES of γ -picoline, discussed in section 4.1. It is seen from 2D PES that hindering rotational potential is minimum for $\phi_1 = \phi_2 - (2\pi/3)q$ where $q \in \mathbb{Z}$. The one-dimensional minimum path can be plotted as a function of one single rotational variable. Table 4.1 shows the parameters of the coupled-pair model obtained through fitting. Figure 4.9 shows the low hindering potential of about 8.40 meV. It indicates that the low hindering rotational potential of γ -picoline results from the shallow single rotor and shallow coupling potential. These results agree well with what discussed in section 4.1, and particularly with the quantitative image of tunnel splitting given in Figure 4.5. The similar analysis on a dimer of γ -picoline,¹²⁷ discussed in the previous chapter, showed a coupling strength of about seven times larger than single particle potential. However, the current calculations show that it is almost 1.4 times larger when full atomic environment in the crystal is taken into account. This highlights the influence of the other molecules in crystal structure on hindering methyl rotational dynamics.

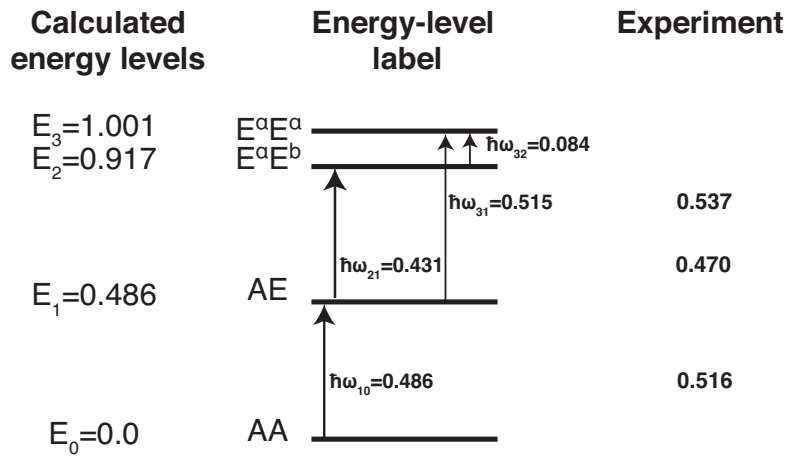


Figure 4.8: Energy-level diagram and tunneling transitions of γ -picoline crystal, calculated by numerically solving 2D Schrödinger equation with the obtained 2D DFT potential, Fig. (4.6). The experimentally observed transitions¹²¹ are included as a guide. Energies are in meV.

The effect of crystal field is also visible on proton density distribution. Experimentally, the nuclear density distribution of the three methyl protons in rotational plane can be obtained through the Fourier difference method using the single-crystal neutron diffraction data.²³ The experimental map is a graphic view of the protons

Table 4.1: Fitted parameters through mapping of Eq. (4.2) to the computed 2D PES obtained from DFT for two face-to-face methyl groups in γ -picoline.

Molecular crystal	CP model potentials parameters (in meV)
γ -picoline	$V_3=2.48$, $W_3=3.44$

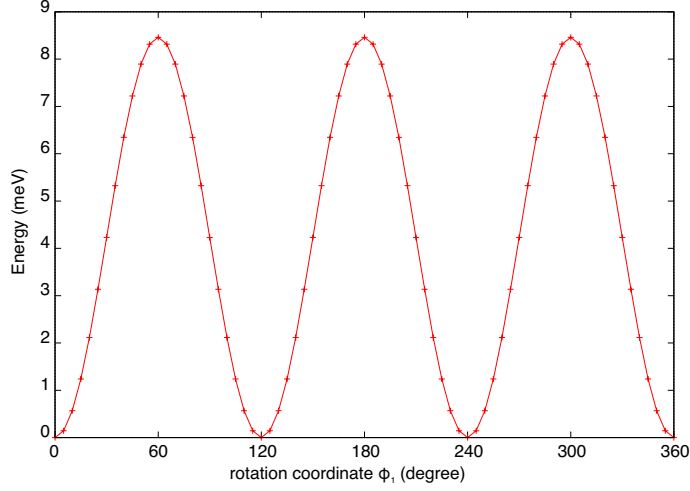


Figure 4.9: Minimum energy potential path along the line $\phi_1 = \phi_2 - 2\pi/3$ of a pair of γ -picoline molecules in crystal is obtained by mapping the couple-pair model potential, Eq. (4.2) to the computed 2D PES.

confined in a plane perpendicular to the rotational axis, which cannot be produced by simple rotation of a methyl group. Here, it is possible to construct the proton density map by analyzing the geometrical structures obtained from NEB calculations, where the protons locate on their minimum energy paths. Thereby, the position of protons are collected from the optimized band of replicas. The density distribution can be constructed by summation on the distribution of protons due to the isotropic thermal factor, which is a gaussian in shape and can be represented as:

$$\rho(x, y, T) = \left(\frac{1}{\pi \langle u_{iso}^2 \rangle_T} \right)^{1/2} \sum_{i=1}^n \exp \left[- \frac{(x - x_i)^2 + (y - y_i)^2}{\langle u_{iso}^2 \rangle_T} \right] \quad (4.4)$$

where the summation is taken over all methyl protons in the optimized band of replicas and the isotropic thermal factor $\langle u_{iso}^2 \rangle_T$ at the temperature $T=10$ K is 0.0194 (\AA)².²³ The isotropic thermal factor is comprised of the mean square amplitude for proton displacements (internal vibrations) and isotropic librations of molecular en-

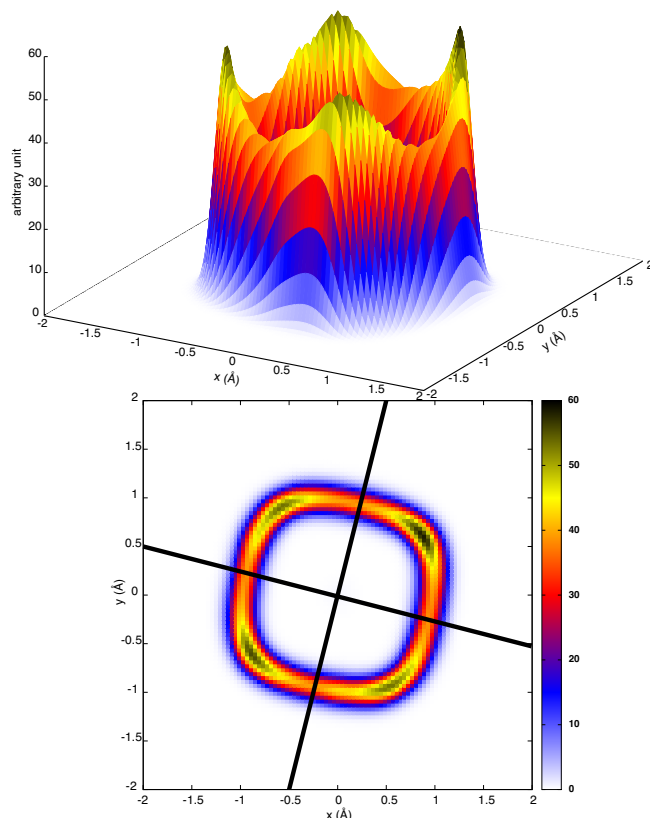


Figure 4.10: Landscape view (top) and projected map (bottom) of the calculated proton density distribution in rotational plane of methyl protons of γ -picoline crystal for a single methyl group at low temperature. The solid lines represent the orientations of aromatic rings.

tities (lattice thermal factor). Figure 4.10 shows the calculated density distribution map for rotating methyl protons of a single methyl group in crystal. The rotating path is tilted as the molecular planes of molecules with respect to crystal plane are tilted. The solid lines show the orientation of the molecular planes. The calculated proton density distribution for the methyl group is very similar to that extracted from the experimental data published in Ref.²³ Therefore, in order to describe the methyl dynamics accurately, the full details of molecular environment should be taken into account.

CHAPTER 5

CONCLUSIONS AND FUTURE WORK

This work deals with the numerical determination of tunneling splittings of rotating methyl groups in realistic chemical environments in the condensed phase. The specific interest for rotational tunneling splittings is their relevance for nuclear magnetic resonance^{1-5, 7, 125, 130} (NMR) hyperpolarization via the Haupt effect, where the thermal population difference between the lowest rotational states is transferred to the spin population, causing a significantly larger spin polarization than the thermal spin population distribution would yield. Complementary interest stems from the field of inelastic Neutron scattering^{29, 121, 126, 131} (INS) spectroscopy, where the low-temperature rotational energy spectrum can be measured directly.

The tunneling splitting energy, which characterizes the lowest rotational quantum excitation, is directly correlated to the NMR signal amplitude amplification in hyperpolarization experiments. In 2012, Berger *et al.*^{1, 2} reported a large signal enhancement in methyl carbon-13 upon a temperature jump in a sample containing γ -picoline in liquid-state NMR. Levitt *et al.*⁴⁻⁶ presented a theoretical framework for the mechanism of hyperpolarization effects in liquid-state NMR, termed quantum rotor induced polarization⁷ (QRIP). A year later, a systematic experimental study, done by Berger *et al.*,¹²⁵ on more than 40 substances showed that a larger tunnel splitting leads to a higher NMR signal enhancement. However, what is missing up to now is a thorough understanding of the relationship between the tunnel splitting and local molecular structure in terms of chemical composition and chemical environment of a methyl group. Here, the present thesis fills this gap and provides a comprehensive quantum chemical toolbox for the numerical determination of tunnel splitting values of methyl rotors in arbitrary condensed-phase environments.

The first part of this work is focused on theoretical approaches for the calculation of tunneling splittings. In this regard, a semiclassical approach is introduced for the calculation of tunneling splittings of methyl groups based on the rotational potential computed at the level of density functional theory. Besides, two semiclassical methods are summarized and examined for a polyatomic molecule and several one-dimensional models of potential energy functions.

The second part of this work deals with the application of the tunneling splitting

approach on molecular crystals containing methyl groups. Two chemically almost identical molecules, γ -picoline and toluene, are investigated while show very different hyperpolarization capabilities in the experiments. The approach developed here is able to reproduce quantitatively the observed tunnel splitting in the experiment. The large difference in magnitude of tunneling splitting is explained by the intermolecular interactions arising from the crystal packing and coupling motion of methyl groups.

As an important aspect, the effect of coupled rotations on tunneling spectrum is investigated for a pair of coupled methyl groups within a simple coupled-pair model. The calculations showed that an individual increase either in coupling or single-particle potential strength yields vanishing splitting. As single particle potential and interaction proportionally increases, the relative splitting caused by coupling effect decreases and goes towards a constant. As a real system for the coupled-pairs model of methyl groups, γ -picoline is studied. A theoretical explanation for the observed multiple tunneling transition in the INS experiment¹²¹ of γ -picoline within a coupled-pair model is given. The calculated energy levels agree well with the measured spectrum. Additionally, the magnitude of rotor-rotor coupling in γ -picoline crystal is found to be as shallow as a single particle potential. The results confirm that a coupled-pair model can be considered as an appropriate model to describe the rotational dynamics and thereby associated transitions in γ -picoline.

Work is in progress to develop strategies for (a) using quantum methyl rotors as protein analysis tool with a predictive site-selectivity, and (b) the rational design of biochemical mutations to optimize the site-specific NMR signal amplification.

BIBLIOGRAPHY

- [1] M. Icker and S. Berger. Unexpected multiplet patterns induced by the Haupt-effect. *J. Magn. Reson.*, 219:1–3, 2012.
- [2] M. Icker, P. Fricke, and S. Berger. Transfer of the Haupt-hyperpolarization to neighbor spins. *J. Magn. Reson.*, 223:148–150, 2012.
- [3] J. Haupt. A new effect of dynamic polarization in a solid obtained by rapid change of temperature. *Phys. Lett. A.*, 38(6):389–390, 1972.
- [4] B. Meier, J. N. Dumez, G. Stevanato, J. T. Hill-Cousins, S. S. Roy, P. Håkansson, S. Mamone, R. C.D. Brown, G. Pileio, and M. H. Levitt. Long-lived nuclear spin states in methyl groups and quantum-rotor-induced polarization. *J. Am. Chem. Soc.*, 135(50):18746–18749, 2013.
- [5] J. N. Dumez, P. Håkansson, S. Mamone, B. Meier, G. Stevanato, J. T. Hill-Cousins, S. S. Roy, R. C.D. Brown, G. Pileio, and M. H. Levitt. Theory of long-lived nuclear spin states in methyl groups and quantum-rotor induced polarisation. *J. Chem. Phys.*, 142(4), 2015.
- [6] S. S. Roy, J. N. Dumez, G. Stevanato, B. Meier, J. T. Hill-Cousins, R. C.D. Brown, G. Pileio, and M. H. Levitt. Enhancement of quantum rotor NMR signals by frequency-selective pulses. *J. Magn. Reson.*, 250:25–28, 2015.
- [7] C. Ludwig, M. Saunders, I. Marin-Montesinos, and U. L. Gunther. Quantum rotor induced hyperpolarization. *Proc. Nat. Acad. Sci. U. S. A.*, 107(24):10799–10803, 2010.
- [8] M. A. Suhm and R. O. Watts. Quantum monte carlo studies of vibrational states in molecules and clusters. *Phys. Rep.*, 204:293, 1991.
- [9] R. P. Feynman. Statistical mechanics: A set of lectures. (*Reading, Mass.: W. A. Benjamin*), 1972.
- [10] R. P. Feynman and A. R. Hibbs. Quantum mechanics and path integrals. (*New York: McGraw-Hill*), 1965.
- [11] A. Kuki and P. G. Wolynes. *Electronic tunneling paths in proteins*, pages 49–83. Springer Berlin Heidelberg, Berlin, Heidelberg, 1991.

- [12] M. Marchi and D. Chandler. Path-integral calculation of the tunnel splitting in aqueous ferrous–ferric electron transfer. *The Journal of Chemical Physics*, 95(2):889–894, 1991.
- [13] G. Wentzel. Eine verallgemeinerung der quantenbedingungen für die zwecke der wellenmechanik. *Zeitschrift für Physik*, 38(6):518–529, Jun 1926.
- [14] H. A. Kramers. Wellenmechanik und halbzahlige quantisierung. *Zeitschrift für Physik*, 39:828–840, 1926.
- [15] L. Brillouin. La mecanique ondulatoire de schrödinger une methode generale de resolution par approximations successives. *Comptes Rendus de l'Academie de Sciences*, 24, 1926.
- [16] J. O. Richardson. *Ring-Polymer Approaches to Instanton Theory (Doctoral dissertation)*. Pembroke College, University of Cambridge, 2012.
- [17] J. O. Richardson and S. C. Althorpe. Ring-polymer instanton method for calculating tunneling splittings. *J. Chem. Phys.*, 134:054109, 2011.
- [18] Y. Ootani and T. Taketsugu. Ab initio molecular dynamics approach to tunneling splitting in polyatomic molecules. *J. Comput. Chem.*, 33:60, 2012.
- [19] N. Makri and W. H. Miller. A semiclassical tunneling model for use in classical trajectory simulations. *J. Chem. Phys.*, 91:4026, 1989.
- [20] J. O. Richardson, S. C. Althorpe, and D. J. Wales. Instanton calculations of tunneling splittings for water dimer and trimer. *J. Chem. Phys.*, 135:124109, 2011.
- [21] G. Mil'nikov and H. Nakamura. Practical implementation of the instanton theory for the ground-state tunneling splitting. *J. Chem. Phys.*, 115:6881, 2001.
- [22] M. A. Neumann, M. Plazanet, M. R. Johnson, and H. P. Trommsdorff. Rotation-libration and rotor-rotor coupling in 4-methylpyridine. *J. Chem. Phys.*, 120(2):885–897, 2004.
- [23] F. Fillaux, B. Nicolai, W. Paulus, E. Kaiser-Morris, and A. Cousson. Collective rotational tunneling of methyl groups and quantum solitons in 4-

- methylpyridine: Neutron scattering studies of single crystals. *Phys. Rev. B*, 68(22):1–13, 2003.
- [24] M. Neumann and M. R. Johnson. Methyl group tunneling—A quantitative probe of atom–atom potentials. *J. Chem. Phys.*, 107(6):1725–1731, 1997.
- [25] M. R. Johnson and G.J. Kearley. Tunneling of coupled methyl groups. *Annu. Rev. Phys. Chem.*, 51(2):297–321, 2000.
- [26] G. Mills and H. Jónsson. Quantum and thermal effects in H₂ dissociative adsorption: evaluation of free energy barriers in multidimensional quantum systems. *Phys. Rev. Lett.*, 72:1124, 1994.
- [27] G. Mills, H. Jónsson, and G. K. Schenter. Reversible work transition state theory: application to dissociative adsorption of hydrogen. *Surf. Sci*, 324:305, 1995.
- [28] G. Henkelman, B. P. Uberuaga, and H. Jónsson. Climbing image nudged elastic band method for finding saddle points and minimum energy paths. *J. Chem. Phys.*, 113(22):9901–9904, 2000.
- [29] F. Fillaux and C. J. Carlile. Inelastic-neutron-scattering study of methyl tunneling and the quantum sine-gordon breather in isotopic mixtures of 4-methylpyridine at low temperature. *Phys. Rev. B.*, 42:5990–6006, 1990.
- [30] P. C. Hohenberg and W. Kohn. Inhomogeneous electron gas. *Phys. Rev. B*, 136:864, 1964.
- [31] W. Kohn and L. J. Sham. Self-consistent equations including exchange and correlation effects. *Phys. Rev.*, 140:A1133–A1138, 1965.
- [32] R. O. Jones and O. Gunnarsson. The density functional formalism, its applications and prospects. *Rev. Mod. Phys.*, 61:689–746, Jul 1989.
- [33] R. G. Parr. *Density Functional Theory of Atoms and Molecules*, pages 5–15. Springer Netherlands, Dordrecht, 1980.
- [34] M. Pillai, J. Goglio, and T. G. Walker. Matrix Numerov method for solving Schrödinger’s equation. *Am. J. Phys.*, 80:1017, 2012.

- [35] Z. Kalogiratou, Th. Monovasilis, and T. E. Simos. Numerical solution of the two-dimensional time independent Schrödinger equation with Numerov-type methods. *J. Math. Chem.*, 37:271–279, 2005.
- [36] R. M. Martin. Electronic structure: Basic theory and practical methods. *Contemp. Phys.*, 52(1):77–77, 2011.
- [37] G. I. Kerley. On corrections to the born-oppenheimer approximation. *arXiv:1306.6574*, 2013.
- [38] D. R. Hartree. *Proc. R. Soc. London*, A113:621, 1928.
- [39] H. F. Hameka. *Quantum Mechanics: A Conceptual Approach*. John Wiley and Sons, Inc., Hoboken, NJ, USA, 2004.
- [40] C. D. Sherrill and H. F. Schaefer. The configuration interaction method: Advances in highly correlated approaches. volume 34 of *Advances in Quantum Chemistry*, pages 143 – 269. Academic Press, 1999.
- [41] J. Čížek. On the correlation problem in atomic and molecular systems. calculation of wavefunction components in ursell-type expansion using quantum-field theoretical methods. *J. Chem. Phys.*, 45(11):4256–4266, 1966.
- [42] J. Čížek. *Adv. Chem. Phys.*, 14, 1969.
- [43] J. Čížek and J. Paldus. *Int. J. Quantum. Chem. Symp.*, 5:351, 1971.
- [44] C. Møller and M. S. Plesset. Note on an approximation treatment for many-electron systems. *Phys. Rev.*, 46:618–622, 1934.
- [45] R. A. Evarestov. *Symmetry and ab-initio Calculations of Nanolayers, Nanotubes and Nanowires*, pages XIV, 672. Springer-Verlag Berlin Heidelberg, 2015.
- [46] S.H. Vosko, L. Wilk, and M. Nusair. Accurate spin-dependent electron liquid correlation energies for local spin density calculations: a critical analysis. *Can. J. Phys.*, 58:1200, 1980.
- [47] J. P. Perdew and W. Yue. Accurate and simple density functional for the electronic exchange energy: Generalized gradient approximation. *Phys. Rev. B*, 33:8800–8802, Jun 1986.

- [48] A. D. Becke. Density-functional exchange-energy approximation with correct asymptotic behavior. *Phys. Rev. A.*, 38(6):3098–3100, 1988.
- [49] P. Jemmer and P. J. Knowles. Exchange energy in kohn-sham density-functional theory. *Phys. Rev. A*, 51:3571–3575, May 1995.
- [50] A. D. Becke. Density-functional thermochemistry. iv. a new dynamical correlation functional and implications for exact-exchange mixing. *J. Chem. Phys.*, 104:1040, 1996.
- [51] C. Lee, W. Yang, and R. G. Parr. Development of the Colle-Salvetti correlation-energy formula into a functional of the electron density. *Phys. Rev. B.*, 37(2):785–789, 1988.
- [52] L. A. Curtiss, K. Raghavachari, P.C. Redfern, and J.A. Pople. Assessment of gaussian-2 and density functional theories for the computation of enthalpies of formation. *J. Chem. Phys.*, 106:1063, 1997.
- [53] S. Grimme. Semiempirical gga-type density functional constructed with a long-range dispersion correction. *J. Comput. Chem.*, 27(15):1787–1799, 2006.
- [54] H. Iikura, T. Tsuneda, T. Yanai, and K. Hirao. A long-range correction scheme for generalized-gradient-approximation exchange functionals. *J. Chem. Phys.*, 115:3540, 2001.
- [55] J. Heyd, G.E. Scuseria, and M.J. Ernzerhof. Hybrid functionals based on a screened coulomb potential. *Chem. Phys.*, 118:8207, 2003.
- [56] T. Yanai, D.P. Tew, and N.C. Handy. A new hybrid exchange?correlation functional using the coulomb-attenuating method (cam-b3lyp). *Chem. Phys. Lett.*, 51:393, 2004.
- [57] A. J. Cohen, P. Mori-Sánchez, and W. Yang. Challenges for density functional theory. *Chemical Reviews*, 112(1):289–320, 2012. PMID: 22191548.
- [58] A. C. Tsipis. Dft flavor of coordination chemistry. *Coordination Chemistry Reviews*, 272(Supplement C):1 – 29, 2014.
- [59] P. A. M. Dirac. Note on exchange phenomena in the thomas atom. *Math. Proc. Camb. Phil. Soc.*, 26:376–385, 1930.

- [60] D. M. Ceperley and B. J. Alder. Ground state of the electron gas by a stochastic method. *Phys. Rev. Lett.*, 45:566–569, Aug 1980.
- [61] J. P. Perdew, K. Burke, and M. Ernzerhof. Generalized gradient approximation made simple. *Phys. Rev. Lett.*, 77:3865–3868, Oct 1996.
- [62] W. Koch and M. C. Holthausen. Second Edition, Wiley-VCH, Weinheim, Germany, 2008.
- [63] D. Rappoport, N. R. M. Crawford, F. Furche, and K. Burke. Which functional should i choose? 2008.
- [64] F.Z. London. *Phys. Chem*, 11, 1930.
- [65] H. C. Longuet-Higgins. Spiers memorial lecture: Intermolecular forces. *Discuss. Faraday Soc.*, 40:7–18, 1965.
- [66] E. Zaremba and W. Kohn. Van der waals interaction between an atom and a solid surface. *Phys. Rev. B.*, 13(6):2270–2285, 1976.
- [67] S. Grimme, J. Antony, S. Ehrlich, and H. Krieg. A consistent and accurate ab initio parametrization of density functional dispersion correction (DFT-D) for the 94 elements H-Pu. *J. Chem. Phys.*, 132(15), 2010.
- [68] S. Grimme. Accurate description of van der waals complexes by density functional theory including empirical corrections. *J. Comput. Chem.*, 25(12):1463–1473, 2004.
- [69] A. Tkatchenko and M. Scheffler. Accurate molecular van der waals interactions from ground-state electron density and free-atom reference data. *Phys. Rev. Lett.*, 102:073005, 2009.
- [70] A. D. Becke and E. R. Johnson. Exchange-hole dipole moment and the dispersion interaction. *J. Chem. Phys.*, 122(15):154104, 2005.
- [71] A. D. Becke and E. R. Johnson. A density-functional model of the dispersion interaction. *J. Chem. Phys.*, 123(15):154101, 2005.
- [72] Li. Guanna. *Computational Chemistry of Catalytic Biomass Conversion*, pages X, 198. Springer Singapore, 2016.

- [73] M. Dion, H. Rydberg, E. Schröder, D. C. Langreth, and B. I. Lundqvist. Van der waals density functional for general geometries. *Phys. Rev. Lett.*, 92(24):246401, 2004.
- [74] C. Hartwigsen, S. Goedecker, and J. Hutter. Relativistic separable dual-space Gaussian pseudopotentials from H to Rn. *Phys. Rev. B.*, 58:103–128, 1998.
- [75] S. Goedecker, M. Teter, and J. Hutter. Separable dual-space Gaussian pseudopotentials. *Phys. Rev. B.*, 54:1703, 1996.
- [76] E. Bylaska, K. Tsemekhman, N. Govind, and M. Valiev. *3. Large-Scale Plane-Wave-Based Density Functional Theory: Formalism, Parallelization, and Applications*, pages 77–116. John Wiley and Sons, Inc., Hoboken, NJ, USA, 2011.
- [77] M. C. Payne, M. P. Teter, D. C. Allen, T. A. Arias, and Joannopoulos J. D. Iterative minimization techniques for ab initio total-energy calculations: molecular dynamics and conjugate gradients. *Rev. Mod. Phys.*, 64:1045, 1992.
- [78] D. R. Hamann, M. Schlüter, and C. Chiang. Norm-conserving pseudopotentials. *Phys. Rev. Lett.*, 43:1494–1497, Nov 1979.
- [79] G. B. Bachelet, D. R. Hamann, and M. Schlüter. Pseudopotentials that work: From h to pu. *Phys. Rev. B*, 26:4199–4228, Oct 1982.
- [80] N. Troullier and José Luís Martins. Efficient pseudopotentials for plane-wave calculations. *Phys. Rev. B*, 43:1993–2006, Jan 1991.
- [81] L. Kleinman and D. M. Bylander. Efficacious form for model pseudopotentials. *Phys. Rev. Lett.*, 48:1425–1428, May 1982.
- [82] G. Henkelman. *Methods for Calculating Rates of Transitions with Application to Catalysis and Crystal Growth (Doctoral dissertation)*. University of Washington, 2001.
- [83] J. Baker. An Algorithm for the Location of Transition States. *J. Comput. Chem.*, 7:385, 1986.
- [84] H. Taylor and J. Simons. Impositton of Geometrical Constraints on Potential Energy Surface Walking Procedures. *J. Phys. Chem.*, 89:684, 1985.

- [85] C. J. Cerjan and W. H. Miller. On finding transition states. *J. Chem. Phys.*, 75:2800, 1981.
- [86] D. T. Nguyen and D. A. Case. On finding stationary states on large-molecule potential energy surfaces. *J. Phys. Chem.*, 89:4020, 1985.
- [87] W. Quapp. A gradient-only algorithm for tracing a reaction path uphill to the saddle of a potential energy surface. *Chem. Phys. Lett.*, 253:286, 1996.
- [88] S. Fischer and M. Karplus. Conjugate peak refinement: an algorithm for finding reaction paths and accurate transition states in systems with many degrees of freedom. *Chem. Phys. Lett.*, 194:252, 1992.
- [89] I. V. Ionova and E. A. Carter. Ridge method for finding saddle points on potential energy surfaces. *J. Chem. Phys.*, 98:6377, 1993.
- [90] G. H. Vineyard. Frequency factors and isotope effects in solid state rate processes. *J. Phys. Chem. Solids*, 3:121, 1957.
- [91] M. McKee and M. Page. *in Reviews in Computational Chemistry*. (VCH, New York, 1993), Vol. IV, 1993.
- [92] H. Jónsson, G. Mills, and K. W. Jacobsen. *in Classical and Quantum Dynamics in Condensed Phase Simulations*. World Scientific, Singapore, 1998.
- [93] A. Heyden, A. T. Bell, and F. J. Keil. Efficient methods for finding transition states in chemical reactions: Comparison of improved dimer method and partitioned rational function optimization method. *J. Chem. Phys.*, 123:224101, 2005.
- [94] G. Henkelman and H. Jónsson. Improved tangent estimate in the nudged elastic band method for finding minimum energy paths and saddle points. *J. Chem. Phys.*, 113:9978, 2000.
- [95] J. Hutter, M. Iannuzzi, F. Schiffmann, and J. Vandevondele. Cp2k: Atomistic simulations of condensed matter systems. *Wiley Interdisciplinary Reviews: Computational Molecular Science*, 4(1):15–25, 2014.
- [96] C. Grossmann, H. G. Roos, and M. Styne. pages XII, 596. Springer-Verlag Berlin Heidelberg, 2007.

- [97] A. Derevianko, E. Luc-Koenig, and F. Masnou-Seeuws. Application of b-splines in determining the eigenspectrum of diatomic molecules: Robust numerical description of halo-state and feshbach molecules. *Can. J. Phys.*, 87:67–74, 2009.
- [98] C. C. Marston and G. G. Balint-Kurti. The fourier grid hamiltonian method for bound state eigenvalues and eigenfunctions. *J. Chem. Phys.*, 91:3571–3576, 1989.
- [99] W. H. Press, S. A. Teukolsky, W. T. Vetterling, and B. P. Flannery. Cambridge University Press, 2007.
- [100] F. Y. Hajj. Eigenvalues of any parameter in the schrödinger radial equation. *Journal of Physics B: Atomic and Molecular Physics*, 13(23):4521, 1980.
- [101] F. Y. Hajj. Eigenvalues of the two-dimensional schrödinger equation. *Journal of Physics B: Atomic and Molecular Physics*, 15(5):683, 1982.
- [102] F. Y. Hajj. Solution of the schrödinger equation in two and three dimensions. *Journal of Physics B: Atomic and Molecular Physics*, 18(1):1, 1985.
- [103] Exponential-fitting methods for the numerical solution of the schrödinger equation.
- [104] H. D. Meyer, J. Vanthournout, G. V. Berghe, and A. Vanderbauwhede. On the error estimation for a mixed type of interpolation. *Journal of Computational and Applied Mathematics*, 32(3):407 – 415, 1990.
- [105] T. E. Oliphant. Python for Scientific Computing. *Comput. Sci. Eng.*, 9:10, 2007.
- [106] K. J. Millman and M. Aivazis. Python for Scientists and Engineers. *Comput. Sci. Eng.*, 13:9–12, 2011.
- [107] R. E. Langer. On the connection formulas and the solutions of the wave equation. *Phys. Rev.*, 51:669, 1937.
- [108] L.F. Canto and M.S. Hussein. *Scattering Theory of Molecules, Atoms and Nuclei*. World Scientific, 2013.

- [109] R. Wiesendanger. *Scanning Probe Microscopy and Spectroscopy: Methods and Applications*. Cambridge University Press, 1994.
- [110] Z. Cao and Y. Cheng. *Advances in One-Dimensional Wave Mechanics*. Springer-Verlag Berlin Heidelberg, 2014.
- [111] M. F. Herbst. *Instanton calculations of tunnelling in water clusters (Master dissertation)*. Girton College, University of Cambridge, 2013.
- [112] P. R. Bunker and P. Jensen. *Molecular Symmetry and Spectroscopy*. 2nd ed. (NRC Research Press, Ottawa), 2006.
- [113] R. M. Dimeo. Visualization and measurement of quantum rotational dynamics. *Am. J. Phys.*, Vol. 71, N(September 2003):885–893, 2003.
- [114] M. Pillai, J. Goglio, and T. G. Walker. Matrix Numerov method for solving Schrödinger’s equation. *Am. J. Phys.*, 80(11):1017–1019, 2012.
- [115] U. Ohms, H. Guth, W. Treutmann, H. Dannöhl, A. Schweig, and G. Heger. Crystal structure and charge density of 4-methylpyridine (C₆H₇N) at 120 K. *J. Chem. Phys.*, 83(1):273, 1985.
- [116] M. Anderson, L. Bosio, J. Brundeaux-Pouille, and R. Fourme. Toluene: crystal and molecular structure of the stable alpha-phase and of the amorphous state. *J. Chim. Phys. Phys. Chim. Biol.*, 74(2):68, 1977.
- [117] M. Prager and A. Heidemann. Rotational Tunneling and Neutron Spectroscopy: A Compilation. *Chem. Rev.*, 97(8):2933–2966, 1997.
- [118] J. Baudry. Van der Waals interactions and decrease of the rotational barrier of methyl-sized rotators: A theoretical study. *J. Am. Chem. Soc.*, 128(34):11088–11093, 2006.
- [119] S. Clough, A. Heidemann, A. H. Horsewill, and M. N J Paley. Coupled tunnelling motion of a pair of methyl groups in lithium acetate studied by inelastic neutron scattering. *Z. Phys. B Condensed Matter*, 55(1):1–6, 1984.
- [120] W. Häusler and A. Hüller. Tunneling of coupled methyl groups. *Z. Physik B Condensed Matter*, 59(2):177–182, 1985.

- [121] F. Fillaux, C. J. Carlile, and G. J. Kearley. Inelastic-neutron-scattering study of the sine-Gordon breather interactions in isotopic mixtures of 4-methylpyridine. *Phys. Rev. B.*, 58:11416, 1998.
- [122] K. R. Naqvi and W. B. Brown. The non-crossing rule in molecular quantum mechanics. *Int. J. Quantum Chem.*, 6:9–12, 1972.
- [123] W. D. Heiss and A. L. Sannino. Avoided level crossing and exceptional points. *J. Phys. A: Math. Gen.*, 23:1167, 1990.
- [124] F. M. Francisco. On the crossing of the energy levels of a parameter-dependent quantum-mechanical Hamiltonian. *J. Math. Chem.*, 52:2322–2329, 2014.
- [125] M. Icker, P. Fricke, T. Grell, J. Hollenbach, H. Auer, and S. Berger. Experimental boundaries of the quantum rotor induced polarization (QRIP) in liquid state NMR. *Magn. Reson. Chem.*, 51(12):815–820, 2013.
- [126] C. J. Carlile, S. Clough, A.J. Horsewill, and A. Smith. Observation of a dynamic coupling of methyl groups in 4-methylpyridine. *Chem. Phys.*, 135:437–440, 1989.
- [127] S. Khazaei and D. Sebastiani. Methyl rotor quantum states and the effect of chemical environment in organic crystals: gamma-picoline and toluene. *J. Chem. Phys.*, 145:234506, 2016.
- [128] G. Lippert, J. Hutter, and M. Parrinello. A hybrid Gaussian and plane wave density functional scheme. *Mol. Phys.*, 92:477–487, 1997.
- [129] J. VandeVondele, M. Krack, F. Mohamed, M. Parrinello, T. Chassaing, and J. Hutter. A hybrid Gaussian and plane wave density functional scheme. *Comput. Phys. Communications.*, 167:103–128, 2005.
- [130] A. J. Horsewill. Quantum tunnelling aspects of methyl group rotation studied by NMR. *Prog. Nucl. Magn. Reson. Spectros.*, 35(4):359–389, 1999.
- [131] B. Nicolai, A. Cousson, and F. Fillaux. Interplay of quantum methyl rotation and crystal structure in the lithium acetate dihydrate: neutron diffraction, inelastic neutron scattering and theory. *Chem. Phys.*, 290:101–120, 2003.
- [132] M. J. Davis and E. J. Heller. Semiclassical gaussian basis set method for molecular vibrational wave functions. *J. Chem. Phys.*, 71:3383, 1979.

- [133] Z. Wang and H. Shao. A new kind of discretization scheme for solving a two-dimensional time-independent schrödinger equation. *Comput. Phys. Commun.*, 180:842, 2009.
- [134] G. H. Peslherbe, H. Wang, and W. L. Hase. *Monte Carlo Sampling for Classical Trajectory Simulations*, pages 171–201. John Wiley and Sons, Inc., 2007.
- [135] J. Zheng, Z.-H. Li, A. W. Jasper, D. A. Bonhommeau, R. Valero, R. Meana-Paneda, S. L. Mielke, and D. G. Truhlar. A program for adiabatic and nonadiabatic trajectories. *ANT, version 2016, University of Minnesota, Minneapolis*, 180:842, 2017.
- [136] I. Vainshtein, V. I. Zakharov, V. A. Novikov, and M. A. Shifman. Abc of instantons. *Sov. Phys. Usp.*, 25:195, 1982.

LIST OF FIGURES

3.1	Eigenvalues for a methyl group as a function of the barrier height. . .	49
3.2	Schematic illustration of the first two lowest librational levels and tunnel split.	49
3.3	The approximate exponential dependence of the tunnel splitting on the barrier height.	50
3.4	Barrier height dependence of the first librational transition.	51
3.5	Methyl rotational potential for γ -picoline and toluene from first-principles calculations.	54
3.6	Methyl rotational potential for γ -picoline and toluene from first-principles calculations when the dispersion correction was included. .	54
3.7	The ground state geometrical arrangements of the nearest molecule(s) to the probe molecule in γ -picoline and toluene.	55
3.8	Charge density differences for crystal structures of γ -picoline and toluene	56
3.9	Geometrical arrangements of the molecules around the probe γ -picoline molecule.	57
3.10	Geometrical arrangements of the molecules around the probe toluene molecule.	57
3.11	Decomposition of rotational barrier for γ -picoline into sets of inter- and intra-molecular interactions.	58
3.12	Decomposition of rotational barrier for toluene into sets of inter- and intra-molecular interactions.	59
3.13	Calculated 2D potential energy surfaces of rotor-rotor couplings for a dimer of γ -picoline, and toluene.	61
3.14	Calculated 2D potential energy surfaces of rotor-rotor couplings for a dimer of γ -picoline, and toluene when the dispersion correction is included.	61
3.15	The calculated fitted 2D rotational potential for a dimer of γ -picoline.	62
3.16	A comparison of the minimum energy potential path obtained from fitting to the model potential and crystal structure.	64

3.17	A comparison of the minimum energy potential path obtained from fitting to the model potential and crystal structure when dispersion correction was included.	64
4.1	The energy levels of two completely uncoupled free rotors.	68
4.2	Dependence of the lowest lying energy eigenvalues of the two uncoupled methyl groups on the strength of single rotor barrier height. . .	69
4.3	Dependence of the lowest lying energy eigenvalues of the two coupled methyl groups on the coupling strength.	70
4.4	Dependence of the lowest lying energy eigenvalues of the two coupled methyl groups on the coupling strength in different single rotor potentials.	71
4.5	Dependence of tunnel splitting of two coupled methyl groups on coupling strength and single particle potential strength.	73
4.6	Unit cell of γ -picoline.	74
4.7	2D potential energy surface for two face-to-face methyl groups in γ -picoline crystal obtained by DFT calculation. The dispersion correction is included.	75
4.8	Energy-level diagram and calculated tunneling transitions of γ -picoline crystal.	76
4.9	Minimum energy potential path along the lowest potential barrier of a pair of γ -picoline molecules in crystal.	77
4.10	Landscape view and projected map of the calculated proton density distribution in rotational plane of methyl protons of γ -picoline crystal.	78
A.1	Two examples of one-dimensional rotational potentials.	98
A.2	The ground state tunnel splitting and the librational energy over a broad range of barrier height in a potential of general shape. The phase angle is set to zero.	99
A.3	The ground state tunnel splitting and the librational energy over a broad range of barrier height in a potential of general shape. The phase angle is set to π	100
C.1	Dependence of the lowest lying energy eigenvalues of two coupled methyl groups on the coupling strength in different single rotor potentials, obtained by solving the Hamiltonian (C.4) numerically.	109

D.1	The momentum variation of nitrogen along the tunneling direction in the umbrella inversion of Ammonia.	111
D.2	The coordinate variation of nitrogen along tunneling direction in the umbrella inversion of Ammonia.	112
D.3	The distance of nitrogen from the hydrogen plane.	112
D.4	Variation of accumulated tunneling amplitude for Ammonia.	113
E.1	Pathway plots for one-dimensional double well potential with various number of beads.	119

LIST OF TABLES

3.1	Experimental and calculated tunnel splittings for γ -picoline and toluene.	53
3.2	Binding energy of molecules in molecular crystals of γ -picoline and toluene.	53
3.3	Fitted parameters of the model potential to the 2D potential energy surface of a dimer of γ -picoline molecules.	63
3.4	Experimental and calculated tunnel splittings for γ -picoline when the coupling effect is taken into account.	63
4.1	Fitted parameters through mapping of model potential to the computed 2D DFT-PES for two face-to-face methyl groups in γ -picoline.	77
C.1	A comparison between the calculated eigenvalues [per rotational constant which is 0.5] for a harmonic oscillator obtained through the in-house code and those reported in Ref. ³⁵	105
C.2	A comparison between the eigenvalues of the Henon-Heiles potential obtained through the in-house code and those reported in Refs. ^{35,132,133}	106
C.3	A comparison between the calculated eigenvalues [per rotational constant $B = 0.5$] for the two uncoupled free rotors obtained through the in-house code and those reported in Ref. ¹¹⁹	107
E.1	Kink actions S_{kink} in reduced units for one-dimensional quartic-well system.	117
E.2	Determinant ratios corresponding to the kink actions for one-dimensional quartic-well system.	118
E.3	Convergence of the tunneling splitting for one-dimensional quartic-well system.	118
E.4	Comparison of the instanton tunneling splittings in reduced units with the exact quantum splittings for one-dimensional quartic-well system.	120
E.5	Convergence of the tunneling splitting from Ring-Polymer instanton method for the one-dimensional three-fold cosine potential.	122
E.6	Comparison of the instanton tunneling splittings in reduced units with the exact quantum splittings for different barrier heights	123

APPENDIX A

METHYL ROTOR IN A ONE-DIMENSIONAL POTENTIAL OF GENERAL SHAPE

The Hamiltonian for the rotational potential of general shape is defined as,

$$H = -\frac{\hbar^2}{2I} \frac{\partial^2}{\partial \phi^2} + \frac{V_3}{2} [1 + (-1)^k \cos 3\phi] + \frac{V_6}{2} [1 + (-1)^k \cos 6\phi] \quad (\text{A.1})$$

Three independent variables k , VS, and δ are used to define the shape of potential in the following way:

1 - $k = 0$ or $k = 1$ stand for phase angles $\alpha = \pi$, and $\alpha = 0$, respectively. The first case ($\alpha = 0$) describes potentials with broad barriers and shallow minima while the second case ($\alpha = \pi$) gives potentials with broad minima and narrow barriers.

2 - $\text{VS} = |V_3| + |V_6|$ is a measure of the potential strength.

3 - $\delta = V_3/\text{VS}$ determines the shape of potential. It characterizes the contribution of a pure $\cos(3\phi)$ potential.

The ground state tunnel splitting E_{tunnel} and the first librational excitation E_{01} are calculated by numerical diagonalization of Eq. (A.1). Fig A.1(a) and A.1(b) show two examples of potentials with different values of the parameters, described above. In Fig A.1(a) three fold potential is dominated whereas in Fig A.1(b) six fold one. Figures A.2 and A.3 show the calculated ground state tunnel splitting and librational energies over a broad range of the parameters for the potential function. These plots allow the experimentalists to interpret their measured data within the single particle model. The librational energy is defined as $E_{01} = (E_3 + E_2)/2 - (E_1 + E_0)/2$. The obtained results are in agreement with the study of Prager et al.¹¹⁷

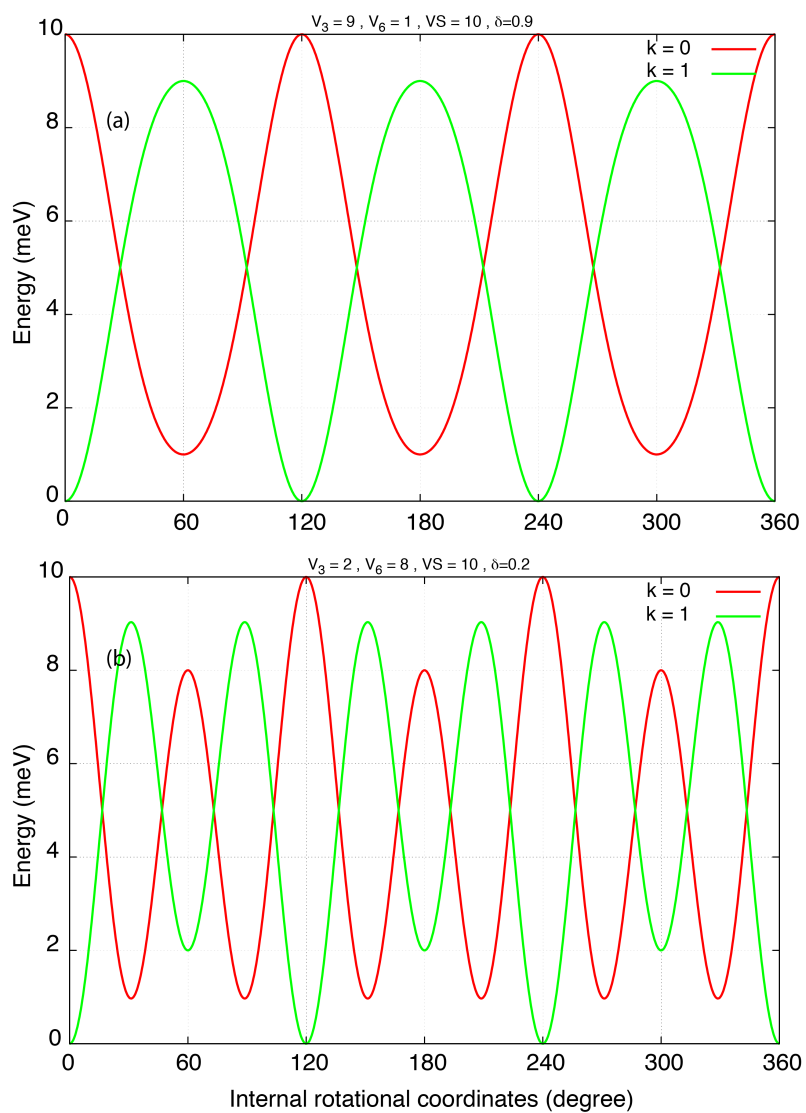


Figure A.1: Two examples of one-dimensional rotational potentials with fixed parameters (a) $V_3 = 9, V_6 = 1$, and (b) $V_3 = 2, V_6 = 8$; for $k = 0$ and $k = 1$.

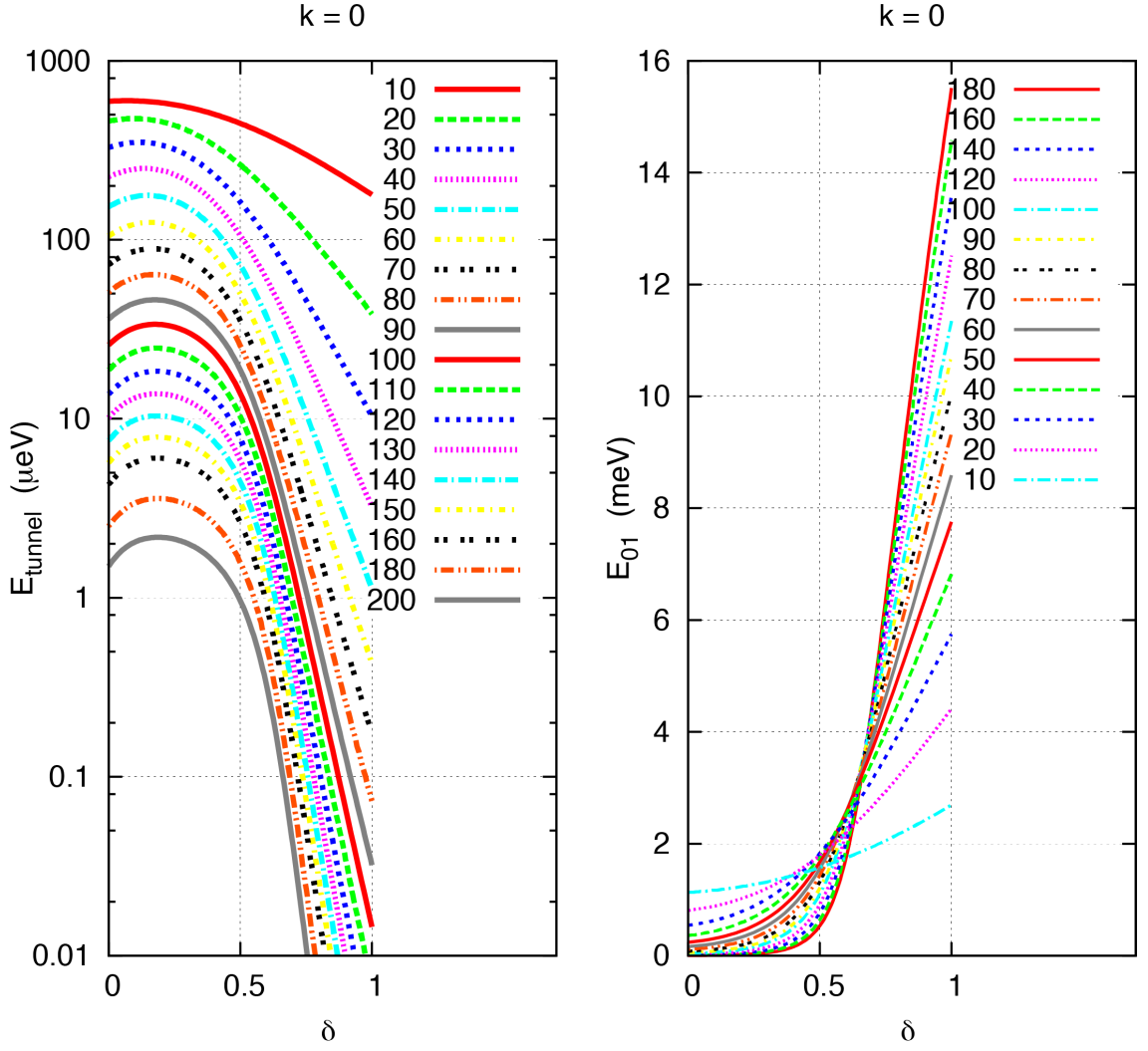


Figure A.2: The ground state tunnel splitting (the energy difference between the two lowest eigenvalues) and the librational energies E_{01} (the energy difference between the averaged energies of the two lowest and a following pairs of levels) in a potential of general shape with $k = 0$. V_3 and V_6 are taken ≥ 0 .

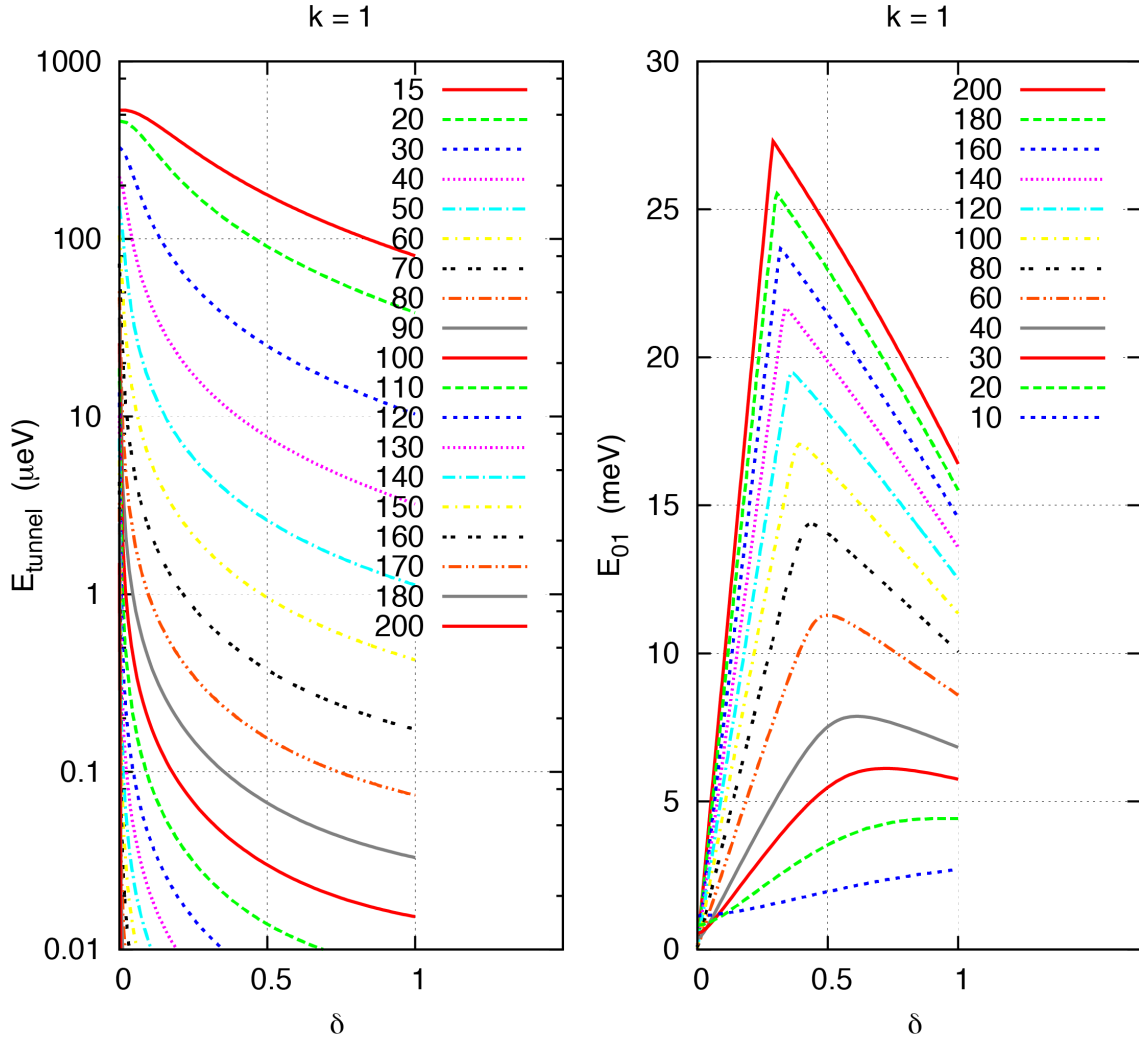


Figure A.3: The ground state tunnel splitting (energy difference between the two lowest eigenvalues) and the librational energies E_{01} (energy difference between the averaged energies of the two lowest and a following pairs of levels) in a potential of general shapes with $k = 1$. V_3 and V_6 are taken ≥ 0 .

APPENDIX B

ANALYTICAL SOLUTION TO THE COUPLED-PAIR MODEL HAMILTONIAN

The Schrödinger equation is solved for the two coupled rotors in a hindered periodic potential,

$$\mathcal{H} = -B\left(\frac{\partial^2}{\partial\phi_1^2} + \frac{\partial^2}{\partial\phi_2^2}\right) + V_3(\cos 3\phi_1 + \cos 3\phi_2) + W_3\cos 3(\phi_1 - \phi_2) \quad (\text{B.1})$$

by expanding the wave function on the basis set of two independent free rotor functions. A general solution for the coupled-pair Hamiltonian Eq. (B.1) is derived, which can be easily modified to get the energy spectrum of two free rotors, two uncoupled rotors in hindered potentials, and one single rotor in hindered potential.

The solution of the Hamiltonian (B.1) has the periodicity of 2π -periodic with respect to the variables ϕ_1 and ϕ_2 , the same as in the single rotor problem. The wave functions can be expanded in terms of the free rotor states, which is the same as an expansion into a double Fourier series:

$$|\psi\rangle = \sum_{m=-\infty}^{+\infty} \sum_{n=-\infty}^{+\infty} a_{m,n} |m, n\rangle \quad (\text{B.2})$$

where

$$a_{m,n} = \frac{1}{2\pi} \int_0^{2\pi} \int_0^{2\pi} d\phi_1 d\phi_2 \psi(\phi_1, \phi_2) e^{-im\phi_1} e^{-in\phi_2} \quad (\text{B.3})$$

is the Fourier coefficients of $\psi(\phi_1, \phi_2)$. Because of the periodicity of the wavefunction, the 2D Fourier space is infinite but discrete, i.e: $n, m = (\dots, -1, 0, 1, \dots)$. In Eq. (B.2), $|m, n\rangle = |m\rangle \otimes |n\rangle$. The ket notations $|m\rangle$ and $|n\rangle$ are used to represent the plane-wave functions:

$$\langle \phi_1 | m \rangle = \frac{1}{\sqrt{2\pi}} e^{im\phi_1} \quad \text{and} \quad \langle \phi_2 | n \rangle = \frac{1}{\sqrt{2\pi}} e^{in\phi_2} \quad (\text{B.4})$$

The Schrödinger equation $(\mathcal{H} - E)|\psi\rangle = 0$ with the Hamiltonian defined in Eq.

(B.1) is solved by the Ansatz, Eq. (B.2), gives:

$$\begin{aligned} \frac{1}{2\pi} \sum_{m=-\infty}^{+\infty} \sum_{n=-\infty}^{+\infty} e^{im\phi_1} e^{in\phi_2} \times \left\{ \right. & [B(n^2 + m^2) - E] a_{m,n} \\ & + \frac{V_3}{2} (a_{m+3,n} + a_{m-3,n}) \\ & + \frac{V_3}{2} (a_{m,n+3} + a_{m,n-3}) \\ & \left. + \frac{W_3}{2} (a_{m-3,n+3} + a_{m+3,n-3}) \right\} = 0 \end{aligned} \quad (\text{B.5})$$

where for the cosine potentials, the relation $\cos(\alpha) = (e^{i\alpha} + e^{-\alpha})/2$ is used. The only solution to the Eq. (B.5) is that the terms in bracket for every m and n to be zero. This means:

$$\begin{aligned} & B n^2 a_{m,n} + \frac{V_3}{2} (a_{m+3,n} + a_{m-3,n}) \\ & + B m^2 a_{m,n} + \frac{V_3}{2} (a_{m,n+3} + a_{m,n-3}) \\ & + \frac{W_3}{2} (a_{m-3,n+3} + a_{m+3,n-3}) \\ & = E a_{m,n} \end{aligned} \quad (\text{B.6})$$

This leaves us with $(2K + 1)^2$ inhomogeneous equations for $(2K + 1)^2$ coefficients $a_{m,n}$; when the infinite system is truncated to $-K \leq m, n \leq K$. The Eq. (B.6) can be transformed into a more compact form $\mathbb{M}\mathbb{A} = E\mathbb{A}$, using a matrix representation $\mathbb{A} \equiv ((a_{m,n}))$ and matrix \mathbb{M} :

$$\begin{aligned} \mathbb{M} = & \left[B \mathbb{C} + \frac{V_3}{2} (\mathbb{I}_{+3} + \mathbb{I}_{-3}) \right] \otimes \mathbb{I}_0 \\ & + \mathbb{I}_0 \otimes \left[B \mathbb{C} + \frac{V_3}{2} (\mathbb{I}_{+3} + \mathbb{I}_{-3}) \right] \\ & + \frac{W_3}{2} (\mathbb{I}_{-3} \otimes \mathbb{I}_{+3} + \mathbb{I}_{+3} \otimes \mathbb{I}_{-3}) \end{aligned} \quad (\text{B.7})$$

where \mathbb{I}_p is a matrix of 1s along the p th diagonal, and zeros elsewhere. The diagonal matrix \mathbb{C} represents the kinetic term. The dimension of \mathbb{I}_p matrices is $(2K + 1) \times (2K + 1)$ and accordingly the dimension of \mathbb{M} matrix is $(2K + 1)^2 \times (2K + 1)^2$. To evaluate the eigenvalues and eigenfunctions, the \mathbb{M} matrix is diagonalized using the Lanczos algorithm for the sparse matrices, implemented in Python code. One can compute the energy spectrum of two free-rotors or two uncoupled-rotors in hindered potentials by excluding the corresponding relevant matrices from Eq. (B.7). Clearly, for the eigenvalue problem of one single free rotor or a single rotor in hindered potential, the total number of computed eigenvalues is $(2K + 1)$, i.e. the tensor

multiplying by identity matrix has to be ignored. In Eq. (B.8) to (B.11), the essential matrices for constructing Matrix elements of \mathbb{M} are given.

$$\mathbb{C} = \begin{pmatrix} \boxed{(-K)^2} & 0 & 0 & \dots & 0 \\ 0 & \boxed{(-K+1)^2} & 0 & \dots & 0 \\ 0 & 0 & \boxed{(-K+2)^2} & \dots & 0 \\ \vdots & \vdots & \vdots & \ddots & \vdots \\ 0 & 0 & 0 & \dots & \boxed{(K)^2} \end{pmatrix}_{(2K+1) \times (2K+1)} \quad (\text{B.8})$$

$$\mathbb{I}_{+3} = \begin{pmatrix} 0 & 0 & 0 & \boxed{1} & 0 & 0 & \dots & 0 \\ 0 & 0 & 0 & 0 & \boxed{1} & 0 & \dots & 0 \\ 0 & 0 & 0 & 0 & 0 & \boxed{1} & \dots & 0 \\ \vdots & \vdots & \vdots & \vdots & \vdots & \vdots & \ddots & \vdots \\ 0 & 0 & 0 & 0 & 0 & 0 & \dots & \boxed{1} \\ 0 & 0 & 0 & 0 & 0 & 0 & \dots & 0 \\ 0 & 0 & 0 & 0 & 0 & 0 & \dots & 0 \\ 0 & 0 & 0 & 0 & 0 & 0 & \dots & 0 \end{pmatrix}_{(2K+1) \times (2K+1)} \quad (\text{B.9})$$

$$\mathbb{I}_{-3} = \begin{pmatrix} 0 & 0 & 0 & \dots & 0 & 0 & 0 & 0 \\ 0 & 0 & 0 & \dots & 0 & 0 & 0 & 0 \\ 0 & 0 & 0 & \dots & 0 & 0 & 0 & 0 \\ \boxed{1} & 0 & 0 & \dots & 0 & 0 & 0 & 0 \\ 0 & \boxed{1} & 0 & \dots & 0 & 0 & 0 & 0 \\ 0 & 0 & \boxed{1} & \dots & 0 & 0 & 0 & 0 \\ \vdots & \vdots & \vdots & \ddots & \vdots & \vdots & \vdots & \vdots \\ 0 & 0 & 0 & \dots & \boxed{1} & 0 & 0 & 0 \end{pmatrix}_{(2K+1) \times (2K+1)} \quad (\text{B.10})$$

$$\mathbb{I}_0 = \begin{pmatrix} \boxed{1} & 0 & 0 & \dots & 0 \\ 0 & \boxed{1} & 0 & \dots & 0 \\ 0 & 0 & \boxed{1} & \dots & 0 \\ \vdots & \vdots & \vdots & \ddots & \vdots \\ 0 & 0 & 0 & \dots & \boxed{1} \end{pmatrix}_{(2K+1) \times (2K+1)} \quad (\text{B.11})$$

APPENDIX C

NUMERICAL TESTS OF THE TWO DIMENSIONAL CODE

The Numerov-type method is applied for the calculation of the eigenvalues of the two-dimensional harmonic oscillator, the Henon-Heiles potential, and two uncoupled free rotors. The obtained results through the in-house developed python code are compared with those produced using the full discretization technique given in the literature. Furthermore, the numerical results of the eigenvalue dependency on the coupling strength for the coupled-pair model of potential described in section 4.1 are given in the last part.

TWO-DIMENSIONAL HARMONIC OSCILLATOR

Two-dimensional harmonic oscillator Hamiltonian is defined as

$$\mathcal{H} = -\frac{1}{2} \frac{\partial^2}{\partial x^2} - \frac{1}{2} \frac{\partial^2}{\partial y^2} + \frac{1}{2}(x^2 + y^2) \quad (\text{C.1})$$

The exact eigenvalues of the above Hamiltonian are given by $E_n = n + 1$, $n = n_x + n_y$ where $n_x, n_y = 0, 1, 2, 3, \dots$ Table C.1 shows the results obtained through the in-house code, which are compared with those reported by Kalogiratou et al.,³⁵

Table C.1: A comparison between the calculated eigenvalues [per rotational constant which is 0.5] for a harmonic oscillator obtained through the in-house code and those reported in Ref.³⁵

E_n	E_n [this work]	E_n ³⁵	E_n [exact]	n_x	n_y
E_0	0.9996869	0.999687	1.0	0	0
E_1	1.9996845	1.999685	2.0	0	1
E_1	1.9984353	-	2.0	1	0
E_2	2.9959302	2.999678	3.0	0	2
E_2	2.9984329	-	3.0	2	0
E_2	2.9996775	-	3.0	1	1
E_3	3.9921692	3.999663	4.0	0	3
E_3	3.9959278	-	4.0	3	0
E_3	3.9984259	-	4.0	1	2
E_3	3.9996626	-	4.0	2	1
E_4	4.9871500	4.999637	5.0	0	4
E_4	4.9921668	-	5.0	4	0
E_4	4.9959208	-	5.0	1	3
E_4	4.9984110	-	5.0	3	1
E_4	4.9996369	-	5.0	2	2

TWO-DIMENSIONAL HENON-HEILES POTENTIAL

Two-dimensional Henon-Heiles Hamiltonian is defined as

$$\mathcal{H} = -\frac{1}{2} \frac{\partial^2}{\partial x^2} - \frac{1}{2} \frac{\partial^2}{\partial y^2} + \frac{1}{2}(x^2 + y^2) + (0.0125)^{1/2}(x^2 y - \frac{y^3}{3}) \quad (\text{C.2})$$

Table C.2 shows the results of the calculated eigenvalues for the Henon-Heiles Hamiltonian obtained through the in-house code, which are compared with those reported in Refs.^{35,132,133}

Table C.2: A comparison between the eigenvalues of the Henon-Heiles potential obtained through the in-house code and those reported in Refs.^{35,132,133}

E_n	E_n [this work]	E_n^{35}	E_n^{132}	E_n^{133}
E_0	0.99828234	0.9986	0.9986	0.99859477
E_2	1.98854812	1.9901	1.9901	1.99007676
E_3	1.98975597	-	-	1.99007676
E_4	2.95405925	2.9562	2.9562	2.95624298
E_5	2.98327253	2.9853	2.9853	2.98532642
E_6	2.98377955	-	-	2.98532642
E_7	3.92005535	3.9259	3.9260	3.92596372
E_8	3.9247260	3.9822	3.9824	3.92596372
E_9	3.97939347	3.9856	3.9858	3.9824172
E_{10}	3.98269488	-	-	3.98576092
E_{11}	4.86392434	4.8700	4.8701	4.87014400
E_{12}	4.89307373	4.8986	4.8986	4.89864420
E_{13}	4.8944664	4.9860	4.9863	4.89864420
E_{14}	4.98137535	-	-	4.98625101
E_{15}	4.98185088	-	-	4.98625101

TWO UNCOUPLED FREE ROTORS

The Hamiltonian for the two uncoupled free rotors is defined as

$$\mathcal{H} = -B \frac{\partial^2}{\partial \phi_1^2} - B \frac{\partial^2}{\partial \phi_2^2} \quad (\text{C.3})$$

where $B = \hbar^2/2I = 654\mu\text{eV}$ is the rotational constant. Table C.3 shows the results of the calculated eigenvalues for the above Hamiltonian, which are compared with those reported in Ref.¹¹⁹

Table C.3: A comparison between the calculated eigenvalues [per rotational constant $B = 0.5$] for the two uncoupled free rotors obtained through the in-house code and those reported in Ref.¹¹⁹

E_n	E [this work]	E [exact] ¹¹⁹
E_0	0.0	0.0
E_1	0.991963	1.0
E_1	0.991963	1.0
E_1	0.992015	1.0
E_1	0.992016	1.0
E_2	1.983979	2.0
E_2	1.983979	2.0
E_2	1.983979	2.0
E_2	1.983979	2.0

NUMERICAL SOLUTION TO THE 2D COUPLED-PAIR MODEL HAMILTONIAN

The Hamiltonian for two coupled methyl rotors is defined as

$$\mathcal{H} = -B \frac{\partial^2}{\partial \phi_1^2} - B \frac{\partial^2}{\partial \phi_2^2} + V_3 \cos 3\phi_1 + V_3 \cos 3\phi_2 + W_3 \cos(3\phi_1 - 3\phi_2) \quad (\text{C.4})$$

where $B = \hbar^2/2I = 654\mu\text{eV}$ is the rotational constant. Figure C.1 shows the dependence of the lowest energy eigenvalues as function of the coupling strength W_3 at various single particle potential strength of V_3 in meV. The results are obtained by solving the above Hamiltonian numerically.

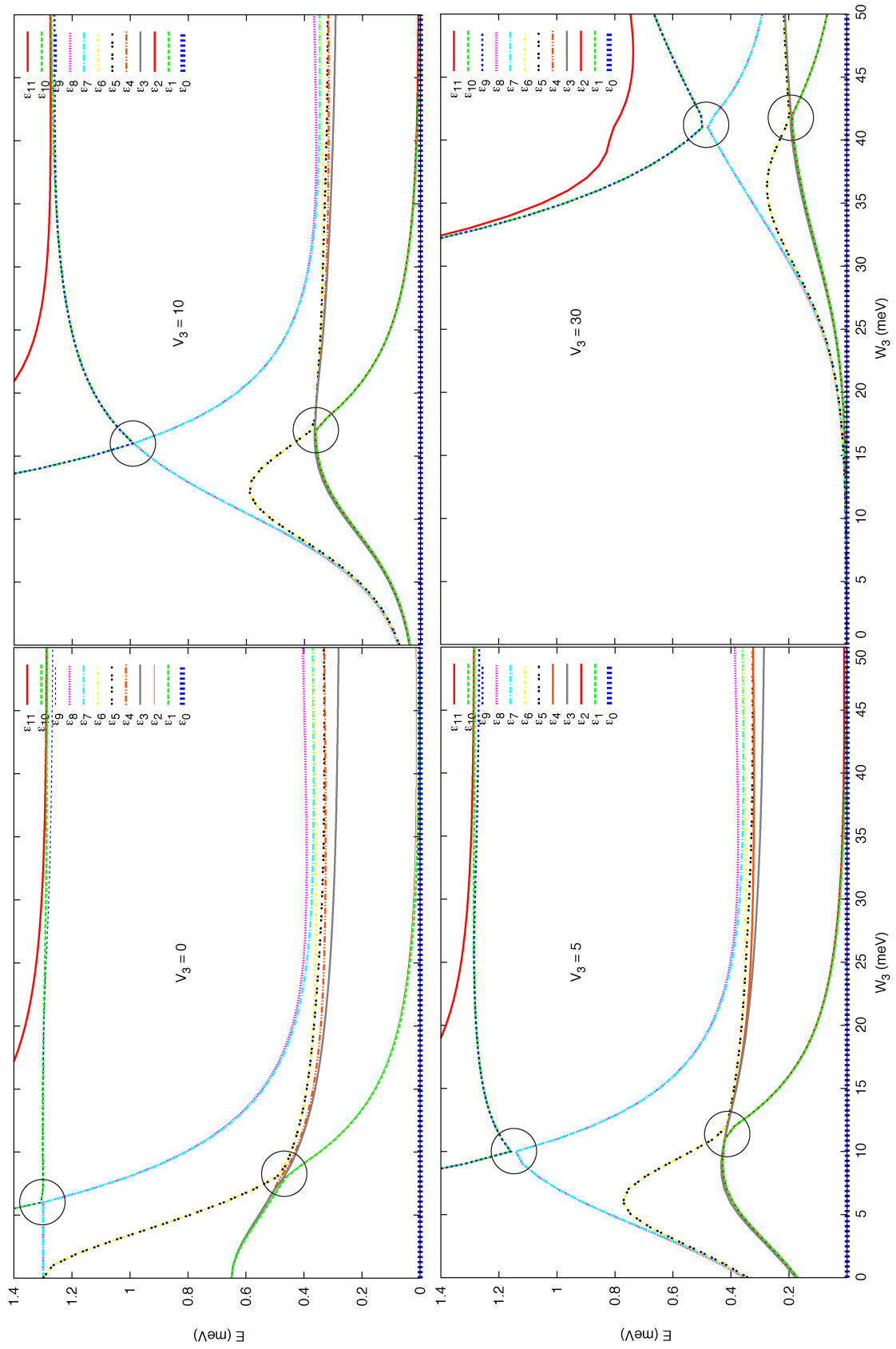


Figure C.1: Dependence of the lowest lying energy eigenvalues of two coupled methyl groups on the coupling strength in different single rotor potentials, obtained by solving the Hamiltonian (C.4) numerically.

APPENDIX D

NUMERICAL IMPLEMENTATION OF THE AIMD APPROACH COMBINED WITH THE SEMICLASSICAL METHOD

Based on the ab-initio molecular dynamics approach combined with the semiclassical method of Makri-Miller,¹⁹ described in section 2.2, several in-house Fortran codes are developed which combined with the CP2K program⁹⁵ to reproduce the results for the tunnel splitting of the umbrella inversion of Ammonia given in the Ref.¹⁸ In the following, the details of the calculations are described.

APPLICATION TO THE UMBRELLA INVERSION OF AMMONIA

Ammonia is the simplest molecule accompanying the quantum tunneling effect. It has a trigonal pyramidal shape with three hydrogen atoms at the base and the nitrogen atom at the top. This system has a double well potential because the nitrogen atom faces a barrier to travels through either side of the plane defined by the hydrogen atoms. The barrier is the result of the Coulomb repulsion between the nitrogen and the three protons. The tunneling of nitrogen through the barrier results in a splitting of the ground state vibrational energy.

Here, a set of standard molecular dynamic (MD) calculations were performed in microcanonical (NVE) ensemble using CP2K program package.⁹⁵ A hybrid Gaussian and Plane-Wave (GPW) basis set with the GTH pseudopotentials^{74,75} were employed, in conjunction with the Becke, Lee, Yang and Parr (BLYP)^{48,51} generalized gradient approximation for the exchange and correlation energy. A 300 Ry energy cut-off was used for the auxiliary basis set of plane waves. A non-periodic box of dimensions $12 \times 12 \times 12$ angstrom with one single molecule was selected. The trajectories are calculated up to 100 fs, with a time step of 0.2 fs. The initial geometries and momentum for ab-initio MD (AIMD) simulations were determined by performing normal mode analysis. The details of initial conditions for the AIMD are given in the next section. In total, 200 trajectories were calculated. The number of trajectories are determined by checking the convergence of the tunneling splitting.

The initial point for calculating tunneling is the determination of the tunneling direction. In the case of the umbrella inversion of Ammonia, the norm of the hydrogen plane is defined as the tunneling direction $\hat{\mathbf{n}}$, the momentum vector of nitrogen as \mathbf{p} , and the coordinate vector of nitrogen as \mathbf{q} . In order to find the turning points, the variation of $\mathbf{p}\cdot\hat{\mathbf{n}}$ for each trajectory is monitored. Fig. D.1 shows the variation of momentum along the tunneling direction. The blue circles highlight the points that $\mathbf{p}\cdot\hat{\mathbf{n}}$ goes to zero. However, the turning points are those in which $\mathbf{q}\cdot\hat{\mathbf{n}}$ goes through a relative maximum. Fig. D.2 shows the variation of coordinate along the tunneling direction and the blue circles show the relative maximums. Therefore, three classical turning points are detected, which correspond to the time that the nitrogen gets very close to the hydrogen plane, however as it classically cannot go through the barrier of hydrogen plane, it is then reflected. Fig. D.3 shows the distance of nitrogen from the hydrogen plane for each molecular dynamics step. As it can be seen, the turning points are those that nitrogen has the minimum distance from the hydrogen plane. This analysis for each trajectory has to be repeated to find the turning points.

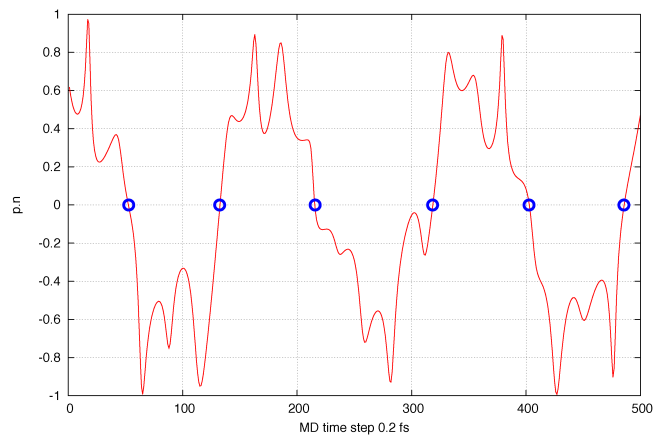


Figure D.1: The momentum variation of nitrogen along the tunneling direction in the umbrella inversion of Ammonia for each molecular dynamics step. The blue circles show the points that $\mathbf{p}\cdot\hat{\mathbf{n}}$ goes through zero.

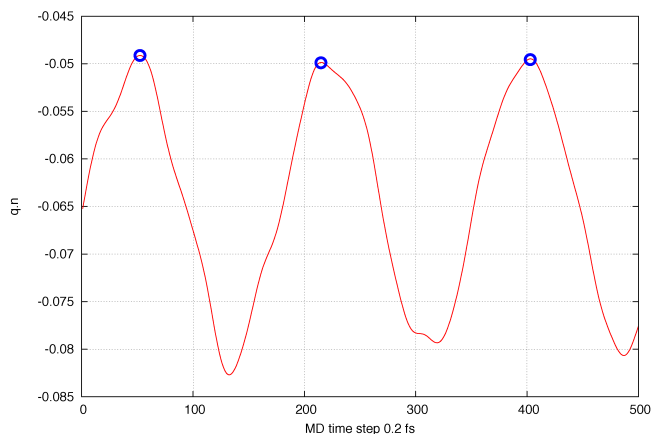


Figure D.2: The coordinate variation of the nitrogen along the tunneling direction in the umbrella inversion of Ammonia for each molecular dynamics step. The blue circles show the points that $\mathbf{q} \cdot \hat{\mathbf{n}}$ goes through the relative maximum.

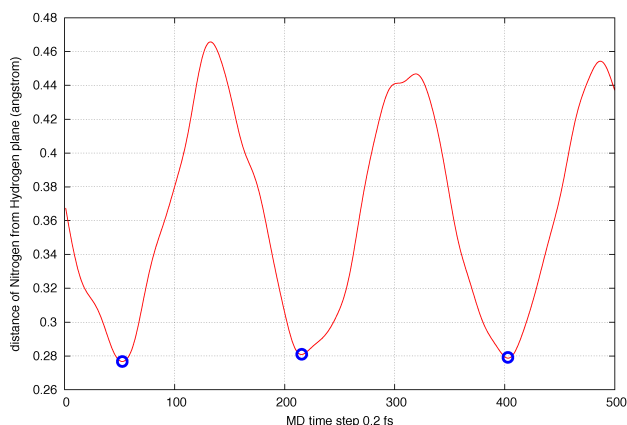


Figure D.3: The distance of nitrogen from the hydrogen plane for each molecular dynamics step. The blue circles show the points that nitrogen has the minimum distance from the hydrogen plane.

Once the turning points were detected, the terminal point of the tunneling path is determined by taking the mirror reflection of the structure with respect to the hydrogen plane. For determination of tunneling path, 18 middle structures are created between the initial and the terminal structure, by moving the nitrogen towards the hydrogen plane and adjusting NH bond length to the value at the initial structure. The potential energy of each structure along the tunneling path is then obtained by performing single point calculations. The smooth potential energy curve $V(\xi)$ is generated by interpolating technique based on the calculated energies of 20 grids

along the tunneling path. For each turning point, the tunneling amplitude $\exp(-\theta)$ according to the Eq. (2.117) is calculated. The action integral is calculated numerically with quadrature by parts. The accumulated tunneling amplitude is averaged over 200 trajectories, shown in Fig. D.4. Using the Eq. (2.119), the tunneling splitting ΔE is calculated accordingly.

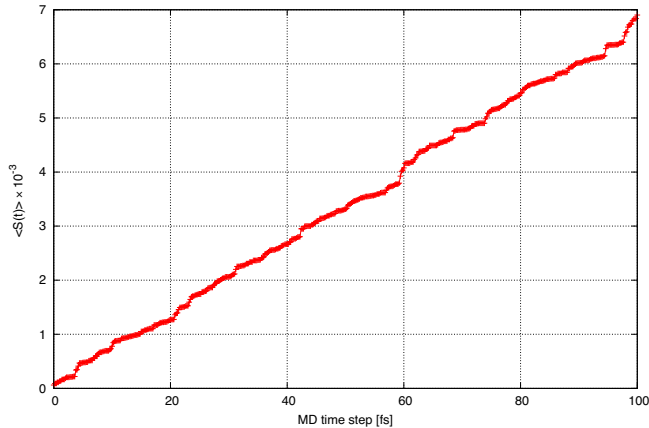


Figure D.4: Variation of accumulated tunneling amplitude averaged over 200 trajectories for Ammonia.

DETAILS OF NORMAL-MODE SAMPLING

The Hamiltonian for a system of n normal modes is the sum of energies for the separable harmonic oscillators and is given by

$$H = E = \sum_{i=1}^n E_i = \sum_{i=1}^n \frac{P_i^2 + \omega_i^2 Q_i^2}{2} \quad (\text{D.1})$$

To form a microcanonical ensemble, random values for the P_i and Q_i are chosen so that there is a uniform distribution in the classical phase space of $H(P, Q)$. For the method called microcanonical normal-mode sampling, random values are chosen for the mode energies E_i , which are then transformed to the random values for P_i and Q_i .¹³⁴ To accomplish this, an in-house Fortran code is developed which is combined with the ab-initio MD CP2K code to create the initial geometries and momentum of Ammonia molecule for the ab-initio molecular dynamics.

The Boltzmann-like distribution of vibrational quantum numbers is determined by taking the following steps based on the Adiabatic and Non-adiabatic Trajectories (ANT) program.¹³⁵ The ANT manual is used as guidance for the implementation of the code.

(i) Normal mode analysis is performed to obtain vibrational frequencies and normal mode coordinates. The basic idea behind normal mode analysis is that the potential energy function V can be expressed in terms of a Taylor expansion about any of local minima in terms of the mass-weighted coordinates $q_i = \sqrt{m_i}x_i$, where x_i is the displacement of the i th coordinate from the energy minimum and m_i is that mass of the corresponding atom. To second-order approximation, the Taylor series expansion of V is,

$$V = \frac{1}{2} \sum_{i,j=1}^{3N} \frac{\partial^2 V}{\partial q_i \partial q_j} q_i q_j \quad (\text{D.2})$$

Therefore, the potential energy surface is approximated by the so-called harmonic potential, which is characterized by the second derivatives, *i.e.*, the force constants, evaluated at the minimum energy. It is assumed that the fluctuations still occur within this parabolic energy surface. The second derivatives in Eq. (D.2), can be written in a matrix, the so-called ‘‘Hessian matrix’’. Diagonalization of the Hessian matrix yields to the eigenvalue and eigenvectors implies normal mode frequencies and coordinates, respectively. The CP2K program is used to obtain vibrational frequencies and normal mode coordinates. ω_m are the vibrational frequencies, where $m = 6$ in the case of Ammonia. The mass scaled eigenvectors are stored as \hat{X}_m^{ij} , where j labels atoms, and i labels x, y, z .

(ii) Generate a random number ξ in the range $[0, 1]$.

(iii) Vibrational numbers n_m , for each mode is computed using

$$n_m = -\text{intger}\left(\frac{k_B T \ln(1 - \xi)}{\hbar \omega_m}\right) \quad (\text{D.3})$$

(iv) The last two steps are repeated until $3 \times N - 6$ (N is the number of atoms) vibrational quantum numbers are generated.

The vibrational numbers should be in the range of zero to infinite since $\ln(1 - \xi)$ is between zero to infinite. However, when one randomly samples this region, most of times one gets zero; which is normal because the populations of the vibrational excited states are very small. Once the vibrational quantum numbers are generated, the following steps are taken to generate the initial momenta and position of atoms.

(i) The energy for each mode is computed by

$$E_m = \hbar \omega_m \left(n_m + \frac{1}{2}\right) \quad (\text{D.4})$$

(ii) The turning points are computed from

$$R_m^\pm - R_m^0 = \sqrt{\frac{2E_m}{\omega_m^2 \mu}} \quad (\text{D.5})$$

(iii) Random numbers ξ_m are generated and displacements are made about the minimum energy structure,

$$x^{ij} = x_0^{ij} + \sum_m \hat{X}_m^{ij} (R_m^\pm - R_m^0) \cos(2\pi\xi_m) \quad (\text{D.6})$$

where x_0^{ij} is the initial position of atoms, x^{ij} is the generated position of atoms in cartesian. j labels atoms, and i labels x, y, z . The second term is the mass-weighted coordinates which has to transform back to the unscaled coordinates before to sum up with the initial coordinates of atoms.

(iv) For the initial velocity of atoms, one needs to calculate the kinetic energy of the m th normal mode

$$T_m = E_m - \frac{1}{2} \omega_m^2 \mu [(R_m^\pm - R_m^0) \cos(2\pi\xi)]^2 \quad (\text{D.7})$$

(v) The Velocity is set to

$$\dot{X}_m^{ij} = \sum_m \hat{X}_m^{ij} \sqrt{\frac{2T_m}{\mu}} \quad (\text{D.8})$$

where the sign is randomized for each mode. The mass-weighted velocities transform back to the unscaled velocities.

APPENDIX E

NUMERICAL IMPLEMENTATION OF THE RING-POLYMER METHOD

Based on the Ring-Polymer instanton approach,¹⁷ described in Section 2.3, an in-house Python^{105,106} code is developed to compute the tunnel splitting in the one-dimensional systems. The code is validated by reproducing the results of tunnel splitting for the one-dimensional double well potential given in the Ref.¹⁷ Furthermore, the approach is examined for the one-dimensional three-fold cosine potential of methyl groups.

ONE-DIMENSIONAL DOUBLE WELL POTENTIAL

The one-dimensional double well potential is defined as,

$$V(x) = V_0 \left(\frac{x^2}{x_0^2} - 1 \right)^2 \quad (\text{E.1})$$

where V_0 is the barrier height between two minimas located at $x = \pm x_0$. The initial geometry of beads are made by distributing them evenly between two minimas. The end points of the linear polymer are allowed to be relaxed during the minimization. The limited memory Broyden-Fletcher-Goldfarb-Shanno (L-BFGS) algorithm, implemented in Python code, is used to find the geometry. The single kink action is calculated once the minimum linear polymer geometry is found. Normal mode frequencies are then computed by diagonalizing the Hessian matrix defined in Eq. (2.146). The one-dimensional Schrödinger equation with the potential defined in Eq. (E.1) is numerically solved to obtain the exact quantum states, which is considered as a reference for the comparison.

Tables E.1 and E.2 show the numerical results of the kink action S_{kink} and the determinant ratio Φ with respect to the number of beads M and the imaginary time duration of $\beta\hbar$. As it can be clearly seen, the results along the diagonal of Tables E.1 and E.2 within 3 significant figures are identical because the value of $\beta_M\hbar (= \beta\hbar/M)$ is the same. In the first column of the tables where $\beta\hbar = 15$, the periodic orbits on the inverted potential has insufficient time to connect $\pm x_0$, *i.e.*, the springs between the beads are too stiff to allow a proper sampling of the tunneling path. When the

time duration is sufficiently long, as it can be seen in the second column, one can check for the convergence of the results with respect to the number of beads. At certain number of beads, the results are converged and adding further beads while the time duration is fixed, yields dumping additional beads close to the ends. This can be clearly seen in Fig. E.1, which shows the pathway on the potential energy surface with various number of beads for the fixed imaginary time $\beta\hbar = 30$. Table E.3 gives the tunneling splittings Δ corresponds to the $\beta\hbar = 30$ column of Tables E.1 and E.2. It is seen, the convergence to within 1% is reached by $M = 64$.

Table E.1: Kink actions S_{kink} in reduced units for one-dimensional potential of Eq. (E.1) with $x_0 = 5$ and $V_0 = 1$. The exact path integral version of instanton theory¹³⁶ gives $S_{kink} = 9.428$.

$M/\beta\hbar$	15	30	60	120	240
8	9.4084	8.7639	5.9672	3.4220	1.6551
16	9.3805	9.3358	8.7621	5.9672	3.2420
32	3.16×10^{-10}	9.4057	9.3358	8.7621	5.9672
64	6.82×10^{-10}	9.4225	9.4057	9.3358	8.7621
128	1.58×10^{-9}	9.4267	9.4225	9.4057	9.3358
256	2.71×10^{-9}	9.4277	9.4267	9.4225	9.4057
512	3.30×10^{-9}	9.4280	9.4277	9.4267	9.4225

Table E.2: Determinant ratios Φ corresponding to the kink actions of Table E.1. The exact path integral version of instanton theory¹³⁶ gives $\Phi = 0.510$.

$M/\beta\hbar$	15	30	60	120	240
8	0.4531	0.8717	1.4548	1.6848	1.7467
16	0.5319	0.5997	0.8829	1.4549	1.6848
32	1.7677	0.5329	0.5997	0.8829	1.4549
64	1.7677	0.5161	0.5329	0.5997	0.8829
128	1.7677	0.5117	0.5159	0.5329	0.5997
256	1.7677	0.5108	0.5117	0.5159	0.5329
512	1.7677	0.5105	0.5106	0.5117	0.5159

Table E.3: Convergence of the tunneling splitting Δ in reduced units obtained from the kink actions and determinant in Tables E.1 and E.2 corresponding to $\beta\hbar = 30$. The quantum value is obtained by solving the one-dimensional Schrödinger equation for double well potential.

number of beads	16	32	64	128	256	512	Exact inst ¹³⁶	Quantum
$\Delta \times 10^4$	3.5858	3.7766	3.8380	3.8552	3.8588	3.8601	3.86	3.42

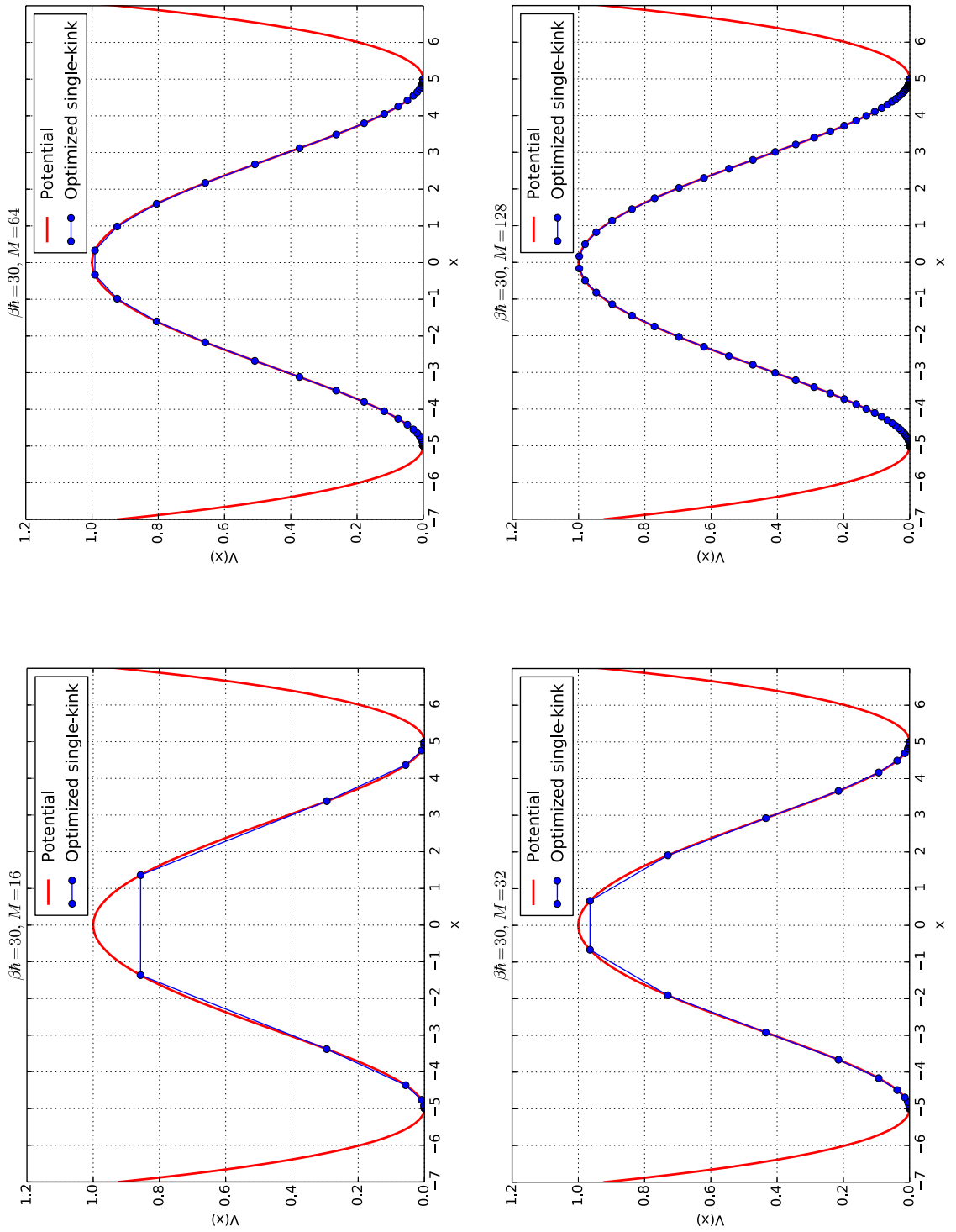


Figure E.1: Pathway plots for the one-dimensional double well potential with various number of beads M for the imaginary time $\beta\hbar = 30$. Adding further beads while $\beta\hbar$ is fixed has only the effect of dumping additional beads close to the ends.

The main source of error within this approach is due to the steepest descent approximation, on which the method is based. However, it does not mean that this approach is a harmonic approach because the anharmonicity is addressed by the kink. More precisely, the anharmonicity along the instanton path is included exactly. In multidimensional systems, the anharmonic fluctuations perpendicular to the instanton path may introduce some error into the results. In one dimensional systems, the main source of error is $\det \mathbf{J}_0$ because it describes the non-tunneling paths by harmonic fluctuations about the minima.¹⁷ The size of this error is investigated by using a series of different values for the barrier height, V_0 (see Table E.4). It is seen that the disagreement of the tunnel splittings with the exact quantum splittings increases as the barrier height decreases.

The in-house python code is successfully validated, and the results are in good agreement with those given in the main Ref.¹⁷ In the next section, the tunnel splittings for three-fold cosine potentials within the ring-polymer instanton method are investigated.

Table E.4: Comparison of the instanton tunneling splittings Δ in reduced units with the exact quantum splittings for different barrier heights V_0 in Eq. (E.1) with $x_0 = 5\sqrt{V_0}$, $\beta\hbar = 30$, and $M = 512$.

V_0	2	1	0.5	0.25
Instanton	4.3905×10^{-8}	3.8601×10^{-4}	3.043×10^{-2}	2.27×10^{-1}
Quantum	4.15×10^{-8}	3.42×10^{-4}	2.25×10^{-2}	1.19×10^{-1}
Error	6%	13%	35%	91%

TUNNEL SPLITTING IN THE ONE-DIMENSIONAL THREE-FOLD COSINE POTENTIALS

The generalization of the ring-polymer instanton method for a molecular system with several degenerate wells can be found in the main Ref.²⁰ The three fold cosine potential is defined as

$$V(\phi) = \frac{V_3}{2}(1 - \cos 3\phi) \quad (\text{E.2})$$

To obtain the tunnel splitting, one needs to diagonalize the tunneling matrix \mathbb{W} defined as,

$$\mathbb{W} = h\mathbb{A} \quad (\text{E.3})$$

where the adjacency matrix \mathbb{A} for the three-fold connected wells is,

$$\mathbb{A} = \begin{pmatrix} 0 & 1 & 1 \\ 1 & 0 & 1 \\ 1 & 1 & 0 \end{pmatrix} \quad (\text{E.4})$$

and h is given by

$$h = \lim_{\beta \rightarrow \infty} \frac{\hbar}{\Phi} \sqrt{\frac{S_{kink}}{2\pi\hbar}} e^{-S_{kink}/\hbar} \quad (\text{E.5})$$

S_{kink} and Φ are the same as defined in section 2.3.

Table E.5 gives the results of tunnel splitting for the three-fold cosine potential with different number of beads and the imaginary time duration, which can be compared with the exact quantum value obtained from solving the one-dimensional Schrödinger equation. The barrier height is set to $V_3 = 10$. It is seen that the results are converged in the lower triangular part of the Table E.5. The approach is further examined for a range of barrier heights, given in Table E.6. As it was expected, the error arising from significantly anharmonic low barrier is very large.

Table E.5: Convergence of the tunneling splitting in reduced units obtained from Ring-Polymer instanton method for one-dimensional three fold cosine potential with $V_3 = 10$. The exact quantum value of splitting obtained by solving the Schrödinger equation is 0.082259.

$M/\beta\hbar$	15	30	60	120
8	2.7198	1.91×10^{-15}	1.61×10^{-31}	6.56×10^{-64}
16	0.00072	1.42×10^{-7}	1.91×10^{-15}	1.61×10^{-31}
32	0.02539	0.00072	1.42×10^{-7}	1.91×10^{-15}
64	0.07901	0.02539	0.00072	1.42×10^{-7}
128	0.0980	0.07901	0.02539	0.00072
256	0.10013	0.0980	0.07901	0.02539
512	0.10068	0.10013	0.0980	0.07901
1024	0.10082	0.10067	0.10013	0.0980
2048	0.10087	0.10082	0.10067	0.10013
4096	0.10087	0.10084	0.10082	0.10068

Table E.6: Comparison of the instanton tunneling splittings in reduced units with the exact quantum splittings for different barrier heights V_3 with $\beta\hbar = 15$ and $M = 4096$.

V_3	1	5	10	20	30	40	50
Instanton	1.05817	0.34387	0.10087	0.01435	0.002923	0.0007339	0.0002123
Quantum	0.47885	0.24064	0.08225	0.01271	0.002657	0.0006762	0.0001969
Error	121%	43%	23%	13%	10%	9%	8%

Curriculum Vitae

Personal details

First name/surname Somayeh Khazaei
Date of Birth 1st March 1983
Place of Birth Tehran, Iran
Nationality Iranian
E-mail somayeh.khazaei@chemie.uni-halle.de

Education

- Oct. 2013 - Jan. 2018 **Doctoral researcher** in *physical and theoretical chemistry*
Martin-Luther-Universitt Halle-Wittenberg, Halle(Saale), Germany.
Research group of Prof. Dr. Daniel Sebastiani.
Doctorate thesis on *Rotational tunnel splitting of methyl quantum rotors in the condensed phase*.
- Sep. 2007 - Mar. 2010 **Master of science** in *physics (Condensed Matter)*
Alzahra University, Tehran, Iran.
Research group of Prof. Dr. Vahid Daadmehr.
Master thesis on *Computing density of electronic states of capped carbon nanotubes using green's function approach*.
- Jan. 2003 - Jul. 2006 **Bachelor of science** in *physics (Condensed Matter)*
Zanjan University, Zanjan, Iran.
Research group of Prof. Dr. Amir Darooneh.
Bachelor thesis on *Simulation of cellular automaton models of traffic flow*.

Publications

- Somayeh Khazaei and Daniel Sebastiani, *Tunneling of coupled methyl quantum rotors in 4-methylpyridine: single rotor potential versus coupling interaction*, J. Chem. Phys. **147**, 194303 (2017).
- Somayeh Khazaei and Daniel Sebastiani, *Methyl rotor quantum states and the effect of chemical environment in organic crystals: γ -picoline and toluene*, J. Chem. Phys. **145**, 234506 (2016).
- Somayeh Khazaei, Mohammad Khazaei, Hosein Cheraghchi, Vahid Daadmehr, and Yoshiyuki. Kawazoe, *Considering the effect of different arrangements of pentagons on density of states of capped carbon nanotubes*, Physica. B Condens. Matter. **406**, 3885 (2011).

STATEMENT OF AUTHENTICITY

I hereby declare that I have written the present thesis independently, without assistance from external parties and without use of other sources than those indicated. The ideas taken directly or indirectly from external sources (including electronic sources) are duly acknowledged in the text. The material, either in full or in part, has not been previously submitted for grading at this or any other academic institution.

Place, Date

Signature

Halle, 17.07.2018

Khazan

